“Blind Interference Mitigation in Multi-Antenna GNSS Receivers”

Von der Fakultät für Elektrotechnik und Informationstechnik
der Rheinisch-Westfälischen Technischen Hochschule Aachen
zur Erlangung des akademischen Grades eines Doktors
der Ingenieurwissenschaften genehmigte Dissertation

vorgelegt von

Diplom-Ingenieur Emrah Taşdemir
aus Istanbul, Türkei

Berichter: Universitätsprofessor Dr.-Ing. Tobias G. Noll
Universitätsprofessor Dr.-Ing. Gerd Ascheid

Tag der mündlichen Prüfung: 26 Juli 2018

Diese Dissertation ist auf den Internetseiten der Hochschulbibliothek online verfügbar.

Contents

List of Abbreviations **5**

List of Symbols **9**

1 Introduction **11**

2 Signals **15**

2.1 Satellite Signal 15

2.2 Interference 20

2.3 Multipath 23

3 Receiver **25**

3.1 Antenna 25

3.1.1 Multi-antennas and Adaptive Beamforming 26

3.2 Front-End 28

3.2.1 Signal power to noise density ratio 30

3.2.2 Analog-to-Digital Conversion 31

3.3 Baseband Processing 35

4 Beamforming **39**

4.1 Beamformers 42

4.1.1 Deterministic Beamformer 42

4.1.2 MVDR: Minimum Variance Distortionless Beamformer 43

4.1.3 MPDR: Minimum Power Distortionless Beamformer 44
4.1.4 LCMV: Linearly Constrained Minimum Variance Beamformer . . 44
4.1.5 MMSE: Minimum Mean-Square Error Beamformer 45
4.1.6 Projection 46
4.1.7 PM: Power Minimization 47
4.2 Quantization 49
4.2.1 Quantization of the input signal 49
4.2.2 Quantization of the filter coefficients 51
4.3 2-Step Spatial Processing 54
4.3.1 Cost comparison 54
4.3.2 Pre-correlation Interference Mitigation 61
4.3.3 Post-Correlation Multipath Mitigation 73
4.4 Signal Outages and Vector Tracking Loops 81

5 Space-Time Processing 85
5.1 Notch Filters 87
5.2 Equalizer Filter 89
5.3 Combined Filtering 90
5.4 Implementation 92
5.5 Simulation Results 94
5.6 Comparison to Joint Filter Approach 97

6 Conclusion 101

A Tracking 105
A.1 Conventional Tracking Loops 106
A.2 Vektor Tracking Loops 108

B Position, Velocity, Time Computation 113

Bibliography **115**

List of Abbreviations

ACF Auto-Correlation Function

AGC Automatic Gain Control

ADC Analog to Digital Conversion

BPF BandPass Filter

BPSK Binary phase shift keying

CW Continuous Wave

CDMA Code division multiple access

DOA Direction Of Arrival

DFT Digital Fourier Transform

DLL Delay-Locked Loop

DSSS Direct sequence spread spectrum

EVD Eigenvalue EigenVector Decomposition

FIR Finite Impulse Response

FLL Frequency-Locked Loop

EQ EQualizer Filter

GBAS Ground Based Augmentation System

GNSS Global Navigation Satellite System

GPS Global Positioning System

IAA Iterative Adaptive Approach

IF Intermediate Frequency

IIR Infinite Impulse Response

INR Interference-to-Noise Ratio

LC Logic Cell

LCMV Linearly Constrained Minimum Variance Beamformer

LHCP Left-Hand Circularly Polarized

LMS Least Mean Square

LNA Low-noise amplifier

LO Local Oscillator

LOS Line-Of-Sight

LUT Look-Up-Table

MMSCE Minimum Mean-Square Correlation Error Beamformer

MMSE Minimum Mean-Square Error Beamformer

MMSSE Minimum Mean-Square Signal Error Beamformer

MP MultiPath

MPDR Minimum Power Distortionless Beamformer

MPM Multidimensional Power Minimization

MVDR Minimum Variance Distortionless Beamformer

NCO Numerically Controlled Oscillator

NF Notch Filter

PLL Phase-Locked Loop

PM Power Minimization

PPD Personal privacy device

PRN PseudoRandom Noise

PSD Power Spectral Density

PVT Position, Velocity and Time

RF Radio Frequency

RFI Radio Frequency Interference

RHCP Right-Hand Circularly Polarized

RMS Root-Mean-Square

SAGE Space Alternating Generalized Expectation Maximization

SNR Signal-to-Noise-Ratio

SNIR Signal-to-Noise-plus-Interference-Ratio

STAP Space-Time Adaptive Processing

VTL Vector Tracking Loops

WAAS Wide Area Augmentation System

List of Symbols

$\varphi_{xy}(\tau)$	Auto-correlation function of $x(t)$
$\varphi_{xy}(\tau)$	Cross-correlation function between $x(t)$ and $y(t)$
$x(t) * y(t)$	Convolution of $x(t)$ and $y(t)$
$\delta(t)$	Dirac-impulse
x^*	Complex conjugate of x
$\mathbf{R_{xx}}$	Auto-covariance matrix of $\mathbf{x}$
$\mathbf{R_{xy}}$	Cross-covariance matrix of $\mathbf{x}$ and $\mathbf{y}$
$\mathbf{R}^{\mathrm{H}}$, $\mathbf{R}^{\mathrm{T}}$	Hermitian and transpose of $\mathbf{R}$
$\mathbf{I}$	Unit matrix
$\mathcal{F}\{.\}$	Fourier-transform
$\mathrm{E}\{.\}$	Expectation
$\mathfrak{Re}\{.\}$, $\mathfrak{Im}\{.\}$	Real and imaginary part
$\mathrm{q}\{.\}$	Quantized value
$\hat{s}(t;\hat{f},\hat{\theta},\hat{\tau})$	Local signal replica with estimated carrier frequency $\hat{f}$, phase $\hat{\theta}$, and code delay $\hat{\tau}$
$\varphi^T_{\hat{s}x}(t;\hat{f},\hat{\theta},\delta\tau)$	Correlation between $\hat{s}(t;\hat{f},\hat{\theta},\hat{\tau}-\delta\tau)$ and $x(t)$ (computed over integration time T)
$\varphi^K_{\hat{s}x}(k;\hat{f},\hat{\theta},\delta\tau)$	Discrete correlation between $\hat{s}(kT_s;\hat{f},\hat{\theta},\hat{\tau}-\delta\tau)$ and $x(kT_s)$ (computed over K samples)
T_s, f_s	Sampling period and sampling frequency
T_c, f_c	Code chip period and chipping frequency
$\mathcal{E}$, $\mathcal{P}$, $\mathcal{L}$	Output of the early, prompt and late correlator
$\mathbf{P}^{\perp}$	Projection matrix
$\mathbf{\Xi}$	Output matrix of a multi-dimensional correlator bank

Chapter 1

Introduction

The vulnerability of Global Navigation Satellite Systems (GNSSs) to jamming has been a major concern for military applications. However, it has not been getting enough attention from the civilian community until recent years. This attitude changed due to the increasing availability of mobile jamming devices targeting GNSS and their growing popularity among civilians. Although the broadcast of non-satellite signals in the GNSS frequency bands is prohibited in many countries, the infrastructure to detect and prevent GNSS interference does not exist. Countermeasures on the receiver side are absolutely necessary to ensure the future use of GNSS for safety-critical applications.

In case of a single-antenna receiver, adaptive filter methods in the frequency/time domain can be used to mitigate frequency-limited or time-limited interference signals. Notch filters are, for example, suitable for suppressing narrow-band interference, whereas pulse blanking is an efficient method against pulsed interference. However, these methods are ineffective against wide-band interference. This kind of interference can efficiently be detected and mitigated in the spatial domain, i.e. using array-antennas and spatial signal processing. Furthermore, the spatial degrees of freedom of an array-antenna provide also an increased potential for multipath mitigation compared to the single-antenna receiver.

The price one has to pay for this increased potential is (aside from the bigger size of the antenna) an increased complexity of the algorithms used for multidimensional signal analysis and signal processing. Consequently, high-performance digital hardware platforms are required instead of the conventional hardware, in order to fulfill the real-time requirements. Associated higher costs and higher power consumption are in contradiction with the requirements of the mass-market. Hence, low-complexity solutions for spatial signal processing are essential for array-antenna GNSS receivers

to make the step to the mass-market.

The first aim of this thesis is to find efficient, easy-to-implement, and low-cost signal processing techniques for array-antenna GNSS receivers. The thesis focuses primarily on interference mitigation but it strives for an adequate multipath rejection performance as well. The first step is the review of the existing techniques and a careful consideration of their costs and benefits. Since the choice of the word lengths for the input signals and for the filter coefficients are directly linked to the hardware cost of a digital signal processing technique, special attention is to be given to quantization effects.

A low-complexity 2-step adaptive beamformer based on the Minimum Mean-Square Error Beamformer (MMSE) is the major outcome of the thesis. The two steps of the proposed method are (a) the pre-correlation interference mitigation and (b) the post-correlation multipath mitigation. Like the conventional MMSE, the presented 2-step beamformer is a blind approach: It does not require the knowledge about the antenna geometry, signal directions, or any kind of calibration, which makes it relatively simple compared to many other spatial processing techniques (such as the deterministic beamformer, the Minimum Variance Distortionless Beamformer (MVDR), or parametric spatial processing methods). On the downside, the MMSE in its conventional form is susceptible to multipath-induced errors. Therefore, it was refined in the proposed 2-step beamformer to give the beamformer a multipath-rejective character.

Later in the thesis, the presented 2-step beamformer will be combined with temporal filtering (with a bank of notch filters in particular) to form a spatiotemporal filter. The advantage of the combined filter is that it can mitigate an increased number of interference signals by making use of the spatial as well as the temporal characteristics of the received signal.

The thesis is structured as following: Chapter 2 introduces the signal models for the satellite signals. In addition, this chapter describes multipath reception and Radio Frequency (RF) interference and discusses their effect on the navigation performance by referencing real-life incidents. Chapter 3 presents the general structure of a GNSS receiver including the antenna, the analog front-end, and the digital baseband processing. Besides providing the basics, detailed information is given on the Analog to Digital Conversion (ADC) and its influence on the post-correlation SNR.

Chapter 4 focuses on beamforming as the core subject of the thesis. First, it gives an overview of the existing spatial processing techniques and highlights the advantages of the MMSE. In addition, this chapter analyzes the effect of quantization on the beamforming performance and provides two formulas that can serve as a general

rule-of-thumb for the choice of the word lengths in a beamformer. The second half of the chapter is dedicated to developing and optimizing the proposed 2-step beamforming technique. The last section in the chapter points to the promising concept of combining the vector tracking loops with beamforming for a continuous and stable positioning even under harshest interference conditions. Finally, the extension of the 2-step beamformer to a spatial-temporal filter with an improved interference mitigation performance is presented in Chapter 5.

Chapter 2

Signals

To prepare for the following chapters, this chapter gives an overview of the signals that are relevant for the rest of the thesis. Since Global Positioning System (GPS) is currently the only fully functional GNSS in global use, the interference and multipath mitigation techniques are discussed based on GPS signals throughout the thesis. However, these techniques can be applied to other GNSS signals (such as GLONASS, Galileo or Beidou) after minor modifications. A summary of the main characteristics of the GPS satellite signal is given in Section 2.1. Section 2.2 addresses the interference issue referencing real life incidents. Section 2.3 describes the multipath reception and its effects on GNSS-based positioning.

2.1 Satellite Signal

GPS satellite signals are Right-Hand Circularly Polarized (RHCP) signals. The type of spread spectrum employed by GPS is known as *binary phase shift keying direct sequence spread spectrum* (BPSK DSSS) signal [1].

Signal model

The received GPS satellite signal can be modeled as follows:

$$s_{\mathrm{RF}}(t) = \underbrace{\sqrt{2P_{\mathrm{R}}} \cdot \cos(2\pi(f_{\mathrm{RF}} + f_{\mathrm{D}})t + \theta_{\mathrm{R}})}_{\text{carrier}} \overbrace{\underbrace{D(t-\tau)}_{\text{data}} \underbrace{c_{N,\mathrm{p}}(t-\tau)}_{\text{(spreading) code}}}^{s_{\mathrm{D+c}}(t)} .$$

Here, P_{R} is the received signal power, $D(t)$ is the navigation data, and the cosine term is the RF carrier. $c_{N,\mathrm{p}}(t)$ is the spread spectrum signal with the code length N, where the

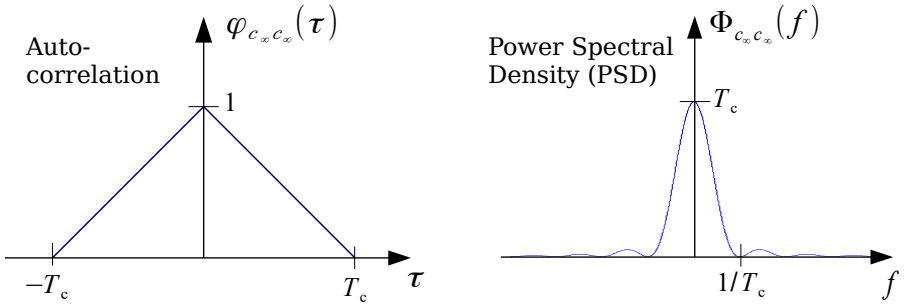


Figure 2.1: ACF $\varphi^{\infty}_{c_\infty c_\infty}(\tau)$ and the PSD $\Phi_{c_\infty c_\infty}(f)$ of an ideal infinite random sequence $c_\infty(t)$

letter p denotes the periodicity of the signal. τ is the time the satellite signal requires to travel from the satellite to the receiver. The travel time causes a delay in the code and the data signal. f_D is the Doppler shift of the carrier due to the movement of the satellite relative to the receiver.

The spread spectrum signal $c_{N,\mathrm{p}}(t)$ is ideally an infinite ($N \to \infty$) random sequence $c_\infty(t)$ of rectangular code-chips with a chip duration of T_c:

$$c_\infty(t) = \sum_{n=-\infty}^{\infty} c_n \cdot \mathrm{rect}\left(\frac{t}{T_\mathrm{c}} - n\right) \quad \text{with} \quad c_n \in \{-1; 1\}\,.$$

The Auto-Correlation Function (ACF) of $c_\infty(t)$,

$$\varphi^{\infty}_{c_\infty c_\infty}(\tau) := \lim_{T\to\infty} \frac{1}{T} \int_{-T/2}^{T/2} c^*_\infty(t) c_\infty(t+\tau)\,\mathrm{d}t = \frac{1}{T_\mathrm{c}} \mathrm{rect}\left(\frac{\tau}{T_\mathrm{c}}\right) * \mathrm{rect}\left(\frac{\tau}{T_\mathrm{c}}\right),$$

is a perfect triangle as illustrated in Figure 2.1 (left). The main task of the receiver in the baseband is to generate a local replica of the satellite signal and to synchronize it with the received satellite signal. For this purpose, the receiver computes the cross-correlation between these two signals, which is equal to the ACF from Figure 2.1, and maximizes the correlation value by adjusting the parameters of the local signal replica. Further details on this *tracking* procedure are given in Appendix A.

The Power Spectral Density (PSD) of c_∞, i.e. the Fourier transform of its ACF $\varphi^{\infty}_{cc}(\tau)$,

$$\Phi_{c_\infty c_\infty}(f) = \mathcal{F}\{\varphi^{\infty}_{c_\infty c_\infty}(\tau)\} = \frac{1}{T_\mathrm{c}} |T_\mathrm{c} \cdot \mathrm{sinc}(\pi f T_\mathrm{c})|^2, \tag{2.1}$$

is a sinc-square-function, which is also illustrated in Figure 2.1 (right). Finally, Figure 2.2 shows the PSD of the data-free code signal modulated onto the carrier. The one-sided noise equivalent bandwidth of this signal is $B_\mathrm{N} = 1/T_\mathrm{c}$.

In contrast to the infinite random code sequence, a real spread spectrum code sequence $c_N(t)$ has a finite length ($N < \infty$) and a finite duration of NT_c:

$$c_N(t) = \sum_{n=0}^{N-1} c_n \cdot \mathrm{rect}\left(\frac{t}{T_c} - n\right) = \mathrm{rect}\left(\frac{t}{T_c}\right) * \sum_{n=0}^{N-1} c_n \cdot \delta\left(t - nT_c\right).$$

The continuous spread spectrum signal

$$c_{N,\mathrm{p}}(t) = \sum_{k=-\infty}^{\infty} c_N(t - kNT_c) = \sum_{n=-\infty}^{\infty} c_n \cdot \mathrm{rect}\left(\frac{t}{T_c} - n\right) \qquad \text{with} \quad c_{n+N} = c_n$$

consists of the periodical repetitions of the code sequence. With the frequency spectrum of one code sequence of length N

$$\mathrm{C}_N(f) = \mathcal{F}\left\{c_N(t)\right\} = T_c \cdot \mathrm{sinc}(\pi f T_c) \cdot \sum_{n=0}^{N-1} c_n e^{-j2\pi f n T_c}$$

the PSD of the spreading signal $c_{N,\mathrm{p}}$ is given by

$$\Phi_{c_{N,\mathrm{p}}c_{N,\mathrm{p}}}(f) = \frac{1}{NT_c}\left|\mathrm{C}_N(f)\right|^2 \cdot \sum_{n=-\infty}^{\infty} \delta\left(f - \frac{n}{NT_c}\right) \tag{2.2}$$

$$= \overbrace{T_c \cdot \mathrm{sinc}^2(\pi f T_c)}^{\text{dominant}} \cdot \overbrace{\underbrace{\frac{1}{N} \cdot \left|\sum_{n=0}^{N-1} c_n e^{-j2\pi f n T_c}\right|^2}_{=:|\mathrm{C}_{\mathrm{code}}(f)|^2}}^{\text{fine structure}} \cdot \sum_{n=-\infty}^{\infty} \delta\left(f - \frac{n}{NT_c}\right). \tag{2.3}$$

$\Phi_{c_\infty c_\infty}(f)$

The first term in (2.3) is equal to the PSD of an infinite random sequence given by (2.1). It is the dominant term in (2.3) and gives $\Phi_{c_{N,\mathrm{p}}c_{N,\mathrm{p}}}(f)$ its main shape. The second term, the limit of which is 1 for $N \to \infty$, is the fine structure of $\Phi_{c_{N,\mathrm{p}}c_{N,\mathrm{p}}}(f)$ [2]. This term and the effect of the data signal $D(t)$ on the PSD can be neglected for most purposes.

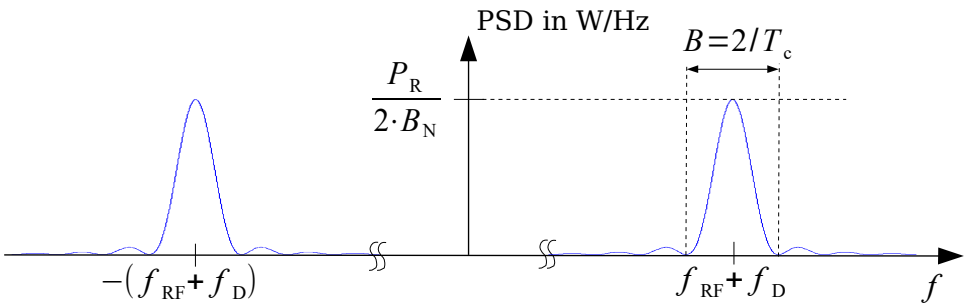


Figure 2.2: PSD of an infinite random sequence modulated onto the carrier signal: $s_{\mathrm{RF}}(t) = \sqrt{2P_R} \cdot c_\infty(t - \tau)\cos(2\pi(f_{\mathrm{RF}} + f_D)t + \theta_R)$

The inverse Fourier transform of $\Phi_{c_{N,\mathrm{p}}c_{N,\mathrm{p}}}(f)$ is the ACF $\varphi_{c_{N,\mathrm{p}}c_{N,\mathrm{p}}}(\tau)$ of a finite random sequence code signal, which is illustrated in Figure 2.3. The ACF linearly connects the discrete values $\varphi_{c_{N,\mathrm{p}}c_{N,\mathrm{p}}}(iT_\mathrm{c})$. Note that $\varphi_{c_{N,\mathrm{p}}c_{N,\mathrm{p}}}(0) = 1$, and if $c_{N,\mathrm{p}}$ is a truly random sequence

$$\mathrm{E}\{\varphi_{c_{N,\mathrm{p}}c_{N,\mathrm{p}}}(iT_\mathrm{c})\} = 0 \quad \text{and} \quad \mathrm{E}\left\{\left|\varphi_{c_{N,\mathrm{p}}c_{N,\mathrm{p}}}(iT_\mathrm{c})\right|^2\right\} = 1/N \tag{2.4}$$

hold for $i \neq 0$. On average, $\varphi_{c_{N,\mathrm{p}}c_{N,\mathrm{p}}}(\tau)$ is equal to the ACF of an infinite random sequence spread spectrum signal. i.e. it is nearly a triangular function. Generally, code tracking algorithms make use of this triangular shape of the ACF.

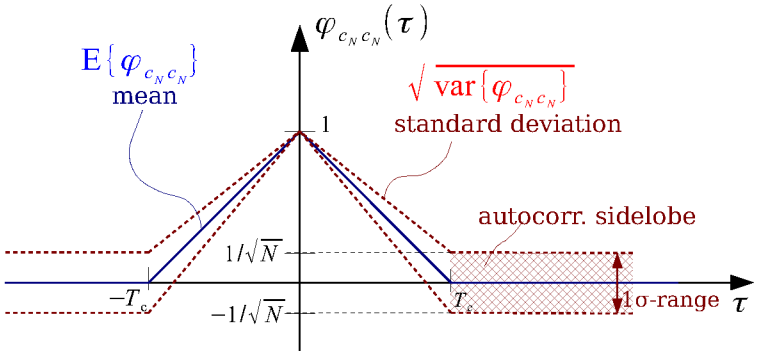


Figure 2.3: ACF $\varphi_{c_N c_N}(\tau)$ of a finite random sequence of length N

Similarly, the crosscorrelation function of two different code sequences $c_{N,\mathrm{p}}^{(k)}$ and $c_{N,\mathrm{p}}^{(l)}$ ($k \neq l$) connects the discrete values $\varphi_{c_{N,\mathrm{p}}^{(k)}c_{N,\mathrm{p}}^{(l)}}(iT_\mathrm{c})$ ($i \in \mathbb{Z}$). By analogy with (2.4)

$$\mathrm{E}\left\{\varphi_{c_{N,\mathrm{p}}^{(k)}c_{N,\mathrm{p}}^{(l)}}(iT_\mathrm{c})\right\} = 0 \quad \text{and} \quad \mathrm{E}\left\{\left|\varphi_{c_{N,\mathrm{p}}^{(k)}c_{N,\mathrm{p}}^{(l)}}(iT_\mathrm{c})\right|^2\right\} = 1/N$$

hold this time for $\forall i \in \mathbb{Z}$, i.e. the crosscorrelation between two different code sequences is small compared to the ACF of a code sequence.

In *code division multiple access* (*CDMA*) communication systems like GPS, each transmitter has a unique spreading code sequence. The low crosscorrelation between different code sequences enables the receiver to distinguish between different transmitters. In contrast to time division and frequency division methods, CDMA allows the simultaneous use of the same frequency band by all transmitters, which is also the case for GPS.

GPS-L1-C/A signal characteristics

The spreading codes used for the civil coarse/acquisition (C/A) signals broadcasted by GPS satellites are, in fact, not random code sequences but deterministic. Due to

the similarities of their autocorrelation and crosscorrelation properties to truly random code sequences, they are called *PseudoRandom Noise (PRN)* codes.

More precisely speaking, the GPS PRN codes are a selected group of so-called *Gold codes*, that are formed from a carefully chosen pair of *maximum-length linear shift register sequences* (m-sequences) of length $N = 1023$. They can be generated using two linear feedback shift registers of length $n = 10$ (with $N = 2^n - 1 = 1023$ non-zero register states)[2]. Autocorrelation and crosscorrelation values of the Gold codes are well defined as

$$\varphi_{c_{N,\mathrm{p}}^{(k)},c_{N,\mathrm{p}}^{(l)}}(iT_\mathrm{c}) \in \left\{1, \frac{-1}{N}, \frac{-\beta(n)}{N}, \frac{-\beta(n)-2}{N}\right\} \qquad \text{with} \quad \beta(n) = 1 + 2^{\lfloor (n+2)/2 \rfloor};$$

in particular,

$$\varphi_{c_{N,\mathrm{p}}^{(k)},c_{N,\mathrm{p}}^{(l)}}(iT_\mathrm{c}) \in \{1, -1/1023, -65/1023, -63/1023\}$$

holds for the GPS-C/A-codes [2]. $\varphi_{c_{N,\mathrm{p}}^{(k)},c_{N,\mathrm{p}}^{(l)}}(iT_\mathrm{c})$ becomes 1 only for $k = l$ and $\tau = 0$.

Characteristics of the GPS-L1-C/A signals are summarized in Table 2.1. In addition to the fixed values in Table 2.1, the maximum Doppler frequency of the carrier for a stationary user on Earth is approximately 4 kHz, corresponding to a maximum line-of-sight velocity of 800 m/s [3]. The Doppler frequency may approach values as high as 10 kHz in case of very high user velocities [4].

Data rate	f_B	$= 50$ Hz (bps)	
Bit duration	$T_\mathrm{B} = 1/f_B$	$= 20$ ms	(6000 km)
Chipping rate	f_c	$= 1.023$ MHz	
Bandwidth (null-to-null)	$B = 2f_\mathrm{c}$	$= 2.046$ MHz	
Chip duration	$T_\mathrm{c} = 1/f_\mathrm{c}$	$\approx 1\ \mu$s	(300 m)
Code length	N	$= 1023$	
Code duration	NT_c	$= 1$ ms	
Carrier frequency	$f_\mathrm{RF} = f_\mathrm{L1}$	$= 1575.42$ MHz	
Carrier period	$T_\mathrm{RF} = 1/f_\mathrm{L1}$	$= 0.635$ ns	(19 cm)

Table 2.1: Characteristics of the GPS-L1-C/A signal

Signal Power

The signal power P_{R} received by an antenna with a unit gain $G_{\mathrm{R}} = 1$ is given by

$$P_{\mathrm{R}} = \overbrace{\frac{P_{\mathrm{T}} \cdot G_{\mathrm{T}}}{L_{\mathrm{A}}} \cdot \underbrace{\frac{1}{4\pi R^2}}_{\text{path loss}}}^{\text{power spatial density}} \cdot \underbrace{\frac{\lambda^2}{4\pi}}_{\substack{\text{effective} \\ \text{receiver} \\ \text{antenna} \\ \text{area}}} . \tag{2.5}$$

P_{T} is the power at transmitter antenna input, G_{T} is the transmitter antenna gain, and L_{A} the atmospheric loss. The second term in the equation is the path loss due to the distance R the signal travels from the satellite to the receiver. The last term is the effective area of the receiver antenna with λ being the wavelength of the satellite signal.

According to the interface control document (ICD) GPS [5], the guaranteed signal power on the Earth's surface for the GPS-L1-C/A signal is $P_{\mathrm{R}} = 10^{-16}\mathrm{W} = -160\mathrm{dBW} = -130\mathrm{dBm}$. This means for the PSD of the satellite signal in Figure 2.2 a maximum value of $P_{\mathrm{R}}/(2B_{\mathrm{N}}) = -193\ \mathrm{dBm/Hz}$. Further, the received signal power is approximately proportional to the sine-square of the elevation angle of the satellite [6].

At room temperature (absolute temperature $T = 290\ \mathrm{K}$), the (two-sided) thermal noise spectral density is $\frac{N_{0,\mathrm{thermal}}}{2} = \frac{kT}{2} \hat{=} -177\ \mathrm{dBm/Hz}$, where $k = 1.38 \cdot 10^{-23}\ \mathrm{J/K}$ is the Boltzmann's constant. Note that the PSD of satellite signal with a maximum of $-193\ \mathrm{dBm/Hz}$ is $16\ \mathrm{dB}$ below the thermal noise floor.

2.2 Interference

GNSS signals are very weak (even weaker than the thermal noise floor as presented in Section 2.1) when received by users. They can easily be overwhelmed by a nearby device transmitting at neighboring frequencies [7]. Strong signals interfering with the GNSS frequency bands may reduce the reception quality or even completely "block" a GNSS receiver. For that reason, the broadcast of any non-GNSS signal at or near GNSS frequencies is prohibited in many countries. Nonetheless, Radio Frequency Interference (RFI) is a growing concern for safety-critical GNSS applications.

Until recently, most detected incidents involved unintended or accidental interference [7]. [8] reported, for example, that the Moss Landing Harbor was heavily jammed. Three commercially available VHF/UHF television antennas with built-in pre-amplifiers were identified to be the source of the Continuous Wave (CW) interference. In [9] a "GNSS repeater", that was used to check the functionality of the GPS

equipment on airplanes within a hangar at a German airport, was identified as the source of the interference. The repeater signal leaked outside the hanger because the repeater transmit power was set too high. The interference signal was received even from the sky by several aircrafts using that airport [7].

Unlike previously, recent observations suggest the increasing intentional use of illegal portable jamming devices. The usage of GNSS jammers may be motivated by criminal intention such as disabling a vehicle theft-protection system, a fraud attempt against a distance-based road-user charging system or a distance-based vehicle insurance. A further reason is by privacy concerns. The popular alias "personal privacy device" (PPD) used for GNSS-jammers stresses their use for this purpose, as the primary market for these devices consists of people who fear being tracked or monitored by GNSS in their vehicles [10]. Such devices can, nowadays, be easily purchased through a number of websites and online entities. Their cost ranges from a few tens of dollars to several hundred and they are offered in different shapes; some designed to fit in the cigarette lighter of automobiles and some disguised as cell phones with an internal battery [11, 12].

Actually, a user who buys a PPD intents and expects to block tracking devices merely in his or her own vehicle. Contrary to the user's assumption, the effective range of a jamming device is significantly larger than the volume of one vehicle; it may reach up to several kilometers [7, 11].

PPDs are already sufficiently common on highways as to present a significant threat to safety-critical GNSS users that must operate in proximity to busy roadways [7]. RFI affecting the reference receivers of the Ground Based Augmentation System (GBAS) at the Newark Liberty International Airport was traced back to a PPD used by a truck driver who passed the airport each day [13]. The driver was arrested and charged. [14] also reported RFI affecting the reference station of the Wide Area Augmentation System (WAAS) in Leesburg, Virginia. In Britain, two truck thieves were jailed for 16 years, because they used GPS jammers to prevent the trucks from being tracked after the thefts. In Germany, some truck drivers have been using jammers to evade the country's GPS-based road-toll system [11]. Both presumably intentional and unintentional interference was detected at the KHH airport in Taiwan. Interference mostly occurred during the work hours [15].

Signal model

There are many types of RFI including CW, chirp signals, pulses, narrowband noise, and broadband noise [11]. In general an interference signal $s(t)$ is a cosine function

with a frequency change over time and a baseband component $s_{\mathrm{BB}}(t)$:

$$s(t) = \sqrt{2P_{\mathrm{R}}} \cdot \cos\left(2\pi \int_{t'=0}^{t} f(t')\,\mathrm{d}t' + \theta\right) \cdot s_{\mathrm{BB}}(t).$$

The simplest form of interference is CW interference, which is a single tone signal with a constant frequency $f(t) = f_0$ ($s_{\mathrm{BB}}(t) = 1$). This kind of interference is more likely to be unintentional, e.g. caused by the harmonics of electronic equipments [15]. Single tone signals whose instantaneous frequency changes linearly over time ($f(t) = f_0 + k \cdot t$) are called chirp or swept frequency signals.

Chirp signal is the most common signal type transmitted by commercial GNSS jammers. In [11, 10] authors purchased some jammers offered online in order to analyse their signal characteristics in a laboratory environment and in open-field tests. The first results showed that the majority of low-cost in-car jammers transmit a chirp signal with a bandwidth between 9.4 to 44.9 MHz in the E1/L1 band (other frequency bands were not considered in these works). The sweep period of the jammers is about 9 μs on average [11]. Among the examined jammers, there were also CW oscillators with a 3 dB-bandwidth of around 0.92 kHz and have a temperature-dependent center frequency around the Galileo/GPS center frequency.

Noise interference is the case, if the baseband component $s_{\mathrm{BB}}(t)$ of $s(t)$ is a noise-like signal with small temporal correlations. The descriptions narrowband and broadband refer to the bandwidth of s_{BB} relative to the chipping rate f_{c} of the satellite signals. While CW or chirp interference with slow frequency variations can be mitigated by means of temporal filtering, e.g. using notch filters, temporal processing is not suitable for mitigating chirp signals with fast frequency changes or broadband noise signals. Chirp signals with fast frequency changes are hard to track; and broadband noise signals show no temporal correlation at all. Instead, the receiver may take advantage of the spatial signal characteristics (which are determined by the signal direction) in order to mitigate these types of interference. In Chapter 4, the use of multi-antennas along with different beamforming techniques is discussed. The mitigation performance can be improved by combining spatial processing with temporal processing. Accordingly, Chapter 5 presents a combined spatio-temporal filter and provides a comparison to the spatial-only filter.

Devices with a baseband component $s_{\mathrm{BB}}(t)$ equal to a satellite's code signal are called *spoofer*s. If cleverly designed, these devices may deceive a GNSS receiver by mimicking satellite signals instead of blocking the receiver's signal reception. Spoofing attacks can be detected and combated, e.g. at post-correlation stage by determining the arrival directions of the received satellite signals and comparing them with the ex-

pected satellite constellation. Spoofing is not subject of this thesis, instead, the thesis focuses exclusively on incoherent RFI.

2.3 Multipath

MultiPath (MP) is the reception of reflected or diffracted replicas of the desired Line-Of-Sight (LOS) satellite signal. Since GNSS positioning relies on LOS range and velocity measurements between the receiver and the satellite, MP reception may distort these measurements and thus is unfavorable for GNSS positioning.

While most system inherent errors of GNSS (such as satellite clock errors, ephemeris errors, or atmospheric errors) can be significantly reduced by techniques like precise modeling, dual-frequency reception, and differential GPS, MP remains to be an important error source to GNSS positioning. In the complex terrain and urban environments, the ranging error caused by MP can be up to tens of meters [16].

Techniques for multipath mitigation at antenna level are discussed in Section 3.1. Later in Section 4.3.3, a digital adaptive beamforming algorithm is presented to reduce multipath effects in an array-antenna receiver.

Signal model

A simple way to model multipath reception is to represent it as a set of M discrete specular reflections:

$$s_{\mathrm{MP}}(t) = \sum_{m=1}^{M} s_{\mathrm{RF},m}(t)$$
$$s_{\mathrm{RF},m}(t) = \sqrt{2\alpha_m P_{\mathrm{R}}} \cdot \cos(2\pi(f_{\mathrm{RF}} + f_{\mathrm{D}} + \Delta f_{\mathrm{D},m})t + \theta_{\mathrm{R},m}) c_{N,\mathrm{p}}(t - \tau - \Delta\tau_m).$$

α_m is the multipath-to-direct ratio (i.e. the signal attenuation due to reflection) of the m-th multipath, $\Delta\tau_m$ is the relative delay, and $\Delta f_{\mathrm{D},m}$ is the relative Doppler frequency. The navigation data is omitted for the sake of simplicity.

Since the path traveled by a reflection is always longer than the direct path, multipath signals are delayed relative to the direct signal ($\Delta\tau > 0$). When the delay is more than twice the code chip duration ($\Delta\tau > 2T_{\mathrm{c}}$), the correlation between the reflected signal and the direct signal is negligible. In this case, reflected path can be perfectly distinguished from the direct path. As long as the receiver tracks the direct path, such

long-delay multipaths have little effect on positioning performance. However, multipath signals caused by nearby objects have a shorter delay. Such short-delay reflections are strongly correlated with the direct signal. Hence, their reception distorts the correlation function between the received code signal and the local code replica. They also distort the composite phase of the received signal, introducing errors in pseudorange and carrier phase measurements [3]. Unfortunately, objects close to the antenna cause the strongest multipath in general [17].

The relative motion between the satellite's reflection on a surface and the receiver is different from the relative motion between the actual satellite and the receiver. Thus, in general, the reflected signal has a different Doppler shift than the direct signal. However, if the Doppler difference Δf_{D} is significantly large (larger than the reciprocal of the coherent integration time in the correlator), the multipath signal is essentially uncorrelated with the direct path [3]. Like in case of long-delay multipath, multipath signals with large relative Doppler shifts practically do not influence the range measurements.

In fact, truly specular reflections require the existence of large (significantly larger than the carrier wavelength $\lambda = c/f_L \approx 19$ cm) and smooth reflecting surfaces. This is the case, for example, for a receiver, that is placed on an airplane and receives reflected signals from the wings and the tail, or for multipath reception due to a smooth sea surface. However, multipath environments are in general more complex and diverse. Some more realistic channel models (e.g. [18, 19]) exist, which can be used for an accurate evaluation of different multipath mitigation techniques. Nonetheless, they give little insight into the underlying issues and characteristics [3].

Two-path channel model (direct signal and one reflection) is indeed the most commonly used model for examining multipath and corresponding mitigation techniques for GNSS applications. The two-path scenario with a strong specular reflection is a more challenging scenario compared to diffuse multipath. According to [3], it is sufficient for a GNSS receiver, although it may not be necessary, to perform well under these simple conditions.

Hence, the two-path channel model is used in this thesis to evaluate the adaptive beamformer in Section 4.3.3 with regard to multipath mitigation performance. The focus here is on short-delay multipath with a Doppler shift close to the Doppler shift of the direct signal.

Chapter 3

Receiver

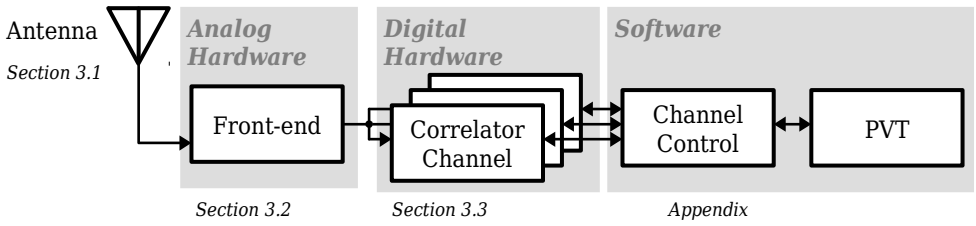


Figure 3.1: Signal processing chain of a GNSS receiver

This chapter gives an insight into the general structure of a GNSS receiver. In accordance to the signal flow illustrated in Figure 3.1, the chapter starts presenting the antenna in Section 3.1 including introductory information on phased array antennas and adaptive beamforming. It continues with the conditioning of the RF signal using analog hardware in Section 3.2. This section pays close attention to the ADC of the RF signal and its effects on the SNR. Section 3.3 describes finally the digital baseband processing, i.e. the correlator channels, that are usually realized in digital hardware (excluding software defined radio receivers). Control of the correlator channels and computation of the Position, Velocity and Time (PVT) are included in the appendix.

3.1 Antenna

The antenna is the first element of a GNSS receiver. Due to their low aerodynamic profile, ease of construction and low cost, microstrip patch antennas are the most common antenna type used for GNSS signal reception. Helix antennas are also widely used [20].

Fundamental parameters that are associated with the antenna are its frequency, bandwidth, polarization, and gain pattern [4]. These parameters should match with

the desired signal's characteristics (frequency $\approx$ 1575.42 MHz, bandwidth $\geq$ 2 MHz, and RHCP in case of GPS-L1-C/A). Matching the polarization of the antenna with the satellite signal provides a significant level of suppression of multipath signals already at antenna level. This is due to the fact that a satellite signal's polarization flips from RHCP to Left-Hand Circularly Polarized (LHCP), when the signal is specularly reflected [4]. (A second reflection would actually flip the polarization back to RHCP, but this signal would be even weaker than the first reflection.)

Especially reflections from the ground the receiver is standing on (*ground multipath*) played a significant role in the history of GNSS antenna design. This type of multipath dominates others, for example, in case of a receiver that stands on the roof top of a building. Hence, hemispherical gain patterns are desired, that attenuate negative or low elevation angles ($\lesssim 15°$). As an example, choke ring antennas are single antennas placed in the middle of a set of concentric conductive cylinders [21]. They provide the desired gain pattern. Antennas placed on different types of ground planes (conventional metallic, resistivity tapered [22], choke ring [23]) or the "multipath rejecting antenna" (a vertical antenna array with a fixed gain pattern) in [24] are also designed to combat ground multipath.

3.1.1 Multi-antennas and Adaptive Beamforming

The use of multi-antennas (array-antennas as a special case) and adaptive beamforming is an effective method against RFI and MP. Figure 3.2 illustrates the principle of multi-antenna reception in a two-dimensional model.

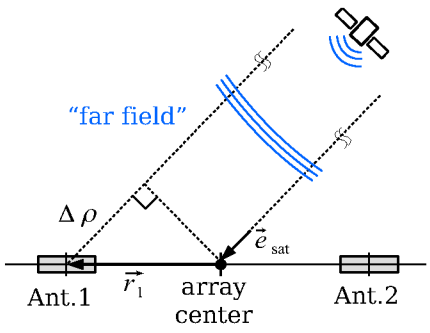


Figure 3.2: Phase shift at an array antenna

In the far-field, the satellite signal can be approximated as a plane wave. In case the signal impinges from an orthogonal direction onto the array plane, the wavefront arrives all array elements at once. If the transmitter is located at an oblique angle as in Figure 3.2, the signal wavefront travels slightly different distances from the source to

the antenna center and to the different antenna elements. Hence, individual elements of the antenna receive the signal with different delays. As a result, the carrier signals received by different elements are phase-shifted relative to one another. This phase shift is a function of the signal direction.

In particular, the phase-shift at the k-th antenna element compared to a predefined antenna center is

$$\Delta\theta_k = 2\pi\frac{\Delta\rho}{\lambda_{\text{RF}}} = 2\pi\frac{\vec{r}_k \cdot \vec{e}_{\text{sat}}}{\lambda_{\text{RF}}}, \tag{3.1}$$

where $\vec{e}_{\text{sat}}$ is the unit vector pointing from the satellite to the antenna center, $\vec{r}_k$ is the vector from the antenna center to the k-th antenna element, and λ_{RF} is the wavelength of the RF carrier signal. Since $\Delta\rho$ is small compared to the length $c_0 T_{\text{c}}$ of one code chip the code delay differences between the array elements can be neglected. Thus, we can assume that individual elements receive identical code signals but a phase difference in the carrier exists.

Beamforming is the name of weighting, phase-shifting and combining the outputs of individual antenna elements in such a way that desired signals from particular directions are amplified (constructive) while others like interferences are attenuated (destructive). This can be done at different stages of signal processing: In analog or in digital domain; at pre-correlation, at post-correlation, or in multiple distributed steps. The challenge here is to adapt the beamforming weights to the signal and noise environment. Further details on beamforming are discussed in Chapter 4.

Until recent years, the use of multi-antennas was limited to military applications [22, 17], but lately this approach attracts great interest also in the research community. [25, 26] present a 2×2-array of microstrip patch antennas with a patch side length of approximately 50 mm and a nearly $\lambda/2$ (95 mm) center-to-center element spacing. The elements of the array are designed to receive signals in the L1-band and to reject out-of-band interference. An active 2×2-array-antenna with $\lambda/2$ element spacing is also presented in [27].

In [25, 26], a calibration signal is generated digitally, upconverted, and injected into the receiver path via directional coupling in order to measure the signal distortions caused by the front-end. The calibration signal is basically a reserved PRN sequence modulated onto the carrier. A dedicated tracking channel estimates the parameters of the calibration signal, in order to use this information later, e.g. for direction of arrival estimation or for computing the beamforming weights. A *compact* array antenna based on the same principle with a $\lambda/4$ ($47.5\,\text{mm}$) spacing is presented in [28]. In order to cope with the mutual antenna coupling due to the reduced element separation, [28] employs a decoupling and matching network between the antenna array and the calibration

network. A 6x6-array of two stacked patches for *dual-band reception* is presented in [20]. Like the previous, [20] employs a calibration network for online calibration. In addition to rectangular arrays, circular arrays like the 8-element array with a diameter of 15 cm in [29] are also frequently used. Further, the use of dual polarization antennas (with separate RHCP and LHCP reception) are also proposed, e.g. by [30], in order to increase the degrees of freedom of the spatial processing.

A simpler approach compared to the previous ones is presented in [31]: Multiple commercial single antennas were mounted on a ground plane to build an array. Since a calibration signal is missing in this case, on-line calibration was not possible for this array. In order to calibrate the array-antenna, the receiver executes a calibration procedure, if possible in an open-sky environment in order to avoid multipath reception during calibration. In addition, information about the array orientation must be provided externally. Besides the planar array-antennas, [32] proposes 3D-arrays to improve the Up/Down spatial resolution of the antenna.

3.2 Front-End

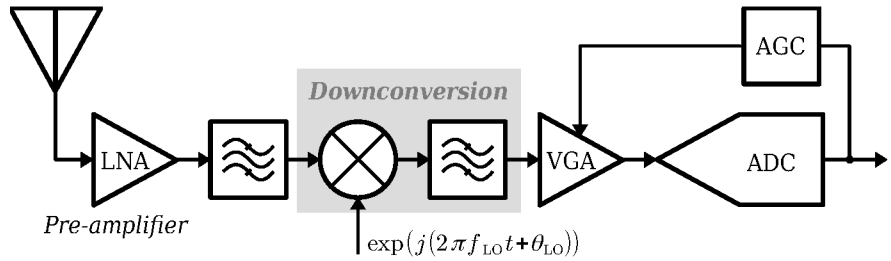


Figure 3.3: Single-antenna front-end

The analog voltage at the antenna output is too weak and has a too high frequency for most of the analog-to-digital converters (ADC) to operate. A chain of amplifiers, mixers, and filters is required for signal conditioning before the ADC [4]. Figure 3.3 shows a simplified block diagram of the analog processing chain. The overall signal *amplification* of a GNSS front-end is in the order of 100 dB.

The noise figure F_{R} of a system is defined as the degradation of the signal power to noise density ratio (C/N_0) as the signal passes through the system components [2]. According to the *Friis' formula*, the first element in the RF cascade dominates the resulting noise figure for the system [4]. Hence, a *low-noise (pre)amplifier* (LNA) with a gain of 25-40 dB and a noise figure of typically less than 2 dB is employed as the first active element of the analog signal chain. In order to avoid the negative impact of any passive components prior to the first LNA, (such as cables and filters) the LNA is usually

integrated into the antenna. Such an antenna is called an *active antenna*. The addition of preselection filtering, burnout protection and associated losses result in an overall noise figure of 3-4 dB [1].

The LNA is followed by an RF BandPass Filter (BPF) in order to suppress out-of-band interference. Usually a surface acoustic wave (SAW) filter is used for this purpose. At the mixer stage, the signal is mixed with a Local Oscillator (LO) signal

$$s_{\text{LO}}(t) = \exp(j(2\pi f_{\text{LO}} t + \theta_{\text{LO}})) \qquad \text{with} \quad f_{\text{LO}} = f_{\text{IF}} - f_{\text{RF}},$$

in order to downconvert the RF signal to an intermediate frequency (IF). The IF is typically one hundredth to one thousandth of the RF. Higher front-end bandwidths and correspondingly high IFs are required if the receiver uses a narrow correlator spacing (less than 1-chip) [3], which is advantageous against multipath. The RF BPF must greatly attenuate any signals at the so-called *image frequencies* before downconversion. Image frequencies are those located at $\pm(f_{\text{RF}} - 2f_{\text{IF}})$. These frequencies are moved to f_{IF} as a side effect of downconversion.

In practice, downconversion is usually carried out in multiple stages (typically in two), i.e. in a chain of mixer and filter stages. This is to prevent *self-jamming* and the requirement of filters with extremely high *quality-factor*s (*Q-factor*). Self-jamming is the phenomenon that occurs if the required total gain is applied directly at the RF frequency in a single step. In this case, strong output of the amplifier can leak back to the input and cause oscillations in the receiver front-end. The Q-factor is defined as the ratio between the center frequency and the bandwidth of a filter. High Q-factors, i.e. narrow-band filters at high frequencies, are in general hard to implement [4].

The analog satellite signal after conditioning (and prior to ADC) is given by

$$s^{(l)}(t) = \sqrt{C^{(l)}} \cdot \exp(j2\pi f^{(l)} \cdot t + \theta) D^{(l)}(t - \tau^{(l)}) c^{(l)}(t - \tau^{(l)}) \tag{3.2}$$

with $f^{(l)} = f_{\text{IF}} + f_{\text{D}}^{(l)}$ the carrier frequency of the satellite signal at IF and $C^{(l)}$ the signal power. Disregarding multipath and RFI, the total signal

$$x(t) = \sum_{l} s^{(l)}(t) + n(t) \tag{3.3}$$

is the superimposition of the received satellite signals $s^{(l)}(t)$ and a white Gaussian noise $n(t)$. The real part $\mathfrak{Re}\{x(t)\}$ is called the in-phase (I) and the imaginary part $\mathfrak{Im}\{x(t)\}$ quadrature-phase (Q) components of the signal.

In case of a multi-antenna receiver, identical front-ends are used after each antenna element. These front-ends share the same LO signal for frequency downconversion

and the ADC in all front-ends should take place synchronously. The multi-antenna signal after analog signal conditioning is

$$\mathbf{x}(t) = \sum_l \mathbf{a}^{(l)} s^{(l)}(t) + \mathbf{n}(t) \qquad \text{with} \quad a_k^{(l)} = \exp\left(j2\pi \cdot \Delta\theta_k^{(l)}\right), \tag{3.4}$$

where $\mathbf{a}^{(l)} = \left[a_1^{(l)}, a_2^{(l)}, \ldots, a_{N_{\text{ant}}}^{(l)}\right]^{\mathrm{T}}$ is called the *steering vector* of the l-th satellite signal. The steering vector represents the phase shifts $\Delta\theta_k^{(l)}$ each antenna element experiences relative to the antenna center as given in (3.1). $\mathbf{n}(t)$ is a multivariate white Gaussian noise . The noise in the different antenna channels is assumed to be uncorrelated, i.e. the noise covariance matrix is $\mathbf{R_{nn}} = \mathrm{E}\{\mathbf{n} \cdot \mathbf{n}^{\mathrm{H}}\} = \sigma_{\mathbf{n}}^2 \cdot \mathbf{I}$, where $\mathbf{I}$ is the unit matrix.

In reality, additional phase shifts and signal distortions arise due to the variations between the antenna channels (e.g. different cable lengths between the antenna elements and their front-ends, variations in the front-ends etc.). Deterministic beamforming algorithms or algorithms estimating the Direction Of Arrival (DOA) of the satellite signals require the exact knowledge of these additional phase shifts, i.e. the antenna needs to be calibrated as discussed in Section 3.1.1. As this thesis focuses on blind algorithms that do not require any information about the antenna geometry or front-end induced phase shifts, these phase shifts are omitted in (3.4).

3.2.1 Signal power to noise density ratio

Signal power C_{LNA} at the input of the LNA is

$$C_{\text{LNA}} = \frac{P_{\text{R}} G_{\text{R}}}{L_{\text{R}}},$$

where P_{R} from (2.5) is the maximum available signal power, G_{R} ($\lesssim 1$, except for low elevations) is the gain of the receiver antenna, and L_{R} stands for the losses from the passive components prior to the LNA. For a typical antenna $C_{\text{LNA}} = -162.5 \cdots -154.5$dBW [2].

The signal to noise density ratio after analog signal conditioning is

$$\frac{C}{N_0} = \frac{C_{\text{LNA}}}{k(T_{\text{A}} + T_{\text{R}})} \qquad \text{with} \quad T_{\text{R}} = T_0(F_{\text{R}}(T_0) - 1),$$

where T_{A} is the effective noise temperature of *external* noise received by the antenna such as the noise from natural sources outside of the receiver, signals from other GNSS satellites, and other man-made signals. Typically, $T_{\text{A}} = 75 \cdots 100$ K [2]. This yields an

overall effective noise temperature $T_\mathrm{E} = T_\mathrm{A} + T_\mathrm{R} = 363 \cdots 538\,\mathrm{K}$. T_R is the receiver's effective noise temperature caused by *internal* noise sources (dominated by the noise performance of the first few stages). $F_\mathrm{R}(T_0)$ stands for the noise figure given for the reference input noise temperature T_0 (usually $T_0 = 290\,\mathrm{K}$ "room temperature"). Typical values for the noise figure are $F_\mathrm{R}(T_0) = 3 \cdots 4\,\mathrm{dB}$ [1]. Altogether, $C/N_0 = 39 \cdots 48\,\mathrm{dB/Hz}$ can be expected. When the (one-sided) noise equivalent bandwidth of the front-end is equal to the null-to-null bandwidth of the satellite signal, i.e. $B_\mathrm{N} = 2.046\,\mathrm{MHz}$, typical values for the SNR before correlation are $\mathrm{SNR} = C/P_n = C/(N_0 B_\mathrm{N}) = -24 \cdots -15\,\mathrm{dB}$.

3.2.2 Analog-to-Digital Conversion

Final stage of the front-end is the analog-to-digital converter (ADC). At this stage the *quantization* and *sampling* of the analog signal takes place. Below, the effect of the front-end bandwidth B and the quantization word length on the SNR is discussed in detail.

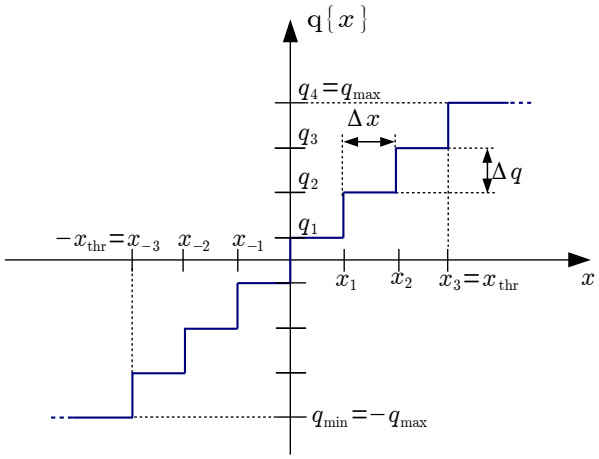


Figure 3.4: Mid-rise uniform quantizer

Figure 3.4 illustrates the quantization function $\mathrm{q}\{x\}$ of a mid-rise uniform quantizer for a scalar real input value x. Uniform means that the decision levels x_i at the input and the quantizing levels q_i at the output of the quantizer are equally spaced. The step sizes between the levels are

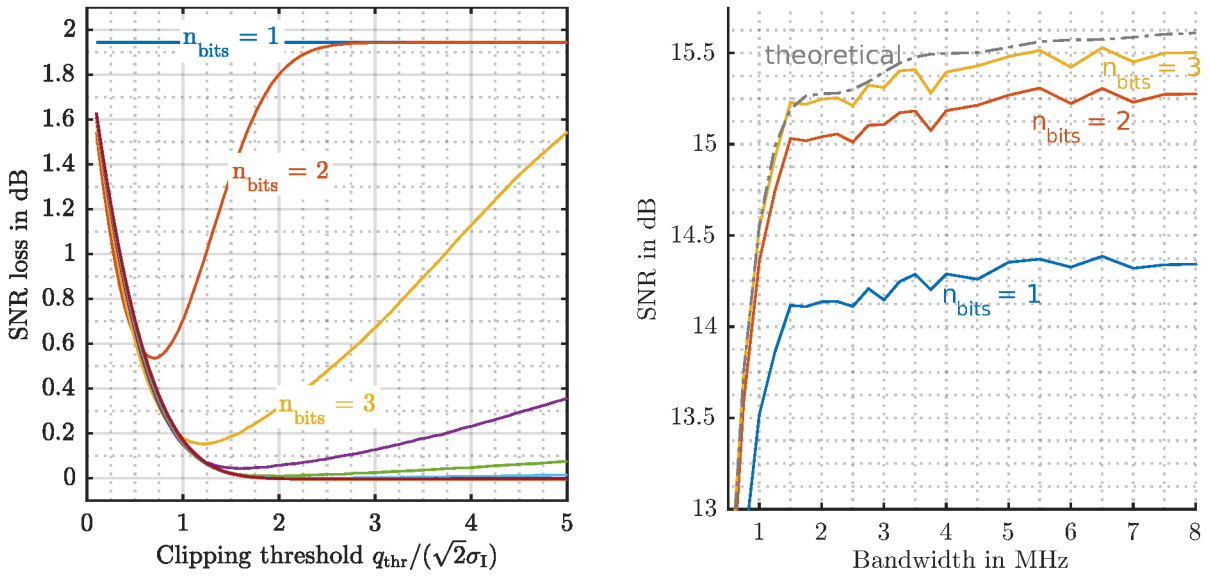
$$\Delta x = \frac{q_\mathrm{max} - q_\mathrm{min}}{2^{n_\mathrm{bits}} - 2} \quad \text{and} \quad \Delta q = \frac{2x_\mathrm{thr}}{2^{n_\mathrm{bits}} - 1}.$$

The number of available discrete values at the output is 2^{n_bits} with n_bits the word length of the quantizer output. $[-x_\mathrm{thr}, x_\mathrm{thr}]$ is the analog input range. Input values exceeding the clipping thresholds $\pm x_\mathrm{thr}$ are assigned to the maximum available output value q_max or to the minimum available value q_min of the quantizer respectively.

In order to analyze the SNR loss caused by quantization, discrete time samples (sampling frequency $f_s = 2.046$ MHz) of the front-end signal $x(t)$ with a C/N_0 of 42.7 dBHz were generated in MATLAB as given in (3.3). The complex valued signal x was quantized using two uniform quantizers, one for the I-component and one for the Q-component of the signal. If the signal power is low compared to the noise power ($C \ll P_n$), as it is the case here and in general for GNSS signals, the SNR after quantization can be computed as

$$\mathrm{SNR} = \frac{C}{P_n} = \frac{\mathrm{E}\{s^* \cdot \mathrm{q}\{x\}\}^2}{\mathrm{E}\{|s|^2\} \cdot \mathrm{E}\{|\mathrm{q}\{x\}|^2\}},$$

where s is the satellite signal given in (3.2). In case of Nyquist-sampling, the maximum available SNR is $\mathrm{SNR}_{\mathrm{max}} = C/(N_0 f_s)$.



(a) Quantization loss for very low SNR

(b) Impact of the bandwidth on the SNR ($C/N_0 =$ 42.7 dBHz)

Figure 3.5: Impact of quantization and signal bandwidth on the SNR

In Figure 3.5a, the SNR loss ($\mathrm{SNR}_{\mathrm{max}} - \mathrm{SNR}$) due to quantization is plotted for various word lengths n_{bits} as a function of the clipping threshold x_{thr}. x_{thr} is normalized by the standard deviation $\sigma_{\mathrm{I}} = \mathrm{E}\{|\Re\mathrm{e}\{\mathrm{q}\{x\}\}|^2\}$ of the I component of the quantized signal ($\sigma_{\mathrm{Q}} = \mathrm{E}\{|\Im\mathrm{m}\{\mathrm{q}\{x\}\}|^2\} = \sigma_{\mathrm{I}}$). The SNR loss is, in fact, not a function of the sampling frequency f_s and C/N_0 as long as $C \ll P_n$ and $N_0 = \mathrm{const.}$. These values were given above for the sake of completeness.

Figure 3.5a shows that the SNR loss due to quantization is less than 2 dB even in case of a 1-bit-quantizer. Multibit quantizers achieve better SNR values, only if the

clipping threshold x_{thr} is adapted to the standard deviation $\sigma_{\text{I}} = \sigma_{\text{Q}}$ of the input signal. Optimum thresholds, that minimize the SNR loss, can be identified from Figure 3.5a. The values here are conform to those given in [33] universally for uniform quantizers. Optimum threshold and the minimum possible SNR loss [34] for different word lengths are listed in Table 3.1.

Number of bits	Optimum threshold [33] $x_{\text{thr}}/\sigma_{\text{I}}$	Pre-correlation SNR loss in dB [34]	Post-correlation SNR loss in dB
1 (no AGC)	0	1.961	1.23
2 (typical)	0.996	0.550	0.30
3	1.758	0.166	0.09
4	2.346	0.050	0.03
5	2.822	0.015	0.01

Table 3.1: Quantization loss for very low SNR

It can be concluded that the SNR (and consequently the range estimation accuracy) does not significantly improve for more than 3 bits [35]. Further, it is known that the performance gap between the uniform and the non-uniform quantization is also insignificant [35]. Note that in order to achieve the optimum SNR values given in Table 3.1, some form of *automatic gain control* (*AGC*) must be implemented in the front-end to adaptively control the clipping thresholds of the quantizer. RFI is not taken into account yet. Actually quantization with such short word lengths is vulnerable to interference [36]. This topic is discussed in Section 4.2.

In Table 3.1, the estimate of the SNR after correlating the received signal $x(t)$ with the local satellite signal replica $\hat{s}(t)$ is included as well. Given that there is no RFI or multipath and the noise $n(t)$ is unbiased, the SNR of the I-component $\mathcal{P}_{\text{I}} = \mathfrak{Re}\{\mathcal{P}\}$ of the "prompt" correlator is

$$\text{SNR}_{\mathcal{P}_{\text{I}}} = \frac{\text{E}\{\mathcal{P}_{\text{I}}\}^2}{\text{E}\{|\mathcal{P}_{\text{I}} - \text{E}\{\mathcal{P}_{\text{I}}\}|^2\}}.$$

Further details on correlation are discussed in Section 3.3.

Maximum available SNR at this stage (for $n_{\text{bits}} \to \infty$ and $B \to \infty$) is

$$\text{SNR}_{\mathcal{P}_{\text{I,max}}} = \frac{1}{2T}\frac{C}{N_0}$$

with T the pre-detection integration time. As stated in [37], SNR loss observed after correlation is slightly smaller than the SNR measured before correlation. This can be

explained by the fact that the quantization error, which is usually modeled as an additive white noise, is actually correlated with the satellite signal.

Figure 3.5b shows how the final bandwidth after analog signal conditioning affects the SNR (measured after correlation) in combination with the quantization. SNR for different word lengths as well as its theoretical maximum (given by (3.7) and (3.8)) are plotted. With regard to SNR, there is no significant advantage in increasing the bandwidth beyond the null-to-null bandwidth (2.046 MHz) of the satellite signal. In [38] even a decrease in the SNR is claimed, if the bandwidth in increased. However, this decrease does not occur in Figure 3.5b, if the sampling frequency is increased proportional to the bandwidth. The observation in [38] is probably due to the constant sampling frequency and increasing aliasing for higher bandwidths.

If we account for RFI, wider bandwidths can indeed become disadvantageous. In case of CW and swept CW interference, for example, narrower bandwidths may potentially eliminate a portion of the interference power. In [39], after testing several receivers, the authors come accordingly to the conclusion that the front-end bandwidth has a greater impact on the tracking performance than the RFI signal type. However, narrow bandwidths broaden and flatten the correlation function at the same time [3]. With regard to multipath, this makes it harder to distinguish multipath from direct signals. The correlator spacing of the narrow early-late-discriminator, for example, should not be set less than the chip rate f_c divided by the front-end bandwidth B as a rule of thumb [3]. Since the maximum multipath error of the discriminator is proportional to the correlator spacing, front-end bandwidth is linked to the multipath mitigation performance of a receiver. Larger bandwidths are required to reduce multipath-induced biases [40] (Figure 4.18 and Figure 4.20 later in Section 4.3.3 provide a quantitative comparison of the front-end bandwidths 2 MHz and 4 MHz with regard to multipath induced ranging errors.).

If the received RF signal is downconverted to the baseband ($f_\mathrm{IF} = 0$) before ADC, the sampling frequency f_s must fulfill the Nyquist criterion $f_\mathrm{s} \geq 2f_\mathrm{UP}$ with f_UP the cutoff frequency (*baseband sampling*). However, most typically the RF signal is downconverted to an intermediate frequency. In this case, *bandpass sampling* may be applied:

$$f_\mathrm{s} = 2f_\mathrm{UP}/m \qquad \text{with} \quad m \in \mathbb{Z} \quad \text{and} \quad m \leq \lfloor f_\mathrm{UP}/B \rfloor .$$

In case of GNSS applications, it is crucial not to use sampling frequencies, that are a multiple of the chip rate f_c. If the satellite's code signal is sampled with a multiple of the chip rate f_c, several phases of the code have the same value of cross correlation [41]. Hence, the correlation triangle deforms to a step function, which leads to a distorted code phase discrimination function as a result. Further details on this topic are

discussed in [42].

3.3 Baseband Processing

Computation of the user position in a GNSS receiver is based on the estimated carrier frequencies and code delays of the different received satellite signals. In order to estimate and keep track of the code delay τ, the carrier frequency f, and the carrier phase θ of a satellite signal, the receiver generates a local replica

$$\hat{s}(t;\hat{f},\hat{\theta},\hat{\tau}) = \underbrace{\exp(j(2\pi\hat{f}t+\hat{\theta}))}_{\text{carrier}} \cdot \underbrace{c(t-\hat{\tau})}_{\text{code}}$$

of the satellite signal and computes the correlation

$$\varphi^T_{\hat{s}x}(t;\hat{f},\hat{\theta},\delta\tau) = \langle \hat{s}^*(t;\hat{f},\hat{\theta},\hat{\tau}-\delta\tau)\cdot x(t)\rangle_T = \frac{1}{T}\cdot\int_{t-T}^{t} \hat{s}^*(t';\hat{f},\hat{\theta},\hat{\tau}-\delta\tau)\cdot x(t')\,\mathrm{d}t' \tag{3.5}$$

between this local replica signal and the received signal $x(t)$ for N_{corr} different code delays $\delta\tau$, where T is the observation time. Correlation function in its discrete form is

$$\begin{aligned}\varphi^K_{\hat{s}x}(k;\hat{f},\hat{\theta},\delta\tau) &= \langle \hat{s}^*(kT_s;\hat{f},\hat{\theta},\hat{\tau}-\delta\tau)\cdot x(kT_s)\rangle_K \\ &= \frac{1}{K}\cdot\sum_{k'=k-K+1}^{k} \hat{s}^*(kT_s;\hat{f},\hat{\theta},\hat{\tau}-\delta\tau)\cdot x(kT_s) \quad \text{with} \quad K=\lfloor T/T_s\rfloor.\end{aligned} \tag{3.6}$$

Ideally the local signal replica is synchronized with the received satellite signal, i.e. $\hat{f}=f$, $\hat{\theta}=\theta$, $\hat{\tau}=\tau$. In following chapters, a parameter is omitted if it is synchronous with the received signal. In the case of an ideal synchronization, for example, the short notation $\hat{s}(t)=\hat{s}(t;\hat{f}=f,\hat{\theta}=\theta,\hat{\tau}=\tau)$ is used. Also the alias "prompt" correlator is used for $\mathcal{P}=\varphi^T_{\hat{s}x}(t;\delta\tau=0)$, i.e. for the correlation of $x(t)$ with the "prompt" signal replica $\hat{s}^*(t;\hat{f},\hat{\theta},\hat{\tau})$.

The "carrier-synchronized" correlation function $\varphi^T_{\hat{s}x}(t,\delta\tau)$ over $\delta\tau$ has a triangle shape with a peak value at $\delta\tau=0$ as shown in Figure 2.3 in the previous chapter. Furthermore,

$$|\varphi^T_{\hat{s}x}(t,\hat{f})|^2 = |\mathrm{sinc}(\pi T\cdot(f-\hat{f}))|^2$$

holds for the "code-synchronized" correlation function $\varphi^T_{\hat{s}x}(t,\hat{f})$ over $\hat{f}$, which has its peak value at $\hat{f}=f$ (Figure 3.6). Put in short terms, the task of the baseband processing

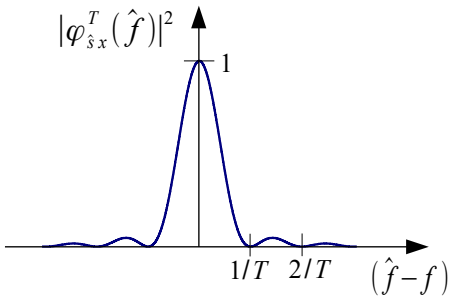


Figure 3.6: "Code-synchronized" correlation function $\varphi^T_{\hat{s}x}(t, \hat{f})$ over frequency estimate $\hat{f}$

is to continuously maximize these two functions. See Appendix A for further details on this so called *tracking* procedure.

The correlation is divided into *carrier wipe-off* and *code wipe-off*. *Carrier wipe-off* is the process of mixing the complex input signal $x(t)$ with the carrier of the local signal replica in order to downconvert the satellite signal to the baseband. *Code wipe-off* is the process of mixing the input signal with the local code signal and integrating over time. Figure 3.7 illustrates the PSD of noise and the satellite signal after these different stages of correlation.

With (2.3) and neglecting the quantization loss and the fine structure of the PSD, the signal power after correlation is

$$P_s = \mathrm{E}\{\mathcal{P}\}^2 = C \cdot T_\mathrm{c} \int_{-B/2}^{B/2} |\mathrm{sinc}(\pi f T_\mathrm{c})|^2 \,\mathrm{d}f \tag{3.7}$$

with B the front-end bandwidth. C is the the signal power after analog signal conditioning. $P_s = C$ for $B \to \infty$. The noise power after correlation is

$$P_n = \mathrm{E}\{|\mathcal{P} - \mathrm{E}\{\mathcal{P}\}|^2\} = \frac{N_0}{T}, \tag{3.8}$$

as $1/T$ is the two-sided noise equivalent bandwidth of an integrator filter over the period T and $1/T << B$. $N_0/2$ is the noise power density. Not the total noise power $N_0 B$ before correlation but the noise power density $N_0/2$ and the integration time T determine the SNR $= P_s/P_n$ after correlation.

The block diagram in Figure 3.8 illustrates the implementation of the correlation process in hardware. The correlator channel computes the correlation values for an odd number of N_corr equidistant code delays. Different code delays in the local signal are realized using a shift register. Two numerically controlled oscillators (NCO) generate the carrier frequency and the chipping rate. While the carrier values are read out from a Look-Up-Table (LUT), the code is generated using feedback linear shift registers as mentioned in Section 2.1.

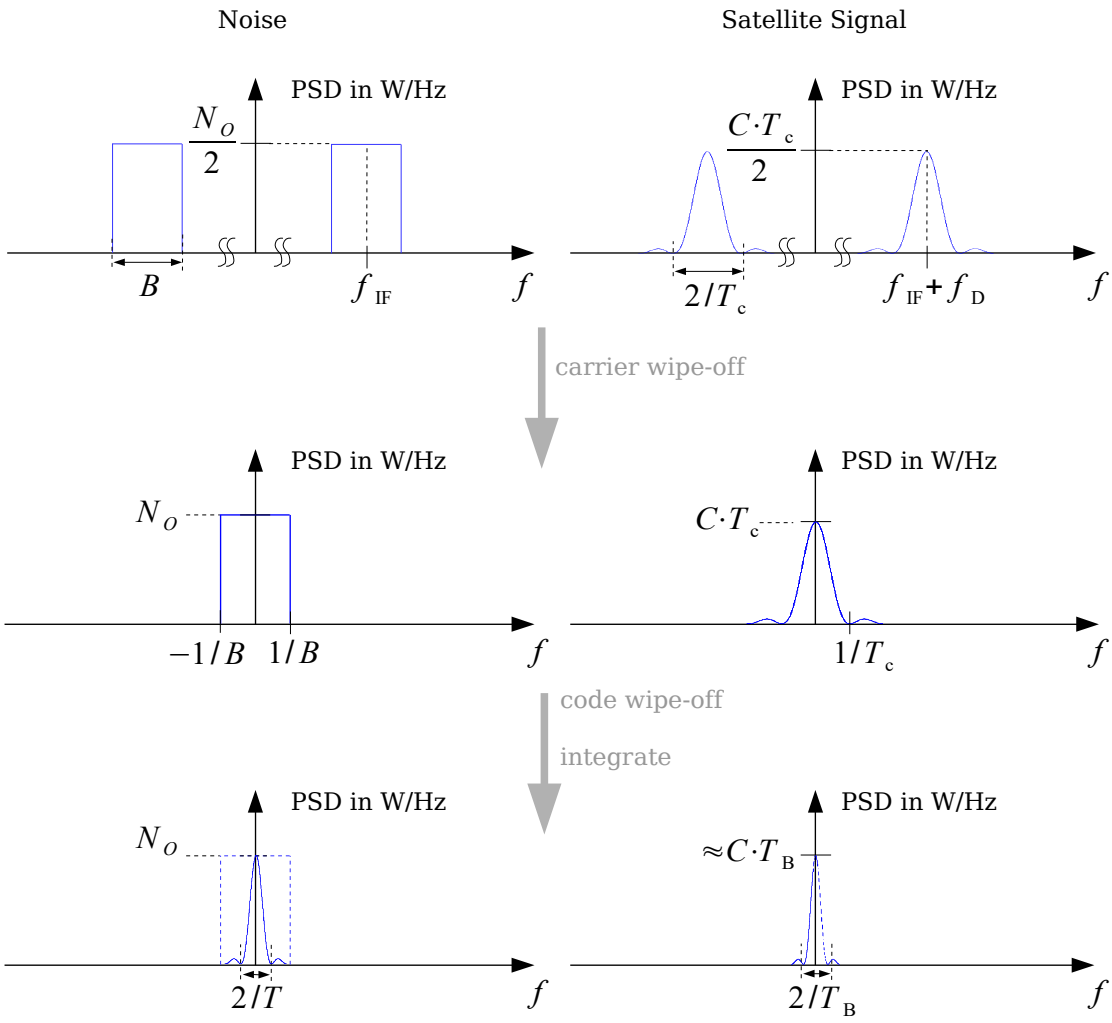


Figure 3.7: Baseband Processing

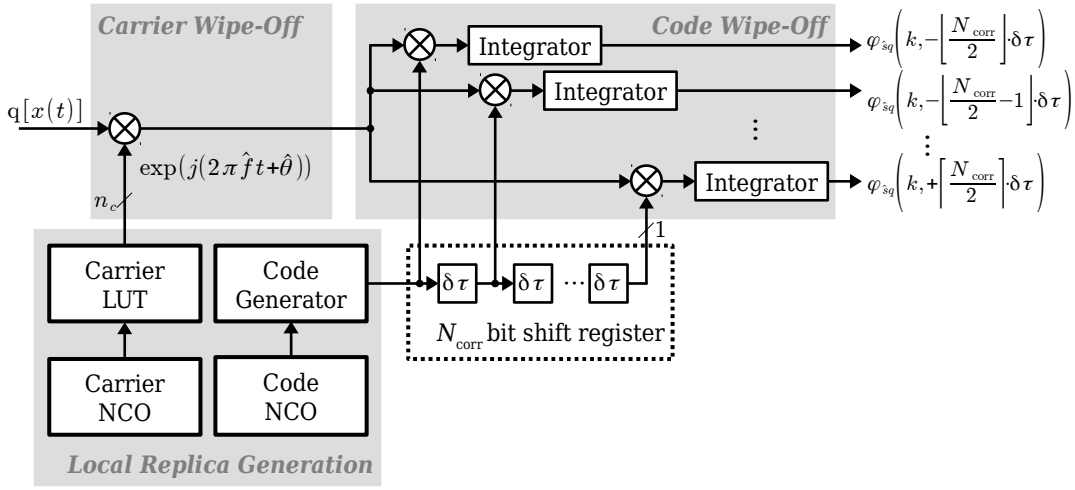


Figure 3.8: Single-antenna correlator channel

	Combinational	Registers	Total	
Carrier NCO	80	96	176	
Code NCO	86	91	177	
Code Generator	66	94	160	
Code & Carrier Wipe-Off	242	192	434	$\propto N_{\text{corr}} \cdot N_{\text{ant}}$
Other	182	192	374	$\propto N_{\text{ant}}$
Total	656	665	1321	

Table 3.2: Number of LCs ($N_{\text{corr}} = 3$, $n_x = n_c = 2$)

In Table 3.2 the synthesis results of one correlator channel are given, if the correlator channel is synthesized on a Cyclone V Altera FPGA (5CSEMA4U23C6) [43]. A distinction is made between LCs that are used for combinational logic and LCs that are used as registers. While the local replica generation consisting of the carrier NCO, code NCO and the code generator is required once per channel, the implementation cost of the code wipe-off path is nearly proportional to the number of computed correlation values N_{corr}. In case of multi-antenna reception, the input signal $\mathbf{x}(t)$ of the correlation channel is a vector of size N_{ant}. This translates into one code & carrier wipe-off chain for each additional antenna.

Chapter 4

Beamforming

In the case of a single-antenna receiver, narrowband interference can be mitigated in the frequency or time domain. Broadband interference, however, can effectively be dealt with in the spatial domain using multi-antenna receivers. Adaptive beamforming is the process of combining the signals from different antenna-elements (decoupled from the tracking loops) in order to form beams and zeros in the gain pattern of the multi-antenna. The objective is to adapt the gain pattern to the signal environment, so that interference and multipath signals are rejected and direct signals from the satellites are amplified.

Beamforming can take place at various stages of the signal processing chain: In the analog hardware, or in the digital domain (hardware or software); before correlation [44] or after correlation [20], or split into multiple steps distributed between the different stages as in [28]. In contrast to beamforming in analog hardware, digital beamforming allows for independent array gain patterns in different correlation channels. This has the advantage that a different gain pattern can be generated in each channel, each of which is adjusted for optimum reception of a specific satellite signal [45].

Beamforming approaches can be grouped into three different categories. Beamformers in the first category are those, that compute the steering vectors of the satellite signals and thereafter the beamforming coefficients based on the satellite positions. The satellite positions are indeed known by the receiver, as the ephemeris are included in the navigation messages. In addition to the satellite positions, however, the receiver must accurately estimate or be provided with the antenna orientation in order to determine the DOAs relative to the antenna. For that reason, this type of beamforming is not practical for dynamic stand alone operation [31]. The second category includes beamformers such as the ones in [45, 46], which are supported by DOA estimation algorithms like ESPRIT [47] or MUSIC [48]. These algorithms provide an estimate of the

signal directions relative to the antenna. A further estimation of the antenna orientation is not required.

The deterministic beamformer, the Minimum Variance Distortionless Beamformer (MVDR) and the Minimum Power Distortionless Beamformer (MPDR) from Section 4.1 can be used for both of these two categories. A modified version of the MPDR employing several overlapping sub-arrays is proposed in [49, 50]. This beamformer is designed to reject reflected signals to deal with multipath reception. Among other additional computations it requires a pre-filtering stage, computation of two covariance matrices (one before and one after pre-filtering) instead of one and the Eigenvalue EigenVector Decomposition (EVD) of the covariance matrix. Hence, its computational cost (in hardware and software) is significantly higher than the conventional MPDR.

The Linearly Constrained Minimum Variance Beamformer (LCMV) can be used for the second category. In addition to the DOAs of the satellite signals, the LCMV can take the estimated DOAs of the interference and multipath also into account and purposefully put zeros into the adaptive gain pattern in order to suppress undesired signal directions. The LCMV presented in [51] is slightly simplified. It does not require the estimation of the interference and multipath directions, but suppresses low elevations in general to reject ground interference and ground multipath. The result is similar to the antenna techniques presented in Section 3.1. The Iterative Adaptive Approach (IAA) in [52] is also worth mentioning, that combines the DOA estimation and the beamforming into one iterative algorithm. It defines a scanning grid of directions, computes iteratively beamforming weights looking into one direction and suppressing all others. Finally, the weight vector of the grid direction is selected, that corresponds to the assumed DOA.

Beamformers mentioned in the first two categories so far must exactly reproduce the steering vector observed after analog signal conditioning for all possible signal directions. The steering vector is not only determined by the signal direction and the antenna geometry, but also by the antenna radiation pattern and the front-end characteristics in reality as discussed in Section 3.2. Therefore, a calibration procedure is required to measure and model the true steering vectors for different DOAs. For this purpose, [31] uses recorded data for calibration. [20, 25, 26] use a calibration signal injected into the signal path for online calibration (see Section 3.1.1). Further, [51] proposes the use of a calibration matrix to model the antenna coupling effects. The calibration matrix is measured in advance and taken into account for corrections in the beamforming algorithm.

The last category is the category of *blind* beamformers, that do not require any knowledge about the antenna geometry or signal directions or any kind of calibration.

The MMSE requires only the waveform of the desired signal to be known as it is the case for GNSS. The MMSE is susceptible to multipath, since it may combine multipath signal with the direct signal in order to increase the total signal power. [53] applies a weighted linear combination of the MVDR and the MMSE to improve this behavior. However, because of the use of the MVDR, this approach cannot be described as blind any more. Instead, this thesis presents a slightly modified version of the MMSE in Section 4.3.3, which is more immune against multipath. Power Minimization (PM) filter [54], that ignores the desired signal directions as a disadvantage and only suppresses strong interference, can also be counted to the blind beamformers.

As an alternative to the beamforming techniques, also parametric methods exist. These methods exploit the underlying signal model as in (3.4) and estimate the unknown parameters of the received satellite signals such as the code delay and the carrier frequency together with the DOA. That requires a complex multi-dimensional search to find the estimates [55]. The Space Alternating Generalized Expectation Maximization (SAGE) algorithm [56] is one of the most common algorithms applied for this purpose. It computes the *maximum likelihood* estimates of the desired signal parameters. [45] compares SAGE against LCMV and MMSE and concludes that SAGE is indeed more robust against multipath. However, due to its computational cost and memory requirements, SAGE is hard to implement for real time operation [57]. With a purpose of reducing the computational complexity, [57] applies SAGE after correlation. The SAGE algorithm also requires antenna/front-end calibration.

This thesis focuses on blind beamformers due to their computational efficiency and ease of implementation. It differentiates from previous work by putting special attention on quantization. It discusses how quantization influences the performance and the implementation cost of digital beamforming.

After giving a brief overview of the different beamformers in Section 4.1, the relation between quantization precision and the Signal-to-Noise-plus-Interference-Ratio (SNIR) after correlation is discussed in Section 4.2. Section 4.3 presents a 2-step beamforming approach. In particular, Subsection 4.3.1 answers the question, where to realize beamforming in the processing chain in order to reduce the implementation cost. The considerations justify the 2-step approach with pre-correlation interference mitigation as presented in Subsection 4.3.2 and post-correlation multipath mitigation as presented in Subsection 4.3.3. Finally, Section 4.4 addresses the potential of combining beamforming techniques with Vector Tracking Loops (VTL).

4.1 Beamformers

With $\mathbf{x}$ being the complex N_{ant}-dimensional output of analog signal conditioning given by (3.4), the output of a beamformer is defined as

$$z = \mathbf{w}^{\mathrm{H}} \cdot \mathbf{x},$$

where $\mathbf{w}$ is the complex beamforming vector. In general, beamforming provides a maximum gain factor of N_{ant} in the Signal-to-Noise-Ratio (SNR) relative to single-antenna reception.

Different optimization criteria result in different beamformers. An overview of those are given in the following subsections. The deterministic beamformer, the MVDR and the MPDR (Sections 4.1.1, 4.1.2, 4.1.3) are well-suited to situations with known DOAs and antenna response but unknown reference signal waveforms. The LCMV (Section 4.1.4) may additionally take interference directions into account, in case they are known or estimated. The performance of these beamformers are negatively impacted by channel errors, line biases, or unmodeled antenna effects [58]. The MMSE (Section 4.1.5) is convenient if the reference waveforms, i.e. satellite signals in case of GNSS, are known but DOAs are not. It does not require any knowledge about the antenna response. The projection matrix introduced in Subsection 4.1.6 is a replacement for the inverse of the auto-covariance matrix $\mathbf{R}_{\mathbf{xx}}$ of the input signal $\mathbf{x}$. It can be used in all mentioned beamformers instead of $\mathbf{R}_{\mathbf{xx}}^{-1}$ in case of strong interference. The PM (Section 4.1.7) approach requires neither the DOAs nor the reference waveforms. Its exclusive task is to minimize the signal power in order to suppress the interference signals.

4.1.1 Deterministic Beamformer

The deterministic beamformer (also known as the conventional or the Bartlett beamformer [59]) maximizes the power from a given signal direction while keeping the noise power constant, if the noise is assumed to be spatially white. This constraint about the noise means $|\mathbf{w}_{\text{det}}| = 1$ for the beamforming vector $\mathbf{w}_{\text{det}}$. With $\mathbf{a}$ being the steering vector of the desired signal, the beamforming vector is given by [55]

$$\mathbf{w}_{\text{det}} = \frac{\mathbf{a}}{\sqrt{\mathbf{a}^{\mathrm{H}}\mathbf{a}}}. \tag{4.1}$$

Since the deterministic beamformer focuses only on maximizing the power of the desired signal, it does not control sidelobes and nulls in the beam pattern. Thus, it may not adequately suppress interference or multipath [58].

4.1.2 MVDR: Minimum Variance Distortionless Beamformer

The minimum variance distortionless (MVDR) beamformer (also known as the Capon's beamformer [60]) attempts to minimize the power contributed by noise and any signals coming from other directions than a particular single look direction. As a constraint, it maintains a fixed unity gain in the look direction ($\mathbf{w}_{\text{MVDR}}^{\text{H}} \cdot \mathbf{a} = 1$) [55]. The MDVR beamformer maximizes the SINR and hence the array gain [61].

In case the desired signal and the interference signals are uncorrelated and the noise is spatially white,

$$\mathbf{R_{xx}} = \mathrm{E}\{\mathbf{x} \cdot \mathbf{x}^{\text{H}}\} = \mathbf{a} \cdot \sigma_s^2 \cdot \mathbf{a}^{\text{H}} + \underbrace{\sum_i \mathbf{b}_i \cdot \sigma_i^2 \cdot \mathbf{b}_i^{\text{H}} + \sigma_n^2 \cdot \mathbf{I}}_{=\mathbf{R}_{\text{N+I}}}$$

applies to the auto-covariance matrix $\mathbf{R_{xx}}$, where $\mathbf{a}$ is the steering vector of the desired signal, $\mathbf{b}_i$ are the steering vectors and σ_i^2 the powers of the interference signals, and σ_n^2 is the noise power. $\mathbf{R}_{\text{N+I}}$ is the auto-covariance matrix resulting exclusively from the interference signal and the noise (excluding the satellite signal). The beamforming vector of the MVDR beamformer is

$$\mathbf{w}_{\text{MVDR}} = \mu \cdot \mathbf{R}_{\text{N+I}}^{-1} \cdot \mathbf{a} \quad \text{with } \mu = \frac{1}{\mathbf{a}^{\text{H}} \cdot \mathbf{R}_{\text{N+I}}^{-1} \cdot \mathbf{a}}. \tag{4.2}$$

A recursive way to compute $\mathbf{w}_{\text{MVDR}}$ is to add the correction vector

$$\Delta\mathbf{w}_{\text{MVDR}} = \gamma \cdot (\mu \cdot \mathbf{a} - \mathbf{R}_{\text{N+I}} \cdot \mathbf{w}_{\text{MVDR}})$$

to it at the end of each update period, where $\gamma > 0$ is the step size parameter controlling the convergence speed of the algorithm [62].

The MVDR requires the exact knowledge of the steering vector of the satellite signal of interest. In the presence of signal direction mismatch or antenna/front-end modeling errors, the SNIR gain of the MVDR is dramatically degraded [63, 64].

Not only for the mentioned criterion but for a wide class of criteria the optimum beamformer is an MVDR beamformer followed by a scalar depending on the criterion. For instance, under the assumption that the noise is a circular complex Gaussian random vector the maximum likelihood estimate of the source signal is identical to the output of the MVDR beamformer [61]. The MPDR and the MMSE from the following two subsections are theoretically also equal to the MVDR. Differences arise in practice due to e.g. steering vector mismatch or numerical approximations in the implementation.

4.1.3 MPDR: Minimum Power Distortionless Beamformer

The attempt to minimize the total output power, while maintaining a fixed gain in the look direction, results in the minimum power distortionless (MPDR) beamformer. The beamforming vector of the MPDR beamformer is also given by (4.2) if $\mathbf{R}_{\text{N+I}}$ is replaced by $\mathbf{R}_{\mathbf{xx}}$:

$$\mathbf{w}_{\text{MPDR}} = \mu \cdot \mathbf{R}_{\mathbf{xx}}^{-1} \cdot \mathbf{a} \qquad \text{with} \quad \mu = \frac{1}{\mathbf{a}^{\mathbf{H}}\mathbf{R}_{\mathbf{xx}}^{-1}\mathbf{a}}. \tag{4.3}$$

Due to their close similarity, the MPDR is also referred to as MVDR in the majority of the literature [61], e.g. in [55], [58].

MVDR and MPDR are equivalent as long as there is no mismatch between the estimated steering vector and the true steering vector. However, in case of a steering vector mismatch the MVDR beamformer outperforms the MPDR beamformer in general. The differences are insignificant for GNSS applications, as the effect of the satellite signals on the auto-covariance matrix is negligible because of their relatively low power, i.e. $\mathbf{R}_{\text{N+I}} \backsimeq \mathbf{R}_{\mathbf{xx}}$.

4.1.4 LCMV: Linearly Constrained Minimum Variance Beamformer

The linearly constrained minimum variance (LCMV) beamformer is an extended version of the MPDR in the sense that it extends the constraints from one signal direction to multiple signal directions (here L). The beamforming vector of the LCMV beamformer is subject to the linear constraint

$$\mathbf{w}_{\text{LCMV}}^{\text{H}} \cdot \mathbf{A} = \mathbf{g}^{\text{H}} \quad \text{with } \mathbf{A} = \begin{bmatrix} \mathbf{a}_1 & \cdots & \mathbf{a}_L \end{bmatrix},$$

where $\mathbf{A}$ contains steering vectors $\mathbf{a}_i$ for the different directions ($i = 1, \cdots, L$) and $\mathbf{g}$ specifies the desired antenna gain for each direction. $\mathbf{A}$ may contain both desired signal directions and undesired interference directions. A reasonable choice for $\mathbf{g}$ would be to set its corresponding elements equal to one for a distortionless reception in desired directions and to set its remaining elements equal to zero for suppressing undesired directions. The beamforming vector of the LCMV is given by

$$\mathbf{w}_{\text{LCMV}} = \mathbf{R}_{\mathbf{xx}}^{-1}\mathbf{A}\left(\mathbf{A}^{\text{H}}\mathbf{R}_{\mathbf{xx}}^{-1}\mathbf{A}\right)^{-1}\mathbf{g}.$$

Arrival directions of the satellite signal can be computed deterministically based on ephemeris data in the navigation message and the antenna orientation provided by e.g. an external compass. In contrast, interference directions cannot be determined in a similar way. If they are taken into account by the LCMV, they must be necessarily estimated by a separate DOA estimation algorithm.

4.1.5 MMSE: Minimum Mean-Square Error Beamformer

The MMSE minimizes the mean square difference between a desired reference signal and the beamformer output. The reference signal in case of GNSS is the satellite signal, the waveform of which is precisely known by the receiver. The beamforming vector of the MMSE is given by

$$\mathbf{w}_{\text{MMSE}} = \mathbf{R}_{\mathbf{xx}}^{-1} \cdot \mathrm{E}\{\hat{s}^* \cdot \mathbf{x}\}\,, \tag{4.4}$$

where $\hat{s}$ is the locally generated reference satellite signal replica. $\hat{s}$ is synchronized with the received satellite signal by the tracking procedure.

The expectation value $\mathrm{E}\{\hat{s}^* \cdot \mathbf{x}\}$ in (4.4) is equal to the steering vector of the satellite signal in case there is no multipath or any other coherent interference. An approximation of this term is

$$\mathrm{E}\{\hat{s}^* \cdot \mathbf{x}\} \approx \boldsymbol{\varphi}_{\hat{s}\mathbf{x}}^T(t; \delta\tau = 0),$$

where $\boldsymbol{\varphi}_{\hat{s}\mathbf{x}}^T$ is the correlation between the local signal replica $\hat{s}$ and the front-end output $\mathbf{x}$ as defined by (3.5). $\boldsymbol{\varphi}_{\hat{s}\mathbf{x}}^T$ is already computed in the correlation module as part of the tracking procedure and can be used also for beamforming.

A recursive way to compute $\mathbf{w}_{\text{MMSE}}$ is to add the correction vector

$$\Delta\mathbf{w}_{\text{MMSE}} = \gamma \cdot (\mathrm{E}\{\hat{s}^* \cdot \mathbf{x}\} - \mathbf{R}_{\mathbf{xx}} \cdot \mathbf{w}_{\text{MMSE}}) = \gamma \cdot (\mathrm{E}\{\hat{s}^* \cdot \mathbf{x}\} - \mathbf{R}_{\mathbf{xz}})$$

to it at the end of each update period [62], where γ is the step size parameter of the algorithm.

In contrast to the previously presented beamformers, MMSE does not require any knowledge about the DOAs or the antenna/front-end response. In this sense, it is a *blind* beamformer. It yields SINRs that are only a few tenths of a dB less than those given using the MPDR beamformer [65]. However, MMSE may be susceptible to multipath-induced errors, since it tends to constructively combine multipath signals with the direct signal [57, 58].

An extended version of the MMSE, which is more immune to multipath, is presented in Section 4.3.3. To distinguish the MMSE from its extended version, the MMSE is denoted also as the Minimum Mean-Square *Signal* Error Beamformer (MMS**S**E). The name stresses the optimization criterion to minimize the differences between two "signals", the reference satellite signal and the beamformer's output signal.

4.1.6 Projection

GNSS signals are weak compared to the noise power. Hence, their effect on the covariance matrix $\mathbf{R_{xx}}$ is negligible. The following holds for the eigenvalue/eigenvector decomposition (EVD) of $\mathbf{R_{xx}}$ if strong interference (interference power $\gg$ noise power σ_n^2) is present:

$$\mathbf{R_{xx}} = \mathbf{U} \cdot \mathbf{\Lambda} \cdot \mathbf{U}^{\mathrm{H}} \approx \mathbf{R}_{\mathrm{N+I}} = \begin{bmatrix} \mathbf{U}_{\mathrm{I}} & \mathbf{U}_{\mathrm{N}} \end{bmatrix} \left(\begin{bmatrix} \tilde{\lambda}_1 & & \mathbf{0} \\ & \ddots & \\ & & \tilde{\lambda}_{N_{\mathrm{I}}} \\ \mathbf{0} & & \mathbf{0} \end{bmatrix} + \sigma_n^2 \cdot \mathbf{I} \right) \begin{bmatrix} \mathbf{U}_{\mathrm{I}}^{\mathrm{H}} \\ \mathbf{U}_{\mathrm{N}}^{\mathrm{H}} \end{bmatrix}.$$

The columns of $\mathbf{U}_{\mathrm{I}}$ are eigenvectors of $\mathbf{R_{xx}}$ that span the *interference subspace*. Among all eigenvectors of $\mathbf{R_{xx}}$ they can be identified by comparing their corresponding eigenvalues $\lambda_i = \tilde{\lambda}_i + \sigma_n^2$ with a threshold value $\lambda_{\mathrm{thr}} \gtrsim \sigma_n^2$. If N_{I} uncorrelated interference signals from distinct directions are received, N_{I} eigenvectors belong to the interference subspace, i.e. $\mathbf{U}_{\mathrm{I}}$ has N_{I} columns. The columns of $\mathbf{U}_{\mathrm{N}}$ are the remaining $(N_{\mathrm{ant}} - N_{\mathrm{I}})$ eigenvectors that belong to the *noise subspace*.

The inverse of the covariance matrix $\mathbf{R_{xx}}$, which is used in all presented beamformers so far, can be computed as

$$\mathbf{R_{xx}^{-1}} = \mathbf{U} \cdot \mathbf{\Lambda}^{-1} \cdot \mathbf{U}^{\mathrm{H}} = \mathbf{U} \cdot \begin{bmatrix} 1/\lambda_1 & & \mathbf{0} \\ & \ddots & \\ \mathbf{0} & & 1/\lambda_{N_{\mathrm{ant}}} \end{bmatrix} \cdot \mathbf{U}^{\mathrm{H}}$$

based on the EVD of $\mathbf{R_{xx}}$. In case that the interference signals are very strong compared to the noise ($\lambda_i \gg \sigma_n^2$),

$$\mathbf{\Lambda}^{-1} \approx \frac{1}{\sigma_n^2} \cdot \mathbf{S} = \frac{1}{\sigma_n^2} \cdot \begin{bmatrix} S_{11} & & \mathbf{0} \\ & \ddots & \\ \mathbf{0} & & S_{N_{\mathrm{ant}}N_{\mathrm{ant}}} \end{bmatrix} \quad \text{with} \quad S_{ii} = \begin{cases} 0 & \text{if } \lambda_i > \lambda_{\mathrm{thr}} \\ 1 & \text{if } \lambda_i \leq \lambda_{\mathrm{thr}} \end{cases} \tag{4.5}$$

applies, where $\mathbf{S}$ is a diagonal "selection matrix". $\mathbf{S}$ lets eigenvectors with a small corresponding eigenvalue λ_i (noise eigenvectors) through while zeroing others (interference eigenvectors). Consequently, $\mathbf{R_{xx}^{-1}}$ can be approximated as follows:

$$\mathbf{R_{xx}^{-1}} \approx \frac{1}{\sigma_n^2}\mathbf{P}^{\perp} = \mathbf{U} \cdot \mathbf{S} \cdot \mathbf{U}^{\mathrm{H}} = \frac{1}{\sigma_n^2}\mathbf{U}_{\mathrm{N}} \cdot \mathbf{U}_{\mathrm{N}}^{\mathrm{H}} = \frac{1}{\sigma_n^2}\left(\mathbf{I} - \mathbf{U}_{\mathrm{I}} \cdot \mathbf{U}_{\mathrm{I}}^{\mathrm{H}}\right). \tag{4.6}$$

$\mathbf{P}^{\perp}$ is called a *projection matrix*. The signal

$$\mathbf{y}^{\perp} = \mathbf{P}^{\perp} \cdot \mathbf{x}$$

is the projection of the input signal $\mathbf{x}$ onto the interference-free noise subspace.

The use of the projection matrix $\mathbf{P}^{\perp}$ for interference mitigation in place of $\mathbf{R}_{\mathbf{xx}}^{-1}$ is proposed, e.g., in [28, 66, 67, 68, 69, 70]. However, one should keep in mind, that $\mathbf{P}^{\perp}$ approximates $\mathbf{R}_{\mathbf{xx}}^{-1}$ if and only if interference is strong compared to noise. $\mathbf{R}_{\mathbf{xx}}^{-1}$ or $\mathbf{P}^{\perp}$ are both responsible for generating notches in the adaptive gain pattern in the directions of the interference signals. When the DOA of a satellite signal is close to an interference direction, its reception power is also affected by the attenuation of a notch [67]. While the "depth" of the notches generated by $\mathbf{R}_{\mathbf{xx}}^{-1}$ is limited (> 0) and adapted to the power of the interference signals, $\mathbf{P}^{\perp}$ generates absolute zeros in the gain pattern regardless how strong the interference is. Hence, in the presence of weak interference signals, the projection approach is disadvantageous compared to using $\mathbf{R}_{\mathbf{xx}}^{-1}$ [71].

4.1.7 PM: Power Minimization

GNSS signals are below the noise floor as discussed in Section 3.2, i.e. the input signal $\mathbf{x}$ of the beamformer is dominated by noise, if there is no strong interference. In this case (and if the noise is assumed to be spatially white) the elements of $\mathbf{x}$ are nearly uncorrelated and, thus, the non-diagonal elements of $\mathbf{R}_{\mathbf{xx}}$ are nearly zero.

Spatial correlations in $\mathbf{x}$ indicate the presence of interference with distinct signal directions. Therefore, removing any spatial correlation from the input signal by spatial filtering and minimizing the power $\mathrm{E}\{|z|^2\}$ at the filter output down to the noise floor results in the removal of strong interference signals. The PM filter [54, 72] used for this purpose is a special case of the MPDR beamformer. The beamforming vector $\mathbf{w}_{\mathrm{PM}}$ of the PM filter is given by (4.3), if the steering vector $\mathbf{a}$ is replaced by $\boldsymbol{\delta}$, which is a zero vector except for the i_{ref}-th element (reference) $\delta_{i_{\mathrm{ref}}} = 1$. $\mathbf{w}_{\mathrm{PM}}$ is the i_{ref}-th column of $\mathbf{R}_{\mathbf{xx}}^{-1}$ divided by the diagonal element $[\mathbf{R}_{\mathbf{xx}}^{-1}]_{i_{\mathrm{ref}},i_{\mathrm{ref}}}$.

The disadvantage of the PM filter is that it does not exploit any information on the satellite directions. Furthermore, it does not explicitly exploit the fact that each interferer arrives as a plane wave at a single discrete angle [54]. The PM filter *blind*ly removes any significant spatial correlation detected in the input signal $\mathbf{x}$. In constrast to previously presented beamformers, it does not "care" about the effect of beamforming on the satellite signals. In that sence, it is a blind but sub-optimum beamformer.

The most important advantage of the PM beamformer is its simple formulation

based on

$$z = y_{i_{\text{ref}}} = \underbrace{x_{i_{\text{ref}}}}_{\text{“reference”}} + \underbrace{\sum_{i,i\neq i_{\text{ref}}} w_i^* x_i}_{\text{“estimate”}}, \tag{4.7}$$

where x_i are the elements of $\mathbf{x}$ and w_i the elements of $\mathbf{w}_{\text{PM}}$. i_{ref}-th element of the antenna is chosen as the reference element and its output may be interpreted as the “reference signal”. An estimate of the desired “reference signal” is formed from the auxiliary antenna-elements and subtracted from the reference signal in order to remove spatially correlated interference. The mean square difference between the estimate and the reference needs to be minimized in order to minimize the power of the output signal z.

This formulation leads to the following LMS based algorithm for adapting the weights on a continual basis:

$$\mathbf{w}_{\text{PM}}(k) = \mathbf{w}_{\text{PM}}(k-K) + \Delta\mathbf{w}_{\text{PM}}(k) \quad \text{with} \quad \Delta w_i(k) = -\mu \cdot \varphi^K_{x_i z}(k; \delta\tau = 0). \tag{4.8}$$

The weighting vector $\mathbf{w}_{\text{PM}}$ is periodically updated with a period of K samples by adding a correction term $\Delta\mathbf{w}_{\text{PM}}$. The elements of $\Delta\mathbf{w}$ are derived from the correlation $\varphi^K_{x_i z}$ between the input signal $\mathbf{x}$ and the output signal z as defined by (3.6). μ is the step size parameter, which determines the convergence speed of the LMS algorithm. According to [73], convergence of a gradient-based filter adaptation is guaranteed if the step-size parameter μ satisfies

$$0 < \mu < 2/\text{input-power} \tag{4.9}$$

with

$$\text{input-power} = \mathrm{E}\{|\mathbf{x}|^2\} \approx \langle |\mathbf{x}(k)|^2 \rangle_K.$$

The LMS based algorithm eliminates the computationally intensive inversion of the covariance matrix $\mathbf{R_{xx}}$.

Section 3.2 concluded that a relatively coarse signal resolution (2-3 bits) is sufficient for quantizing the GNSS signals before digital processing. This is not the case if strong interference is present in the input signal $\mathbf{x}$ (see Section 4.2 for further details). As PM suppresses interference signals to the noise level, we are allowed to reduce the resolution of the beamformer's output $\mathbf{y}$ immediately after PM to its normal levels as if there was no interference existent but only noise. Consequently, like in all following processing stages, we can replace $z(k)$ in the computation of the correlation value $\varphi^K_{x_i z}$ by its

coarsely quantized version $\mathrm{q}\{z(k)\}$ in order to reduce the computational complexity of the correlation. If done so (4.8) becomes

$$\Delta w_i(k) \approx \tilde{\Delta w}_i(k) = -\tilde{\mu} \cdot \varphi^K_{x_i \mathrm{q}\{z\}} = -\tilde{\mu} \cdot \langle x_i^*(k) \cdot \mathrm{q}\{z(k)\} \rangle_K \tag{4.10}$$

with the modified step size

$$\tilde{\mu} = \frac{\sigma_z}{\sigma_q} \cdot \mu = \frac{\sqrt{\langle |z(k)|^2 \rangle_K}}{\sigma_q} \cdot \mu.$$

This way the use of the high precision signal $z(k)$ in (4.8) is avoided. However, the computation of the standard deviation σ_z of $z(k)$ is required. The standard deviation σ_q of $\mathrm{q}\{z(k)\}$ is a constant value (determined by the word length of the quantizer and $q_{\max}$ and $q_{\min}$ as defined in Figure 3.4) and it does not need to be computed explicitly.

4.2 Quantization

Analogous to the discussion in Section 3.2.2 for the single-antenna receiver, this section discusses the effect of the quantization on the beamforming performance. While Section 4.2.1 studies the quantization of the input signal in the presence of strong interference, Section 4.2.2 analyses the quantization of the beamforming coefficients.

4.2.1 Quantization of the input signal

In Section 3.2, it was shown for the single antenna receiver that a small number of bits is sufficient to digitize the received signal, provided that there is no interference. There is practically no use in increasing the word length above 3 bits as the SNR loss cannot be further reduced by improving the quantization precision. However, this does not hold for a multi-antenna receiver in the presence of strong interference. The effectiveness of beamforming against interference depends significantly on the signal resolution before beamforming.

To demonstrate the relation between the quantization of the input signal and the beamforming performance, the two-dimensional scenario as illustrated in Figure 4.1 is examined in this section. A satellite signal ($C/N_0 = 45.7$ dBHz) arriving from zenith and a strong broadband noise interference with a power density of I_0 from horizon are received by a 2-element antenna with a $\lambda/2$-element-spacing.

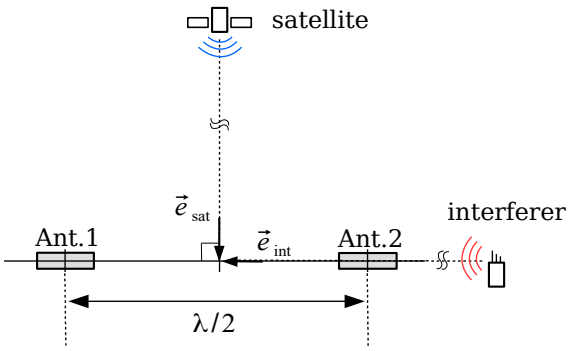


Figure 4.1: Experimental constellation

The steering vector $\mathbf{a}$ of the satellite signal and the steering vector $\mathbf{b}$ of the interference signal,

$$\mathbf{a} = [1, 1]^{\mathrm{T}} \text{ and } \mathbf{b} = [1, -1]^{\mathrm{T}},$$

are orthogonal in this case. Hence, the deterministic beamforming vector $\mathbf{w}_{\text{det}}$ given by (4.1) perfectly suppresses the interference signal, i.e. $\mathbf{w}_{\text{det}}^{\mathrm{H}} \cdot \mathbf{b} = 0$, if the input signal $\mathbf{x}$ is not quantized. In this case, the SNIR after beamforming

$$\text{SNIR} = \frac{\mathrm{E}\{s^* \cdot \mathrm{q}\{z\}\}^2}{\mathrm{E}\{|s|^2\} \cdot \mathrm{E}\{|\mathrm{q}\{z\}|^2\}} \qquad \text{with} \quad z = \mathbf{w}_{\text{det}}^{\mathrm{H}} \cdot \mathbf{x}$$

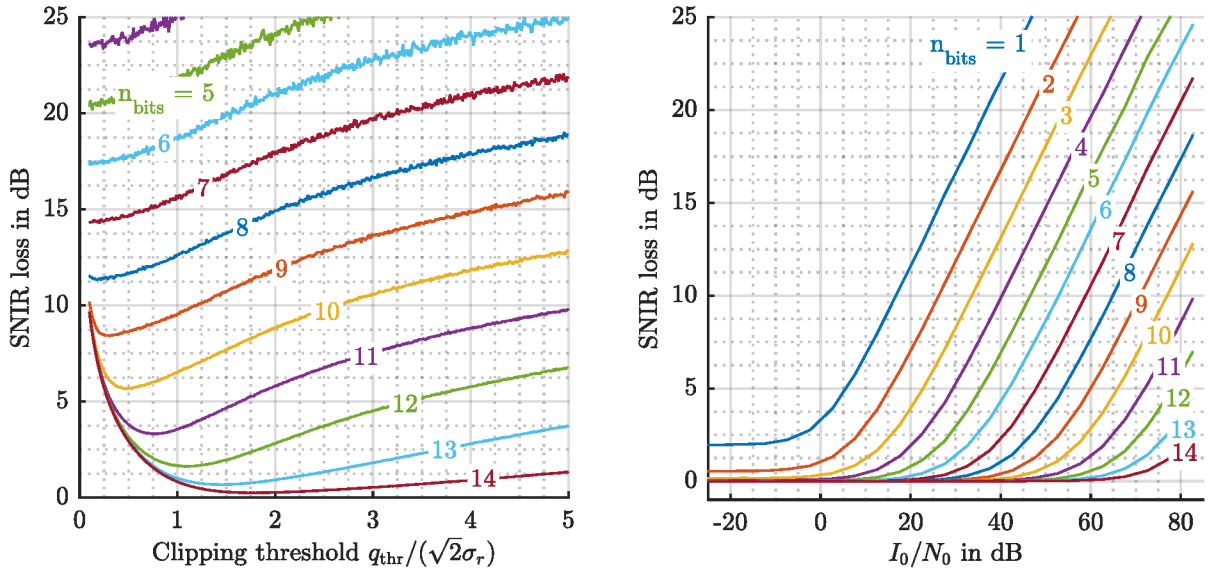
reaches its maximum possible value

$$\text{SNIR}_{\text{max}} = \text{SNR}_{\text{max}} = N_{\text{ant}} \cdot \frac{1}{B} \cdot \frac{C}{N_0} = N_{\text{ant}} \cdot \text{SNR}_{\text{max,1-ant}},$$

where B is the signal bandwidth after analog conditioning (Nyquist-sampling: $f_{\text{s}} = B$).

Quantization reduces the resolution of the input signal $\mathbf{x}$ and causes an SNIR loss ($\text{SNIR}_{\text{max}}/\text{SNIR} > 1$). In Figure 4.2a the SNIR loss due to quantization is plotted for a constant Interference-to-Noise Ratio (INR) of I_0/N_0 = 68 dB and for different quantization word lengths n_{bits} as a function of the clipping threshold q_{thr}. Figure 4.2a is to be compared with Figure 3.5a, where the SNR loss is given for the interference-free (noise-only) case. In contrast to the noise-only case in Figure 3.5a, here, the word length has a drastic effect on the SNIR after beamforming.

Figure 4.2a shows furthermore, that each word length n_{bits} has a different optimum clipping threshold, which minimizes the SNIR loss. The optimum clipping thresholds depend on the input power $2\sigma_{\text{I}}^2$, i.e. some form of AGC is needed in order to adapt the clipping threshold of the quantizer to the signal power and achieve the best SNIR.



(a) Strong interference (I_0/N_0 = 68 dB), variable clipping threshold

(b) Variable interference power, optimum clipping threshold

Figure 4.2: SNIR loss due to quantization

Assuming that this adaptation is ideally carried out, the minimum SNR loss for different word lengths is plotted in Figure 4.2b, this time for variable interference power densities I_0. An empirical formula to estimate the maximum tolerable INR $(I_0/N_0)_{\max}$, for which the SNIR loss due to quantization reaches 3 dB, can be derived from Figure 4.2b:

$$(I_0/N_0)_{\max} = 0.15\ \text{dB} + n_{\text{bits}} \cdot 6.02\ \text{dB}.$$

For example, a precision of at least $n_{\text{bits}} = 14$ bits is required before beamforming in order to successfully suppress a single broadband interference with an INR of 85 dB.

4.2.2 Quantization of the filter coefficients

Besides the quantization of the input signal, the quantization of the beamforming vector $\mathbf{w}$ itself has also an effect on the beamforming performance. In this section, this effect is examined for the simple case that only one interference signal $s(t)$ with a power of σ_s^2 is received by the antenna. With $\mathbf{b}$ the steering vector of the interference signal the received signal is in this case

$$\mathbf{x}(t) = \underbrace{\mathbf{b} \cdot s(t)}_{\text{interference}} + \underbrace{\mathbf{n}(t)}_{\text{noise}},$$

where $\mathbf{n}(t)$ is an additive spatially white noise with a power of σ_n^2. The INR of $\mathbf{x}(t)$ is $\text{INR}_{\text{max}} = \sigma_s^2/\sigma_n^2$. Here, the projection matrix defined by (4.6) becomes

$$\mathbf{P}^{\perp} = \mathbf{P}^{\perp}(\mathbf{b}) = \mathbf{1} - \frac{\mathbf{b}\mathbf{b}^{\text{H}}}{|\mathbf{b}|^2} = \mathbf{1} - \frac{\mathbf{b}\mathbf{b}^{\text{H}}}{N_{\text{ant}}}$$

and perfectly eliminates the interference signal:

$$\mathbf{y}^{\perp}(t) = \mathbf{P}^{\perp} \cdot \mathbf{x}(t) = \overbrace{\underbrace{\mathbf{P}^{\perp} \cdot \mathbf{b}}_{=\mathbf{0}} \cdot s(t)}^{\text{interference}} + \overbrace{\mathbf{P}^{\perp} \cdot \mathbf{n}(t)}^{\text{noise}} = \mathbf{P}^{\perp} \cdot \mathbf{n}(t),$$

i.e. $\mathbf{y}^{\perp}(t)$ contains only a spatially colored noise.

However, if we replace $\mathbf{P}^{\perp}$ by its quantized version $\text{q}\{\mathbf{P}^{\perp}\}$, a portion of the interference power

$$\tilde{P}_s = \text{E}\{|\text{q}\{\mathbf{P}^{\perp}\} \cdot \mathbf{b} \cdot s|^2\} = \sigma_s^2 \cdot \text{E}\{|\text{q}\{\mathbf{P}^{\perp}\} \cdot \mathbf{b}|^2\} > 0 \tag{4.11}$$

"escapes" the projection on average, because $\text{q}\{\mathbf{P}^{\perp}\} \cdot \mathbf{b} \neq \mathbf{0}$. $\text{E}\{\cdot\}$ is here the average over all possible signal directions. The noise power after projection can be computed as follows:

$$\tilde{P}_n = \text{E}\{|\text{q}\{\mathbf{P}^{\perp}\} \cdot \mathbf{n}|^2\} = \sigma_n^2 \cdot \sum_{i,j} |\text{q}\{p_{ij}\}|^2, \tag{4.12}$$

where $\text{q}\{p_{ij}\}$ are the elements of the quantized projection matrix $\text{q}\{\mathbf{P}^{\perp}\}$. Finally, the INR after beamforming is

$$\tilde{\text{INR}} = \tilde{P}_s/\tilde{P}_n$$

with $\tilde{P}_s$ and $\tilde{P}_n$ from (4.11) and (4.12).

If $\mathbf{P}^{\perp}$ without quantization is used for projection, $\tilde{\text{INR}} \to -\infty$, as $\tilde{P}_s = 0$. That is, projection yields an infinite reduction in the INR. However, in contrast to $\mathbf{P}^{\perp}$ its quantized version $\text{q}\{\mathbf{P}^{\perp}\}$ does not completely eliminate the interference but achieves a limited reduction in the INR ($\tilde{P}_s > 0$). The average reduction $\Delta\text{INR} = \tilde{\text{INR}}/\text{INR}_{\text{max}} < 1$ was numerically computed and is plotted in Figure 4.3 (dotted lines) for different word lengths and different number of antennas.

The INR can also be analytically computed if the quantization is modeled as

$$\text{q}\{\mathbf{P}^{\perp}\} = \mathbf{P}^{\perp} + \mathbf{N}_q, \tag{4.13}$$

where the quantization noise is modeled as an additive noise matrix $\mathbf{N}_q$. Furthermore, we make the assumption that the elements of $\mathbf{N}_q$ are uncorrelated ($\text{E}\{[\mathbf{N}_q]_{i_1 j_1} \cdot [\mathbf{N}_q]_{i_2 j_2}\} = 0$ if $i_1 \neq i_2$ or $j_1 \neq j_2$), which leads to

$$\text{E}\{\mathbf{N}_q^{\text{H}} \cdot \mathbf{N}_q\} = N_{\text{ant}} \cdot \sigma_q^2 \cdot \mathbf{I}. \tag{4.14}$$

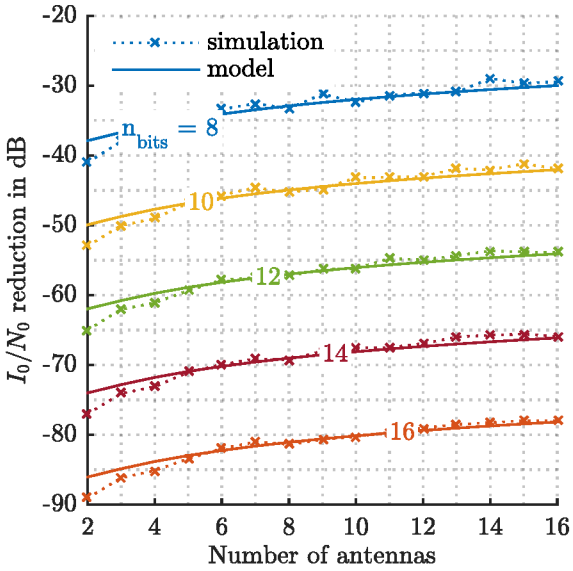


Figure 4.3: INR reduction due to the projection using $\mathrm{q}\{\mathbf{P}^{\perp}\}$

$\sigma_q^2 = \sigma_{q,\mathrm{Re}}^2 + \sigma_{q,\mathrm{Im}}^2$ is the total power of the quantization error in a single element of $\mathrm{q}\{\mathbf{P}^{\perp}\}$. It is the sum of the quantization error powers in the real and imaginary parts.

With (4.13), (4.14) and $\mathbf{P}^{\perp} \cdot \mathbf{b} = \mathbf{0}$, the interference power after projection in (4.11) becomes

$$\begin{aligned}\tilde{P}_s = \sigma_s^2 \cdot \mathrm{E}\{|\mathbf{N}_q \cdot \mathbf{b}|^2\} &= \sigma_s^2 \cdot \mathbf{b}^{\mathrm{H}} \cdot \mathrm{E}\{\mathbf{N}_q^{\mathrm{H}} \cdot \mathbf{N}_q\} \cdot \mathbf{b} \\ &= N_{\mathrm{ant}} \cdot \sigma_s^2 \cdot \sigma_q^2 \cdot \mathbf{b}^{\mathrm{H}} \cdot \mathbf{b} = N_{\mathrm{ant}}^2 \cdot \sigma_s^2 \cdot \sigma_q^2.\end{aligned}$$

The elements of $\mathbf{P}^{\perp}$ are within the range $[-1, 1)$. If they are represented with n_{bits} bits in two's complement,

$$\sigma_{q,\mathrm{Re}}^2 = \sigma_{q,\mathrm{Im}}^2 = \frac{\Delta^2}{3} \qquad \text{with} \quad \Delta = 2^{-n_{\mathrm{bits}}+1}.$$

The noise power $\tilde{P}_n$ in (4.12) can be approximated as

$$\tilde{P}_n \approx \sigma_n^2 \cdot \sum_{i,j} |p_{ij}|^2 = \sigma_n^2 \cdot (N_{\mathrm{ant}} - N_{\mathrm{I}}).$$

The number of interferers is here $N_{\mathrm{I}} = 1$. Finally, the analytical expression

$$\Delta\mathrm{INR} \approx \frac{2}{3} \cdot \frac{N_{\mathrm{ant}}^2}{N_{\mathrm{ant}} - N_{\mathrm{I}}} \cdot 2^{-2\cdot(n_{\mathrm{bits}}-1)} \tag{4.15}$$

can be derived. (4.15) is also plotted in Figure 4.3. It matches with the curves computed numerically by means of simulations. This formula can be used to roughly estimate the required quantization precision for the beamforming vector. For example, in case of a 4-element-antenna, 16 bits (32 bits in total for the real and the imaginary parts) are required, if the beamformer is supposed to suppress broadband noise interference with an INR of 85 dB down to noise level.

4.3 2-Step Spatial Processing

This section presents a 2-step adaptive beamforming approach. It starts with a comprehensive discussion of the different implementation options for a beamformer with regard to the implementation cost. The discussion in Subsection 4.3.1 reveals the advantage of a 2-step approach, that consists of an interference mitigation filter at pre-correlation stage and a multipath mitigation filter at post-correlation stage. Subsequent two subsections explain these two separate steps more in detail.

4.3.1 Cost comparison

Since both correlation and beamforming are linear operations, they can theoretically be done in either order [58]. However, the order makes a significant difference from the implementation point of view. Although an interference-free signal may be quantized with a small number of bits (Section 3.2), a higher precision is required in the presence of strong interference to cope with the potentially high dynamic range of the interference signal (Section 4.2). That means that a high signal resolution is required in the signal processing chain until beamforming takes place and suppresses strong interference signals. After beamforming (interference mitigation), the resolution may be reduced by re-quantizing the beamformer's output. All stages that follow the beamforming operate based on the significantly reduced signal resolution. Hence, the place of beamforming in the processing chain significantly changes the computational complexity of the entire baseband processing.

This subsection discusses the computational cost and the memory requirement in relation with the order of the computational stages in the signal processing chain. The final conclusion will be that a two-step approach is an efficient option that reduces the hardware requirements. These two-steps are the spatial interference mitigation filter at pre-correlation stage and the beamformer at post-correlation stage. While white blocks in the block diagrams hereafter represent computations in dedicated hardware, gray blocks stand for computations in software.

The following options for the order are mainly available:

1. Power minimization (Section 4.1.7) before correlation (Figure 4.4):

   In the processing chain, the input vector $\mathbf{x}$ is multiplied by a weighting vector $\mathbf{w}_{\mathrm{PM}}$ ($\mathbf{y} = \mathbf{w}_{\mathrm{PM}}^{\mathrm{H}} \cdot \mathbf{x}$) in order to mitigate interference right after analogue signal conditioning and digitizing. PM suppresses interference signals prior to correlation

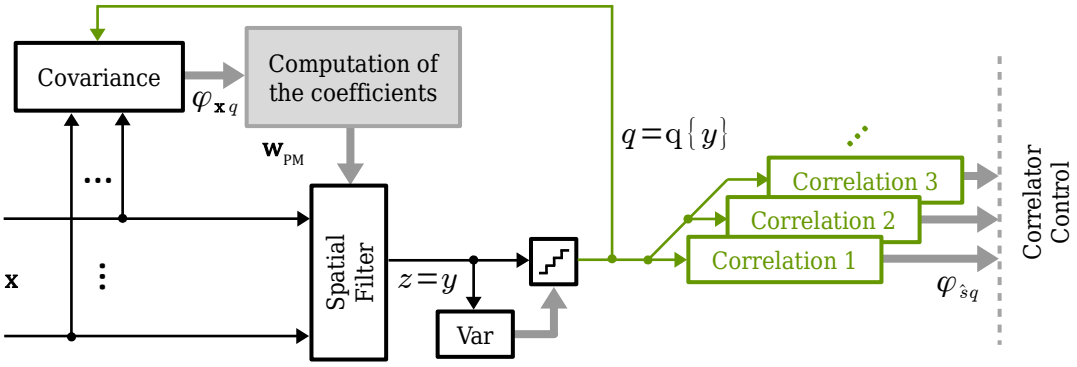


Figure 4.4: Power minimization before correlation

and reduces the signal's dimension from N_{ant} to one. From this point on, the signal is supposed to be interference-free. Hence, the signal's wordlength may be reduced to 2-3 bits immediately after PM at this very early stage (re-quantization). The correlation process, that follows the re-quantization, is computationally the same as in a single-antenna receiver w/o interference protection.

Application of the PM filter is the dot product of two vectors with N_{ant} complex elements. The computational complexity of this operation is

$$\begin{aligned} C_{\mathrm{filt},1} =& N_{\mathrm{ant}} \cdot C_{\mathrm{cmul}}(n_w, n_x) \\ &+ (N_{\mathrm{ant}} - 1) \cdot C_{\mathrm{cadd}}(n_w + n_x + 1 + \lfloor \log_2(\sqrt{N_{\mathrm{ant}}}) \rfloor) \end{aligned}$$

in full-adders. Here, $C_{\mathrm{cmul}}(n_1, n_2)$ is the computational cost of the multiplication of two complex numbers with word lengths n_1 and n_2. n_w is the word length of the weighting vector $\mathbf{w}_{\mathrm{PM}}$ and n_x is the word length of the input signal $\mathbf{x}$. $C_{\mathrm{cadd}}(n)$ is the computational cost of the addition of two complex numbers with a word length of n.

The computation of the filter coefficients $\mathbf{w}_{\mathrm{PM}}$ based on (4.10) requires the computation of the covariance between the input vector $\mathbf{x}$ and the quantized filter output $\mathrm{q}\{y\}$. This computation is composed of N_{ant} complex multiply and accumulate (mac) operations at each clock cycle. Hence, its cost in full-adders is

$$C_{\mathrm{cov},1} = N_{\mathrm{ant}} \cdot C_{\mathrm{cmac}}(n_x, n_q).$$

If complex numbers with word lengths n_1 and n_2 are multiplied and accumulated the computational cost of one mac-operation is

$$C_{\mathrm{cmac}}(n_1, n_2) = C_{\mathrm{cmul}}(n_1, n_2) + C_{\mathrm{cadd}}(n_1 + n_2 + 1 + \Delta n),$$

where $\Delta n = \lfloor \log_2(K) \rfloor$ is the bit growth in case a maximum of K products are summed. A register of size (in bits)

$$M_{\mathrm{cmac}}(n_1, n_2) = 2 \cdot (n_1 + n_2 + 1 + \Delta n)$$

is needed to save the result of a mac-operation. In total, this makes

$$M_{\text{cov},1} = N_{\text{ant}} \cdot M_{\text{cmac}}(n_x, n_q)$$

bits for all filter coefficients.

The variance of the filter output y needs to be computed as well in order to set the clipping thresholds of the re-quantizer properly after spatial filtering. Computation of the variance is the accumulation of the squared absolute values. The cost for this computation is

$$C_{\text{var},1} = C_{\text{var}}(n_y) = C_{\text{csqr}}(n_y) + C_{\text{add}}(2 \cdot n_y + 1 + \Delta n)$$

with n_y the word length of the filter output y, where $C_{\text{csqr}}(n)$ is the cost of squaring and accumulating numbers with a word length of n. The result is stored in a register of size

$$M_{\text{var},1} = M_{\text{var}}(n_y) = 2 \cdot n_y + 1 + \Delta n.$$

The carrier and code wipe-off path of all N_{sat} correlation channels cost

$$C_{\text{corr},1} = N_{\text{sat}} \cdot C_{\text{corr}}(n_q)$$

with

$$C_{\text{corr}}(n_q) = C_{\text{cmul}}(n_c, n_q) + N_{\text{corr}} \cdot C_{\text{cadd}}(n_c + n_q + 1 + \Delta n)$$

being the cost for one channel, where n_c is the word length of the local carrier signal and n_q is the reduced word length of y after re-quantization. N_{corr} complex correlation values are stored in registers, i.e.

$$M_{\text{corr}}(n_q) = N_{\text{corr}} \cdot 2 \cdot (n_c + n_q + 1 + \Delta n)$$

bits per correlation channel. In total, this makes

$$M_{\text{corr},1} = N_{\text{sat}} \cdot M_{\text{corr}}(n_q)$$

for all N_{sat} channels.

2. Beamforming before correlation (Figure 4.5):

   Beamforming is applied to the input signal x before correlation like, e.g. in [44]. In contrast to the PM method, the beamforming vector is different for each satellite channel. Hence, application of the spatial filter costs N_{sat} times the application of the PM filter:

   $$C_{\text{filt},2} = N_{\text{sat}} \cdot C_{\text{filt},1}.$$

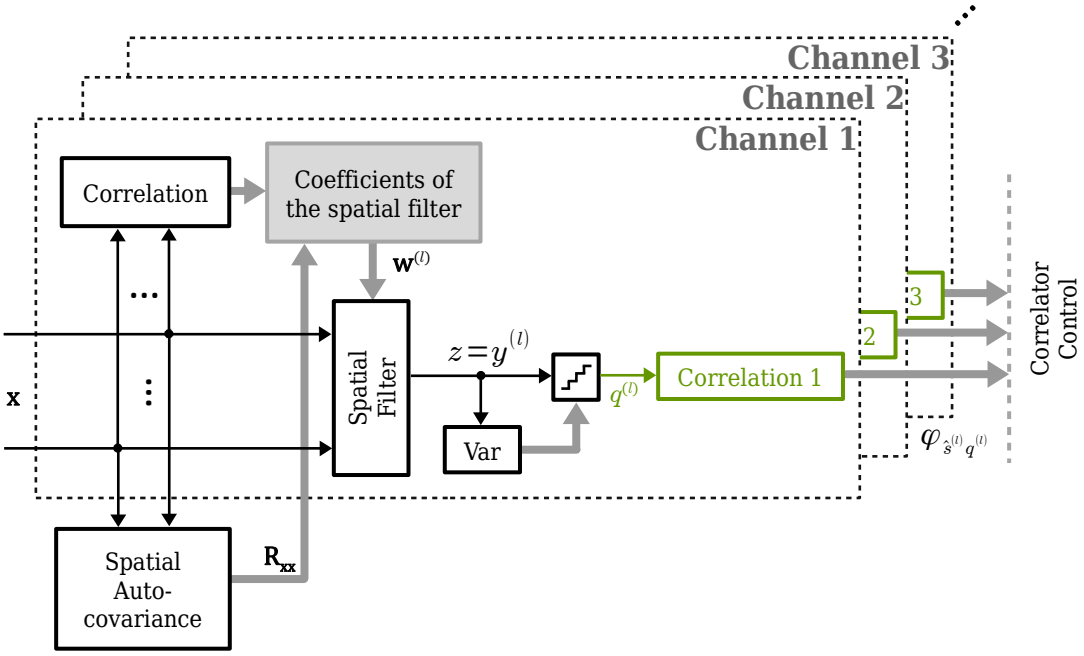


Figure 4.5: Beamforming before correlation

Computation of the filter coeffiecients of the MMSE beamformer as given in (4.4) requires computation of the auto-covariance matrix $\mathbf{R_{xx}}$. Since $\mathbf{R_{xx}}$ is a hermitian matrix, it is sufficient to compute only half of its non-diagonal elements. The computational cost of $\mathbf{R_{xx}}$ is

$$C_{\text{cov},2} = \underbrace{\frac{(N_{\text{ant}} - 1) \cdot N_{\text{ant}}}{2} \cdot C_{\text{cmac}}(n_x, n_x)}_{\text{non-diagonal}} + \underbrace{N_{\text{ant}} \cdot C_{\text{var}}(n_x)}_{\text{diagonal}}$$

and the memory required to store $\mathbf{R_{xx}}$ is

$$M_{\text{cov},2} = N_{\text{ant}}^2 \cdot M_{\text{var}}(n_x).$$

It is taken into account, that the diagonal elements of $\mathbf{R_{xx}}$ are real numbers and the non-diagonal elements are complex numbers.

The variance of the filter output is computed for each satellite channel with the aim of adapting the clipping thresholds of the quantizers. The cost and the storage requirement of the variance computation are

$$C_{\text{var},2} = N_{\text{sat}} \cdot C_{\text{var}}(n_y) \quad \text{and} \quad M_{\text{var},2} = N_{\text{sat}} \cdot M_{\text{var}}(n_y).$$

Estimation of the steering vector requires the computation of the correlation $\varphi^T_{\hat{s}^{(l)}\mathbf{x}}(0)$ between the input signal vector $\mathbf{x}$ and the local signal replica $\hat{s}^{(l)}$ for all N_{sat} satel-

lites as defined in (3.6):

$$C_{\text{ste},2} = N_{\text{sat}} \cdot N_{\text{ant}} \cdot [C_{\text{cmul}}(n_c, n_x) + C_{\text{cadd}}(n_c + n_x + 1 + \Delta n)]$$
$$M_{\text{ste},2} = N_{\text{sat}} \cdot N_{\text{ant}} \cdot 2 \cdot (n_c + n_x + 1 + \Delta n)$$

The computational cost and the storage requirement for correlation are the same as in the case of the PM filter:

$$C_{\text{corr},2} = C_{\text{corr},1} \quad \text{and} \quad M_{\text{corr},2} = M_{\text{corr},1}.$$

3. Beamforming after correlation (Figure 4.6):

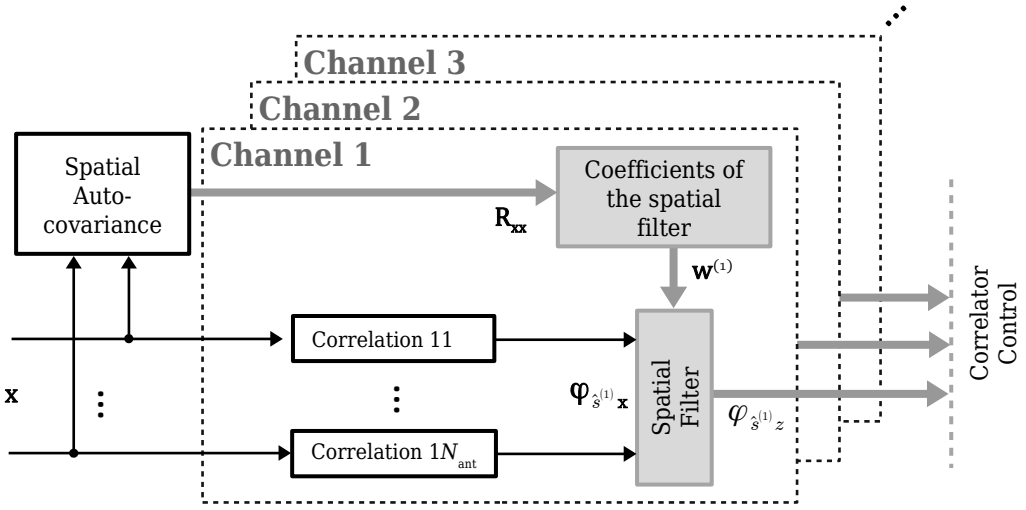


Figure 4.6: Beamforming after correlation

Beamforming is applied after correlating the input signal vector $\mathbf{x}$ with the local satellite signal replicas $\hat{s}$ like in [20]. The filtering is carried out once per correlation period by multiplying the multidimensional correlation output $\varphi^T_{\hat{s}^{(l)}\mathbf{x}}(i \cdot \delta\tau)$ with the beamforming weights $\mathbf{w}^{(l)}$ of the individual satellite channels. Hence, unlike the previous options, implementation of a spatial filter in hardware is not necessary for this option.

Computation of the auto-covariance matrix $\mathbf{R_{xx}}$ is still required in order to estimate the beamforming weights:

$$C_{\text{cov},3} = C_{\text{cov},2}$$
$$M_{\text{cov},3} = M_{\text{cov},2}$$

In contrast to the previous two beamforming variants, here, the input signal of the correlation is the high-resolution vector $\mathbf{x}$ (with a word length of n_x). The cost

and the storage required for computing the correlation values $\varphi^{T}_{\hat{s}^{(l)}\mathbf{x}}(i \cdot \delta\tau)$ are

$$C_{\text{corr},3} = N_{\text{sat}} \cdot N_{\text{ant}} \cdot C_{\text{corr}}(n_x)$$
$$M_{\text{corr},3} = N_{\text{sat}} \cdot N_{\text{ant}} \cdot M_{\text{corr}}(n_x).$$

4. Two-step beamforming:

   [28, 68, 69, 70] propose a two-step processing. A subspace orthogonal projection filter $\mathbf{P}^{\perp}$ is applied to the input signal vector $\mathbf{x}$ to mitigate interference signals before correlation. After interference mitigation, the signal can be re-quantized in order to reduce its word length before computing its correlation with the local signal replica. An adaptive beamforming vector $\mathbf{w}^{(l)}_{\text{post}}$ is applied to the correlation values separately for each satellite to form the beams towards the satellites after correlation. The two-step beamforming is further described in Subsection 4.3.2. Here, the focus is on the implementation cost.

   The computational cost of the interference mitigation filtering before correlations ($\mathbf{y} = \mathbf{P}^{\perp} \cdot \mathbf{x}$) is

   $$C_{\text{filt},4} = N_{\text{ant}} \cdot C_{\text{filt},1}.$$

   $\mathbf{P}^{\perp}$ is derived from the auto-covariance matrix $\mathbf{R}_{\mathbf{xx}}$. Computation of $\mathbf{R}_{\mathbf{xx}}$ using digital hardware requires

   $$C_{\text{cov},4} = C_{\text{cov},2} = C_{\text{cov},3}$$

   full-adders and

   $$M_{\text{cov},4} = M_{\text{cov},2} = M_{\text{cov},3}.$$

   bits of memory. The cost for computing the variance of $\mathbf{y}$ at the filter output is

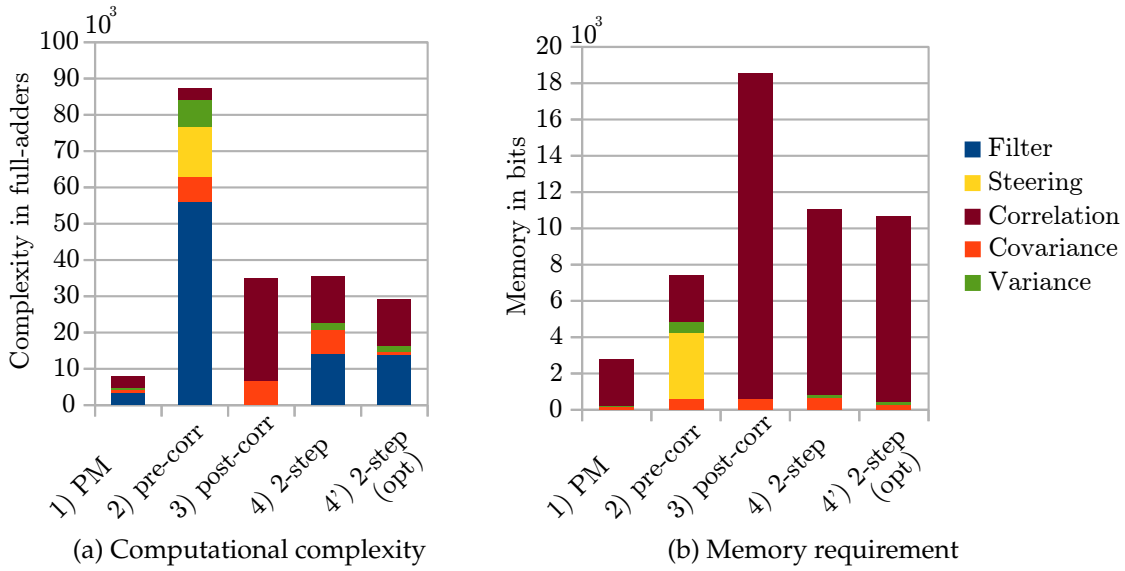
   $$C_{\text{var},4} = N_{\text{ant}} \cdot C_{\text{var}}(n_y)$$
   $$M_{\text{var},4} = N_{\text{ant}} \cdot M_{\text{var}}(n_y).$$

   Finally, correlating the coarse-resolution multi-dimensional signal $\mathrm{q}\{\mathbf{y}\}$ with the local replica signal $\hat{s}^{(l)}$ costs

   $$C_{\text{corr},4} = N_{\text{ant}} \cdot C_{\text{corr},1}$$
   $$M_{\text{corr},4} = N_{\text{ant}} \cdot M_{\text{corr},1}.$$

Figure 4.7 shows the computational cost and the memory requirement of the different approaches under the following conditions:

- the input/output word length of the spatial filter $n_x = n_y = 14$ as in [20, 70]
- the output word length of the re-quantizer $n_q = 2$
- the word length of the local carrier signal $n_c = 2$
- the sampling frequency f_s = 2 MHz and the integration time T = 1 ms, which means an accumulation over $K = 2 \cdot 10^3$ samples
- the number of antennas $N_{\text{ant}} = 4$, the number of correlation channels $N_{\text{sat}} = 16$
- and the number of discrete code delays, for which the correlation values are computed, $N_{\text{corr}} = 5$ (as required by the $\Delta\Delta$-discriminator used for code tracking).



(a) Computational complexity (b) Memory requirement

Figure 4.7: Computational complexity and memory requirement of the different beamforming options

As expected, the PM approach (1) is the most cost-efficient method among all. It is the most simplistic approach at the same time. It suppresses interference signals but does not explicitly form a beam towards the satellite's direction. It does not provide any protection against multipath either.

Compared to the beamforming at post-correlation stage (3) and the two-step approach (4), beamforming at pre-correlation stage (2) is the most computationally expensive method. The computational complexity of this approach is 2.5× the computational cost of the former two. The application of the spatial filter to the high resolution input signal x dominates the computational cost. The correlation constitutes a small

portion of the total cost. The memory requirement is the smallest after the PM approach (1).

Post-correlation beamforming (3) eliminates the implementation of the spatial filter in hardware. This comes at expense of an increased computational complexity and an increased memory requirement of the correlation process. However, the overall computational cost of post-correlation beamforming is significantly lower compared to the pre-correlation beamforming (2). The overall memory requirement is significantly higher due to the memory requirement of the correlation in particular.

The two-step processing (4) has a balanced distribution of the computational cost between the spatial filter and the correlation. In total, its computational complexity is nearly equal to the computational complexity of the post-correlation beamforming. The memory requirement of the two-step approach is also 40% lower than the memory requirement of the post-correlation beamforming (3). Furthermore, in the following section an optimized version of the two-step approach (4') is presented, that reduces its computational cost by 18%.

4.3.2 Pre-correlation Interference Mitigation

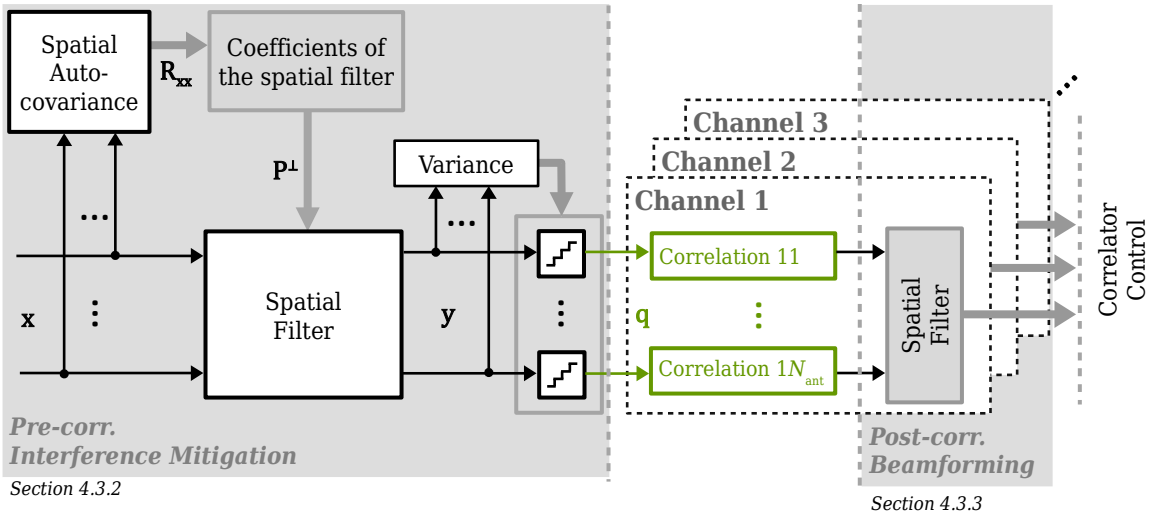


Figure 4.8: Non-recursive interference mitigation at pre-correlation stage

The block diagram of the interference mitigation filter at pre-correlation from [70] is given in Figure 4.8. The input vector $\mathbf{x} \in \mathbb{C}^{N_{\text{ant}} \times 1}$ contains the down-converted and digitized complex outputs of the antenna-array elements with N_{ant} being the number of the array elements. For interference suppression, the input vector $\mathbf{x}$ is multiplied by the projector filter $\mathbf{P}^{\perp} \in \mathbb{C}^{N_{\text{ant}} \times N_{\text{ant}}}$. This is a projection of the input samples onto an

interference-free subspace as defined by (4.6). The projection matrix is derived from the spatial auto-covariance matrix $\mathbf{R_{xx}}$ of the input samples by EVD.

The raw signal $\mathbf{x}$ is quantized with a high precision (14 bits) in order to cover the high dynamic range between weak satellite signals and potentially very strong interference signals. However, the interference-free signal vector $\mathbf{y} = \mathbf{P}^{\perp} \cdot \mathbf{x}$ after projection can be quantized with a coarse precision without practically losing accuracy in the code delay estimation and correspondingly in the user position (see Section 3.2).

This re-quantization step significantly reduces the word length of $\mathbf{y}$ and, hence, the hardware complexity of computing the correlation values $\boldsymbol{\varphi}^{T}_{\hat{s}^{(l)}\mathbf{q}}(t; \delta\tau)$ between $\mathbf{y}$ and the local replicas $\hat{s}^{(l)}$ as defined by (3.6).

Re-quantization of $\mathbf{y}$ can be modeled as

$$\mathbf{q} = \mathrm{q}\{\mathbf{y}\} = \alpha \cdot \mathbf{V}^{-1/2}(\mathbf{y}) \cdot \underbrace{\mathbf{P}^{\perp} \cdot \mathbf{x}}_{=\mathbf{y}} + \sigma_{\mathrm{q}} \cdot \mathbf{n}_{\mathrm{q}}, \text{ with } \mathbf{V}(\mathbf{y}) = \begin{bmatrix} \sigma^2_{y_1} & & \mathbf{0} \\ & \ddots & \\ \mathbf{0} & & \sigma^2_{y_{N_{\mathrm{ant}}}} \end{bmatrix}, \quad (4.16)$$

where $\sigma_{y_1}, \ldots, \sigma_{y_{N_{\mathrm{ant}}}}$ are variances of the elements of $\mathbf{y}$, and $\mathbf{n}_q$ with the auto-covariance $\mathrm{E}\{\mathbf{n}_q \cdot \mathbf{n}_q^{\mathrm{H}}\} = \mathbf{I}$ is an additive Gaussian random vector modeling the quantization error.

While projection suppresses strong interference signals at pre-correlation, the 2nd step of the spatial processing takes place at post-correlation stage separately for each satellite in order to steer a beam towards the satellites.

If multipath is ignored at the first place, the MMSE from Section 4.1.5 is the perfect beamformer with the desired feature of being blind, i.e. it does not require any knowledge about the antenna geometry or the signal directions. Multipath is adressed later in Section 4.3.3. The aim at this point is to find post-correlation beamforming weights, that realize the MMSE if combined with the first step of the spatial processing at pre-correlation stage.

In case the outputs of the array-antenna have nearly equal signal amplifications and noise figures, $\sigma_{y_1} \approx \cdots \approx \sigma_{y_{N_{\mathrm{ant}}}} = \sigma_y$ and hence $\mathbf{V}(\mathbf{y}) \approx \sigma_y^2 \cdot \mathbf{I}$. Further with (4.16), $\mathbf{P}^{\perp} \cdot \mathbf{P}^{\perp} = \mathbf{P}^{\perp}$ and with the approximation in (4.6), the beamforming weights of the

MMSE in (4.4) become

$$\begin{aligned}\mathbf{w}_{\text{MMSE}} \approx & \frac{1}{\sigma_n^2}\cdot\mathbf{P}^{\perp}\cdot\mathrm{E}\{\hat{s}^*\cdot\mathbf{x}\} = \frac{1}{\sigma_n^2}\cdot\mathbf{P}^{\perp}\cdot\mathrm{E}\left\{\hat{s}^*\cdot\underbrace{\mathbf{P}^{\perp}\cdot\mathbf{x}}_{=y}\right\}\\ \approx & \frac{1}{\sigma_n^2}\mathbf{P}^{\perp}\cdot\mathrm{E}\left\{\hat{s}^*\cdot\frac{1}{\alpha}\mathbf{V}^{1/2}\cdot\mathbf{q}\right\}\\ = & \underbrace{\frac{1}{\alpha}\frac{\sigma_y}{\sigma_n^2}}_{=\tilde{\alpha}}\cdot\mathbf{P}^{\perp}\cdot\underbrace{\mathrm{E}\{\hat{s}^*\cdot\mathbf{q}\}}_{\approx\varphi_{\hat{s}\mathbf{q}}(\delta\tau=0)}\end{aligned}$$

Multiplication of the input signal $\mathbf{x}$ with $\mathbf{P}^{\perp}$ is realized by the interference mitigation filter at pre-correlation stage as the first step of the spatial processing. The 2nd step of spatial filtering

$$\frac{1}{\tilde{\alpha}}\varphi_{\hat{s}\mathbf{z}}(\delta\tau) = \mathbf{w}_{\text{post}}^H\cdot\varphi_{\hat{s}\mathbf{q}}(\delta\tau)\quad\text{with }\mathbf{w}_{\text{post}} = \varphi_{\hat{s}\mathbf{q}}(0). \tag{4.17}$$

is applied at post-correlation stage in software.

Jacobi-Algorithm

In [70], the cyclic Jacobi-Algorithm [74] is used for the EVD of the spatial covariance matrix. This algorithm transforms an initially Hermitian matrix $\mathbf{\Lambda}_0 = \mathbf{R}_{\mathbf{xx}}$ to a diagonal matrix $\mathbf{\Lambda}$ containing the eigenvalues. For this purpose, the non-diagonal elements $[\mathbf{R}_{\mathbf{xx}}]_{ij}$ $(i \neq j)$ of the covariance matrix are annihilated one by one using Givens-rotations. Applying the same Givens-rotations concurrently to an initially identity matrix $\mathbf{U}_0 = \mathbf{I}$ produces the eigenvector matrix $\mathbf{U}$. A complete cycle through all non-diagonal elements is called a *sweep*. Because elements being zeroed are filled in again during the zeroing of another element, multiple sweeps are required for a complete diagonalization of $\mathbf{R}_{\mathbf{xx}}$. The fixed-point implementation of the Jacobi-algorithm in [70], which is used for the real-time operation of the receiver, requires 6 complete sweeps per EVD.

Here, a threshold method is applied instead of a cyclic processing of all non-diagonal elements in a sweep, in order to prevent unnecessary Givens-rotations and to determine the minimum necessary number of Givens-rotations per EVD. Accordingly, the Givens-rotation related to a non-diagonal element $[\mathbf{R}_{\mathbf{xx}}]_{ij}$ is carried out unless

$$\beta\cdot[\mathbf{R}_{\mathbf{xx}}]_{ii}\cdot[\mathbf{R}_{\mathbf{xx}}]_{jj} > \left|[\mathbf{R}_{\mathbf{xx}}]_{ij}\right|^2,$$

i.e. unless this element is small enough compared to the corresponding diagonal elements. β is set to 2^{-8} based on simulations, so that no Givens-rotations are carried out for the interference-free case and the precision in the presence of interference is not degraded compared to the cyclic Jacobi-algorithm.

Conversion to a loop

The interference mitigation filter given in Figure 4.8 is non-recursive. It makes no use of the previously computed eigenvectors and eigenvalues. The initialization of the Jacobi-algorithm with the identity matrix $\mathbf{I}$ is a clear indicator for that. It starts from the scratch to decompose the covariance matrix $\mathbf{R_{xx}}$ into its eigenvalues and eigenvectors, every time a new projection matrix $\mathbf{P}^{\perp}$ is computed.

The intention in [71] was first to reduce the computational complexity of the Jacobi-algorithm by introducing a feedback mechanism into the interference mitigation filter in Figure 4.8. The simplest feedback would be to initialize the Jacobi-algorithm with the previously computed eigenvalues

$$\mathbf{U}_0 = \mathbf{U}_{k-1}$$

and with a modified version of the covariance matrix

$$\mathbf{\Lambda}_0 = \mathbf{R}_{\tilde{\mathbf{y}}\tilde{\mathbf{y}}} = \mathbf{U}^{\mathrm{H}} \cdot \mathbf{R_{xx}} \cdot \mathbf{U} \tag{4.18}$$

instead of the "raw" covariance matrix $\mathbf{R_{xx}}$. If $\mathbf{R_{xx}}$ slowly changes over time, $\mathbf{R}_{\tilde{\mathbf{y}}\tilde{\mathbf{y}}}$ is already nearly diagonal and a significantly low number of Givens-rotations are required to diagonalize it. However, the computation of $\mathbf{R}_{\tilde{\mathbf{y}}\tilde{\mathbf{y}}}$ from $\mathbf{R_{xx}}$ requires two additional complex matrix-multiplications.

A better alternative of feed-back would be using the projected signals $\mathbf{y} = \mathbf{P}^{\perp} \cdot \mathbf{x}$ themselves for adaptively "correcting" the eigenvalues and the eigenvectors. The advantage of such an approach is that the projected signals are quantized with a significantly reduced number of bits compared to the high precision quantization before projection. However, the problem with the proposed projector in (4.6) is that it eliminates entire subspaces by a threshold decision. Hence, the projected signals do not provide any information about the interference-subspaces.

From (4.18) it can be derived that instead of $\mathbf{y}$,

$$\tilde{\mathbf{y}} = \mathbf{U}^{\mathrm{H}} \cdot \mathbf{x}$$

is required in order to compute the initialization matrix $\mathbf{R}_{\tilde{\mathbf{y}}\tilde{\mathbf{y}}}$ for the Jacobi-algorithm. $\tilde{\mathbf{y}}$ is given as an intermediate result of projection if the projection matrix in (4.6) is broken down into multiple steps:

$$\mathbf{y} = \mathbf{P}^{\perp} \cdot \mathbf{x} = \mathbf{U} \cdot \mathbf{S} \cdot \underbrace{\mathbf{U}^{\mathrm{H}} \cdot \mathbf{x}}_{=\tilde{\mathbf{y}}}. \tag{4.19}$$

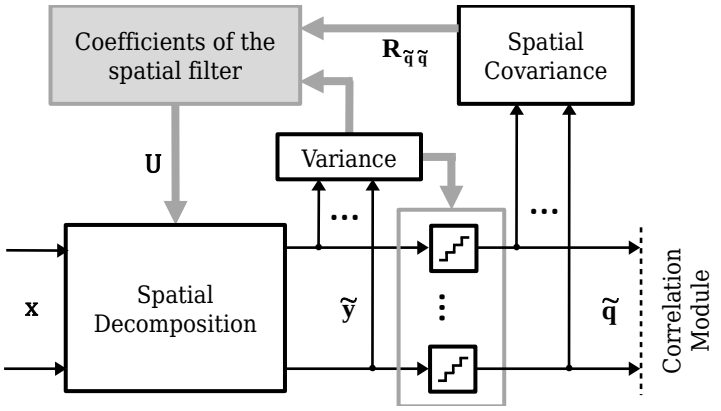


Figure 4.9: Recursive interference mitigation at pre-correlation stage [71]

Let accordingly the computation of $\tilde{\mathbf{y}}$ be the first step of the interference mitigation filter as illustrated in Figure 4.9. $\tilde{\mathbf{y}}$ is the decomposition of the input signal $\mathbf{x}$ into its orthogonal one-dimensional subspaces. If N_I uncorrelated interference signals with distinct directions are received, N_I of these orthogonal subspaces include interference signals (The interference subspaces cannot be assigned to individual interference sources.). The remaining subspaces are interference-free. Thus, the word length of these subspaces can be reduced to 2-3 bits without practically causing an SNR loss. At this point, the effect of re-quantization on the interference subspaces can be ignored, as these subspaces are eliminated by the "selection matrix" $\mathbf{S}$ later.

After orthogonal decomposition by the eigenvector matrix $\mathbf{U}$, the resulting signal $\tilde{\mathbf{y}}$ is re-quantized:

$$\tilde{\mathbf{q}} = \mathrm{q}\{\tilde{\mathbf{y}}\} = \alpha \cdot \mathbf{V}^{-1/2}(\tilde{\mathbf{y}}) \cdot \tilde{\mathbf{y}} + \sigma_q \cdot \mathbf{n}_q.$$

Here, the computation of the variances of the elements of $\tilde{\mathbf{y}}$ is necessary to determine the thresholds of the quantizers.

Instead of computing the auto-covariance matrix $\mathbf{R}_{\tilde{\mathbf{y}}\tilde{\mathbf{y}}}$ based on the high-resolution signal $\tilde{\mathbf{y}}$, its approximation

$$\begin{aligned}\mathbf{R}_{\tilde{\mathbf{y}}\tilde{\mathbf{y}}} &\approx \mathrm{E}\big\{(\alpha \cdot \mathbf{V}^{1/2}(\tilde{\mathbf{y}}) \cdot \tilde{\mathbf{q}}) \cdot (\alpha \cdot \mathbf{V}^{1/2}(\tilde{\mathbf{y}}) \cdot \tilde{\mathbf{q}})^{\mathrm{H}}\big\} \\ &= \alpha^2 \cdot \mathbf{V}^{1/2}(\tilde{\mathbf{y}}) \cdot \mathrm{E}\big\{\tilde{\mathbf{q}} \cdot \tilde{\mathbf{q}}^{\mathrm{H}}\big\} \cdot \alpha^2 \cdot \mathbf{V}^{1/2}(\tilde{\mathbf{y}}) \\ &= \alpha^2 \cdot \mathbf{V}^{1/2}(\tilde{\mathbf{y}}) \cdot \mathbf{R}_{\tilde{\mathbf{q}}\tilde{\mathbf{q}}} \cdot \mathbf{V}^{1/2}(\tilde{\mathbf{y}})\end{aligned}$$

can be computed based on the low-resolution signal $\tilde{\mathbf{q}}$. Due to the reduced word length of $\tilde{\mathbf{q}}$, computation of $\mathbf{R}_{\tilde{\mathbf{q}}\tilde{\mathbf{q}}}$ is significantly less complex than computation of $\mathbf{R}_{\tilde{\mathbf{y}}\tilde{\mathbf{y}}}$. The remaining steps of (4.19), i.e. multiplication with $\mathbf{U} \cdot \mathbf{S}$ (*composition*), can be implemented either in digital hardware before correlation or in software after correlation (with a

drastically reduced computation rate and cost). The order can be chosen arbitrarily, since correlation and matrix-multiplication are both linear operations.

The projection matrix $\mathbf{P}^{\perp}$ replaced $\mathbf{R}_{\mathbf{xx}}^{-1}$ in the MMSE beamformer under the assumption that the interference signal is significantly stronger than the noise and the satellite signals. In [71], it is shown by means of simulations that the projection filter at pre-correlation stage is a suboptimal solution, if this assumption does not hold. In the presence of weak (but still detectable) interference, the signal attenuation of the projection filter in the direction of the interference signal is unnecessarily strong. Furthermore, in case of a small number of array-antenna elements, the signal cancellation cannot be focused in a narrow direction. The projection filter strongly affects satellite signals coming from close directions while canceling even a weak interference signal. Replacing $\mathbf{S}$ by the unit matrix $\mathbf{I}$, i.e. $\mathbf{P}^{\perp}$ by

$$\mathbf{P} = \mathbf{U} \cdot \underbrace{\mathbf{V}^{-1/2}(\tilde{\mathbf{y}}) \cdot \mathbf{U}^{\mathrm{H}}}_{=\tilde{\mathbf{P}}} = \mathbf{R}_{\mathbf{xx}}^{-1/2}$$

significantly corrects this behavior of the interference mitigation filter. Instead of removing entire subspaces, $\mathbf{P}$ suppresses the power of the interference subspace down to noise level. In case of weak interference, the attenuation of $\mathbf{P}$ towards the interference direction is correspondingly weak.

Remark: $\mathbf{P} = \mathbf{R}_{\mathbf{xx}}^{-1/2}$ and $\tilde{\mathbf{P}}$ are both whitening matrices [75]. $\mathbf{P}$ is the *Mahalanobis whitening* (or the *"zero-phase component analysis" whitening*) and $\tilde{\mathbf{P}}$ is a whitening transformation based on scaled principle component analysis [76]. With other words, the interference mitigation filter at pre-correlation stage is a pre-whitening step before quantizing the input signal $\mathbf{x}$.

Neglecting the quantization noise, we can show that the entire chain of decomposing $\mathbf{x}$ by $\mathbf{U}^{\mathrm{H}}$, then re-quantizing and finally beamforming by $\mathbf{w}_{\mathrm{post}} = \mathrm{E}\{\hat{s} \cdot \tilde{\mathbf{q}}\}$ at post-correlation stage is equal to the MMSE beamformer:

$$\begin{aligned}
z &= \mathbf{w}_{\mathrm{post}}^{\mathrm{H}} \cdot \tilde{\mathbf{q}} \\
&= <\hat{s}^* \cdot \tilde{\mathbf{q}}>^{\mathrm{H}} \cdot \tilde{\mathbf{q}} \\
&= <\hat{s} \cdot \mathbf{x}^{\mathrm{H}} \cdot \mathbf{U} \cdot \mathbf{V}^{-1/2}(\tilde{\mathbf{y}})> \cdot \mathbf{V}^{-1/2}(\tilde{\mathbf{y}}) \cdot \mathbf{U}^{\mathrm{H}} \cdot \mathbf{x} \\
&= <\hat{s} \cdot \mathbf{x}^{\mathrm{H}}> \underbrace{\mathbf{U} \cdot \mathbf{V}^{-1}(\tilde{\mathbf{y}}) \cdot \mathbf{U}^{\mathrm{H}}}_{\mathbf{R}_{\mathbf{xx}}^{-1}} \cdot \mathbf{x} \\
&= \mathbf{w}_{\mathrm{MMSE}}^{\mathrm{H}} \cdot \mathbf{x} \quad \text{(Q.E.D.)}
\end{aligned}$$

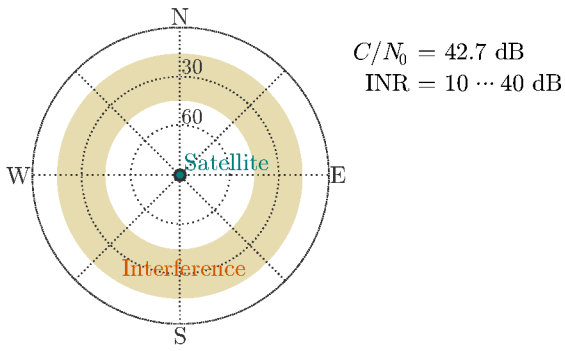


Figure 4.10: Experimental constellation

Simulation Results

A simulation environment was developed using MATLAB in order to evaluate the different signal processing algorithms. The multi-antenna signal generator is able to generate front-end samples based on given artificial satellite constellations as well as all kinds of interference as introduced in Chapter 2. Furthermore, it can simulate the signal reception of a moving antenna conform to real satellite constellations, if these are provided in form of RINEX-files. A software receiver, that implements the entire digital processing chain of a GNSS-receiver from beamforming to PVT, was programmed in MATLAB. The software receiver can be fed by the simulated signals from the signal generator as well as by recorded real front-end samples.

In Figure 4.10, the constellation for the following simulations is given. The satellite ($C/N_0 = 42.7$ dB/Hz) is at zenith, while the interference signals (INR 10 dB and 40 dB) have an elevation between $15°$ and $45°$. All following figures show the average of several hundred separate simulations, in which the INR and the interference direction were selected randomly. The simulations provide a comparison between the non-recursive pre-whitening filter and the recursive filter with and without limiting the number of allowed sweeps of the Jacobi-algorithm. A limitation of the sweeps would be necessary, for example, if the navigation processor provides only a limited computing power.

Figure 4.11 shows the response of the array-antenna receiver to suddenly appearing and disappearing interferences. Starting with the interference-free state, an additional interferer appears each 50 ms. After 150 ms with three interferers, the maximum number of interferences is reached, that can be mitigated using four antennas. From this time, on each 50 ms an interferer disappears. At time 300 ms, the reception is interference-free again. The upper plot in Figure 4.11 shows the change of the SNIR (observed after correlation) in time. The bottom plot shows the number of Givens-rotations required by the Jacobi-Algorithm for the EVD.

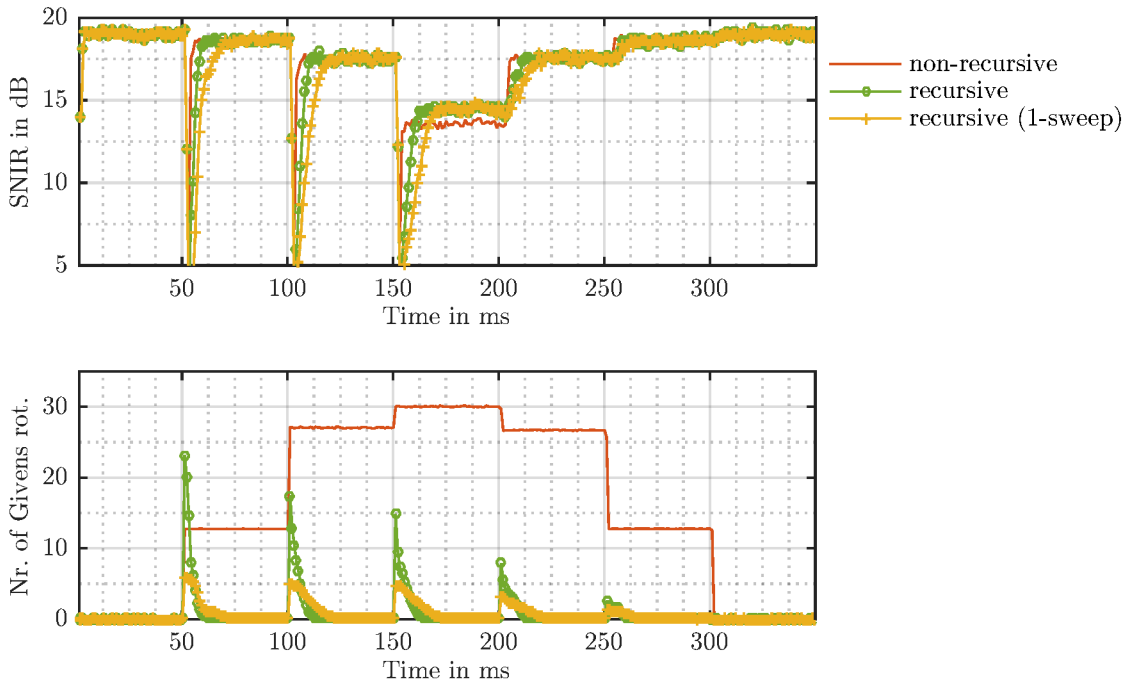


Figure 4.11: Post-correlation SNIR and number of Givens-rotations in case of appearing/disappearing interference sources

The pre-correlation spatial filter does not know about the interference during the first correlation period after the appearance of an interferer. The filter lets the interference through and, as a result, the SNIR drops abruptly. At the end of this period, the interference is detectable in the covariance matrix $\mathbf{R}_{\mathbf{xx}}$, and the spatial filter starts to adapt its coefficients to the new environment. The non-recursive filter responds immediately within one integration period (1 ms). The recursive method requires a settling time of ca. five integration periods (5 ms) after each appearance/disappearance of an interferer. If the number of sweeps is limited to one (six Givens-rotations) the settling time increases to ca. fifteen integration periods (15 ms). In steady state, the SNIRs are equal for all three variants except for the case of three interferers. In this case, the recursive methods perform slightly better.

The benefit of the recursive method with regard to the computational cost becomes clear in the number of the Givens-rotations in Figure 4.11 (buttom). The non-recursive implementation requires at least 12 Givens-rotations for the EVD of the auto-covariance matrix $\mathbf{R}_{\mathbf{xx}}$ for each coefficient update. In case of three interferers, this number of the required Givens-rotations reaches up to 30. In comparison, the recursive methods require a high number of Givens-rotations only in the first few integration periods after an appearance/disappearance of an interferer. The number declines with time. The eigenvalues and eigenvectors are recursively adapted to the changed environment

over time. After ca. 15 ms (25 ms in case the number of the sweeps is limited to one) the computation of the EVD is finalized. As long as the interference conditions remain unchanged, adjustment of the eigenvectors is no longer required. That means that the recursive method causes peak processing loads after heavy changes in the interference environment, but the overall processing load is significantly lower compared to the non-recursive computation. If the processor does not provide enough computing power for the peaks, it is allowed to limit the number of Givens-rotations in order to spread the computations over time at the expense of a longer reaction time.

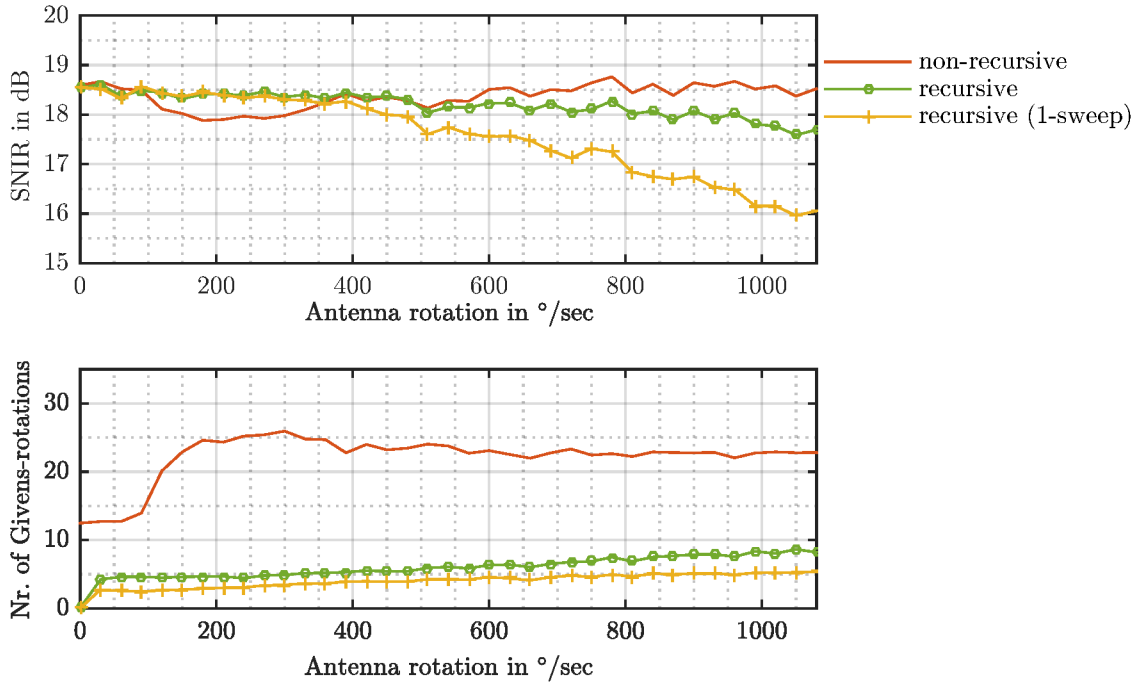


Figure 4.12: Post-correlation SNIR and number of Givens-rotations in case of a rotating antenna and a single strong interference

Figure 4.12 shows the interference mitigation performance in case of an antenna rotation, i.e. the interferer's direction constantly changes over time. In a stationary scenario (antenna rotation = 0), all filter variants perform equally and yield an SNIR of 17 dB. While the non-recursive method uses 12 Givens-rotations in every integration period for the EVD of $\mathbf{R}_{xx}$, the recursive methods keep the previously computed eigenvectors without making any changes.

In case of the non-recursive filter, the SNIR is nearly unaffected by the antenna rotation for the examined rotational speeds. If the recursive filter structure is used, the SNIR decreases slightly with increasing rotational speeds because of the slow reaction of the filter to the changes in the interference environment. The drop in the SNIR is more significant if the computations per coefficient update is limited to one sweep.

The advantage of the recursive method is once again the reduced number of Givens-rotations compared to the non-recursive filter. The non-recursive method computes ca. 23 Givens-rotations per EVD if the antenna rotation is greater than $200°/s$. Although the recursive filter variants require an increased number of Givens-rotations for higher receiver dynamics, overall, this number remains significantly lower than 23. The limitation of the computational load per EVD is allowed at the expense of the dynamic performance of the filter.

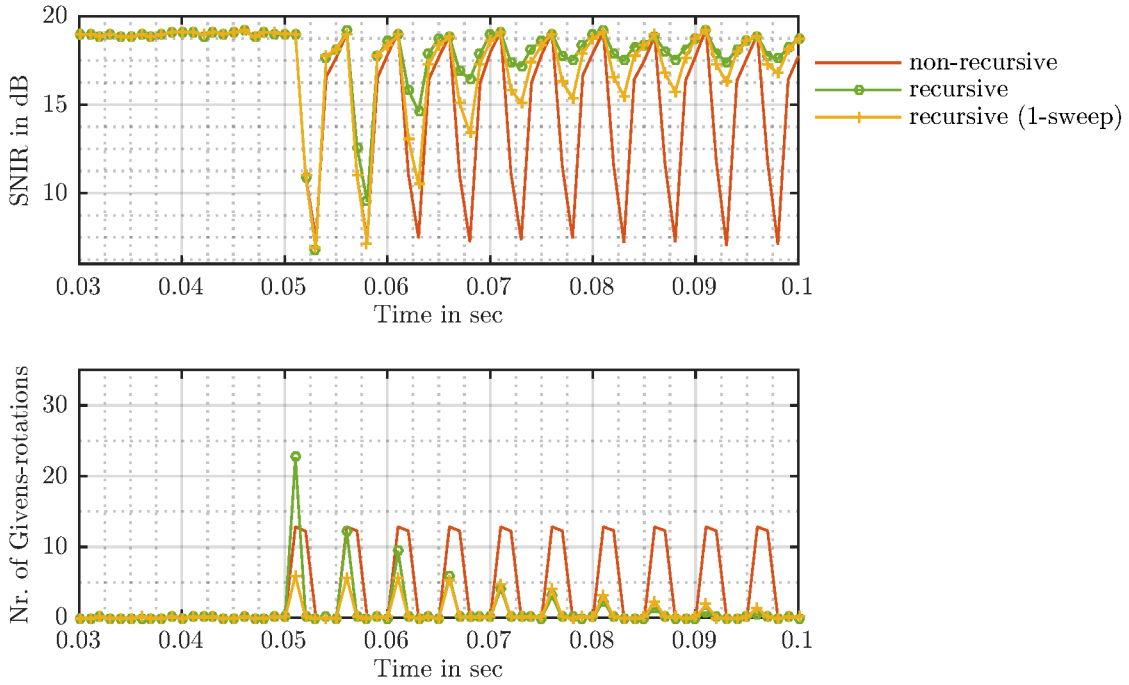


Figure 4.13: Post-correlation SNIR and number of Givens-rotations in the presence of a single pulsed interference

Figure 4.13 shows finally the performance of the different filters in the presence of a pulsed interference. The interference signal is turned on at time 50 ms. Its pulse duration is 1 ms and the pulse frequency is 20 Hz. The pulses have an INR of 50 dB. If not suppressed at all, this kind of pulsed interference would not completely make the receiver unable to track the satellite signals. It would, however, degrade the signal reception during one fifth of the entire time.

The receiver can adapt to a change in the interference environment, here to the direction of the pulse signal, only after finishing the integration period, in which the change occurs. Before then, the receiver is unaware of the pulse and the pre-correlation filter lets the interference pass through. It behaves similarly immediately after a pulse. This time, the filter still "thinks" that there is an interference and suppresses signals coming from the pulse's direction unnecessarily. In Figure 4.13, exactly this behavior

of the non-recursive filter can be observed every time a pulse appears and disappears.

The recursive method shows here a clear advantage over the non-recursive method. While it behaves similar to the non-recursive filter for the first few pulses, it gets less and less affected by the following pulses. The reason for that is the step-by-step adaptation of the recursive filter to the interference direction with each pulse. For the eigenvectors, this means that they slowly converge to their final values determined by the constant interference direction. The appearance and disappearance of the pulses effect only a change of the corresponding eigenvalue, but the decomposition matrix $\mathbf{U}$ remains unchanged, as no (or just very few) Givens-rotations are executed after convergence. Once convergence takes place, the decomposition step of the recursive filter successfully isolates the interference subspace from the noise subspace. This separation is maintained independent from the presence of a pulse.

Multi-dimensional Power Minimization

The power minimization filter with a single output from Section 4.1.7 can be extended to a filter with a multidimensional output, which is called the *multi-dimensional power minimization* (MPM) filter in this thesis. As an alternative to the EVD-based filters, this MPM filter can be employed as the first step in a two-step filter structure to mitigate interference signals before correlation. While the PM filter is well-known, its extension to MPM is first proposed in this thesis.

The MPM filter combines N_{ant} single-output PM filters. Each PM filter takes a different array element's output as its reference. That means that for example the first PM filter interprets the first element's output as the desired "reference" signal ($i_{\text{ref}} = 1$). The filter attempts to form a copy of the reference signal combining all other antenna outputs. The copy signal is then subtracted from the reference signal to minimize the power at the filter output. The second PM filter takes the second element's output as its reference and so on.

With regard to the computation of the filter coefficients in software, the MPM is a cost-efficient method compared to the EVD-based recursive and non-recursive methods. The filter coefficients of the MPM can be computed by means of the LMS based algorithm in (4.8), which is composed of only N_{ant}^2 complex additions. In hardware, the MPM requires cross-covariance $\mathbf{R_{xy}}$ between the input vector $\mathbf{x}$ and the output vector $\mathbf{y}$, whose elements $y_1, \ldots, y_{N_{\text{ant}}}$ are defined by (4.7). $\mathbf{R_{xq}} = \mathbf{R_{xq\{y\}}}$, i.e. the cross-covariance between the input $\mathbf{x}$ and the quantized output $\mathrm{q}\{\mathbf{y}\}$ in order to reduce the computational cost. As the computation of $\mathbf{R_{xq}}$ is more costly relative to $\mathbf{R_{\tilde{q}\tilde{q}}}$ (which is required by the recursive EVD-based filter), the hardware requirement of

MPM is (only) slightly higher than the recursive EVD-based filter. The MPM filter can be preferred an alternative to the recursive filter to release some software processing resources at the expense of additional digital hardware.

In Figure 4.14, the SNIR at the post-correlation stage is shown for the case of appearing and disappearing interferers. The SNIR is plotted for different coefficient update rates (1 kHz-256 kHz). For update rates less than 64 kHz, the filter does not respond

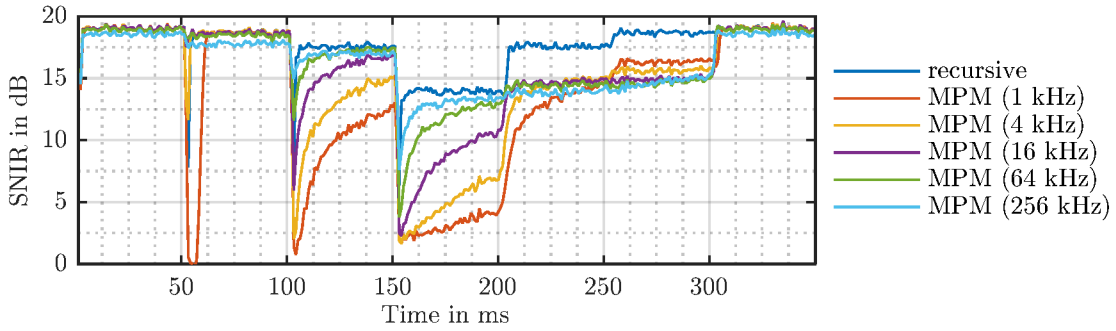


Figure 4.14: Post-correlation SNIR in case of appearing/disappearing interference sources

fast enough to sudden changes in the interference conditions. Furthermore, when interferers start to disappear in the second half of the plot, a lower SNIR is observed in comparison to the EVD-based recursive method. The MPM filter does not recover completely from the heavy interference conditions even in long term and converges to a sub-optimum solution.

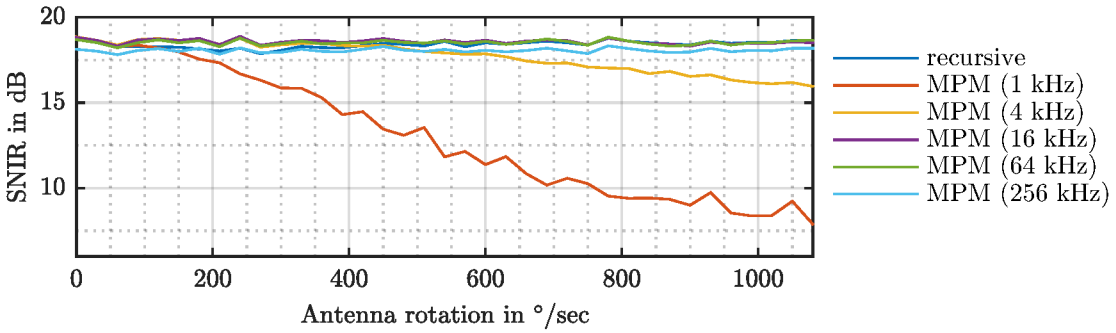


Figure 4.15: Post-correlation SNIR in case of a rotating antenna and single strong interference

In Figure 4.15 the SNIR is plotted for the case of a rotating antenna and a single strong interference. Different coefficient update rates are considered. Filter update rates 1 kHz and 4 kHz are not fast enough to cope with the dynamics. Interestingly, an update rate of 256 kHz results in a lower SNIR compared to the slower update rates (64 kHz and 16 kHz). The reason for that is the increased fluctuations in the filter

coefficients owing to the shorter integration time. Altogether, the MPM is inferior to the recursive EVD-based decomposition filter with regard to interference mitigation performance.

4.3.3 Post-Correlation Multipath Mitigation

The MMSE (as presented so far) tends to constructively combine the direct signal and the multipath components in order to maximize the received signal power. In GNSS applications, multipath reception is, however, undesirable as it distorts the range measurement between the satellite and the receiver. An extended version of the MMSE, which is less prone to multipath, is presented in this section.

In a single-antenna receiver, correlator techniques or temporal filtering may be used at baseband for the purpose of reducing multipath induced ranging errors. [77] compares some of the different correlator techniques, i.a. the standard (wide) correlator, the narrow correlator [78], the double delta ($\Delta\Delta$) correlator (also known as the "High Resolution Correlator" [79]). Eventually, the $\Delta\Delta$-correlator shows the best overall performance.

The use of an equalizer filter in the temporal domain is proposed in [40, 16] as a counter measure against multipath effects. In case of multipath reception, the correlation function $\varphi_{\hat{s}x}$ (of the front-end signal x and local signal replica $\hat{s}$) is the superposition of the main correlation triangle with its delayed copies. The equalizer filter combines time shifted samples of the input signal in such a way, that all delayed correlation triangles in the correlation function are suppressed. After equalization, only the main triangle belonging to the direct path remains.

In general, broader front-end bandwidths and shorter correlator spacings are required in order to resolve the correlation function accurately in the temporal domain. That is necessary to decompose the received signal into its LOS and multipath components, in particular, if short-delay multipath is present. Conversely, the front-end bandwidth must be kept limited to avoid the reception of interference signals from adjacent frequencies. However, limiting the front-end bandwidth flattens the peak of the correlation triangle. This causes that the direct signal's correlation triangle merges with the correlation triangles belonging to short-delay multipath signals. Under this circumstances, a separation is not available in the temporal domain. However, it may be potentially possible in the spatial domain, if the directions of the direct signal and the reflected signals clearly differ from each other.

Accordingly, this thesis proposes a novel beamformer, which is the spatial counter-

part of an equalizer filter in the temporal domain. It combines signals from different antenna elements to suppress the correlation triangles belonging to reflected signals. The principle is illustrated in Figure 4.16 for a 2-element antenna, where the steering vector of the direct signal is $\mathbf{a}^{\mathrm{T}} = [1, 1]$ and the steering vector of the reflected signal is $\mathbf{b}^{\mathrm{T}} = [1, -1]$.

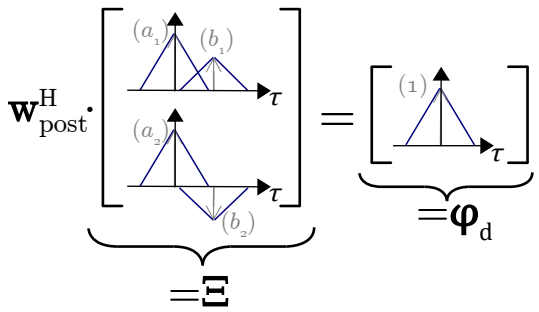


Figure 4.16: Multipath mitigation in spatial domain

In Figure 4.16, the $N_{\mathrm{ant}} \times N_{\mathrm{corr}}$-matrix

$$\boldsymbol{\Xi} = \left[\boldsymbol{\varphi}_{\hat{s}\mathbf{q}}(-\lfloor \tfrac{N_{\mathrm{corr}}}{2} - 1 \rfloor \cdot \delta\tau) \quad \cdots \quad \boldsymbol{\varphi}_{\hat{s}\mathbf{q}}(\lfloor \tfrac{N_{\mathrm{corr}}}{2} - 1 \rfloor \cdot \delta\tau) \quad \boldsymbol{\varphi}_{\hat{s}\mathbf{q}}(\lfloor \tfrac{N_{\mathrm{corr}}}{2} \rfloor \cdot \delta\tau) \right]$$

is the output of a multi-dimensional correlator bank that computes discrete values of the correlation function between the local replica signal $\hat{s}$ and the multi-dimensional quantized signal $\mathbf{q} = \mathrm{q}\{\mathbf{y}\}$ (after interference mitigation). $\mathbf{w}_{\mathrm{post}}$ is the post-correlation beamforming vector, and

$$\boldsymbol{\varphi}_{\mathrm{d}} = \frac{1}{\varphi_{\hat{s}s}(0)} \cdot \left[\varphi_{\hat{s}s}(-\lfloor \tfrac{N_{\mathrm{corr}}}{2} - 1 \rfloor \cdot \delta\tau) \quad \cdots \quad \varphi_{\hat{s}s}(\lfloor \tfrac{N_{\mathrm{corr}}}{2} - 1 \rfloor \cdot \delta\tau) \quad \varphi_{\hat{s}s}(\lfloor \tfrac{N_{\mathrm{corr}}}{2} \rfloor \cdot \delta\tau) \right]$$

contains the desired correlation values after beamforming. $\delta\tau$ is the correlator spacing ($d_{\mathrm{EL}} = 2 \cdot \delta\tau \cdot T_{\mathrm{c}}$ the early-late-spacing in code chips). $\boldsymbol{\varphi}_{\mathrm{d}}$ contains discrete values if the correlation function $\varphi_{\hat{s}s}$ between the local signal replica $\hat{s}(t)$ and the satellite signal $s(t)$ after analog signal conditioning. It can be determined during an interference-free and multipath-free signal reception and be saved for later use. An online computation is also possible based on a calibration signal, if such a signal is provided by the antenna as in [25, 26]. The use of a correlator bank is also proposed in [80]. However, unlike the proposed beamforming technique here, [80] applies the SAGE algorithm at the output of the correlator bank, which is hard to implement in practice because of its computational complexity.

The beamforming vector $\mathbf{w}_{\mathrm{post}}$ can be computed by solving the equation

$$\mathbf{w}_{\mathrm{post}}^{\mathrm{H}} \cdot \boldsymbol{\Xi} = \boldsymbol{\varphi}_{\mathrm{d}}. \tag{4.20}$$

In Figure 4.16, the solution would be $\mathbf{w}^{\mathrm{T}} = [1,1]/\sqrt{(2)}$. In general, the Least Mean Square (LMS) solution of (4.20) is

$$\mathbf{w}_{\text{post}}^{\mathrm{H}} = \boldsymbol{\varphi}_{\mathrm{d}} \cdot \mathbf{R}^{-1} \cdot \boldsymbol{\Xi}^{\mathrm{H}} \cdot \left(\boldsymbol{\Xi} \cdot \mathbf{R}^{-1} \cdot \boldsymbol{\Xi}^{\mathrm{H}}\right)^{-1},$$

where the elements of the auto-covariance matrix

$$\mathbf{R} = \mathrm{E}\big\{(\boldsymbol{\Xi} - \mathrm{E}\{\boldsymbol{\Xi}\})^{\mathrm{H}} \cdot (\boldsymbol{\Xi} - \mathrm{E}\{\boldsymbol{\Xi}\})\big\}$$

can be computed as

$$[\mathbf{R}]_{i,j} = \begin{cases} 1 - |i-j| \cdot \frac{\delta\tau}{T_{\mathrm{c}}} & \text{if } T_{\mathrm{c}} > |i-j| \\ 0 & \text{otherwise.} \end{cases}$$

A recursive way to compute the beamforming vector $\mathbf{w}_{\text{post}}$ using a gradient-based LMS algorithm is

$$\mathbf{w}_{\text{post}}(k) = \mathbf{w}_{\text{post}}(k-K) + \Delta\mathbf{w}_{\text{post}}(k) \tag{4.21}$$

$$\Delta\mathbf{w}_{\text{post}}^{\mathrm{H}}(k) = -\mu \left(\mathbf{w}_{\text{post}}^{\mathrm{H}}(k-K) \cdot \tilde{\boldsymbol{\Xi}}(k-K) - \boldsymbol{\varphi}_{\mathrm{d}}\right) \cdot \mathbf{R}^{-1} \cdot \tilde{\boldsymbol{\Xi}}^{\mathrm{H}}(k-K) \tag{4.22}$$

with

$$\tilde{\boldsymbol{\Xi}}(k) = \frac{\boldsymbol{\Xi}(k)}{\left|\mathbf{w}_{\text{post}}^{\mathrm{H}}(k) \cdot \boldsymbol{\varphi}_{\hat{s}\mathbf{q}}(0)\right|}$$

and μ the step size parameter controlling the convergence speed of the algorithm. If the *composition* step of the interference mitigation filter from Section 4.3.2 is not carried out at pre-correlation stage, it can be taken into account in (4.22) as follows:

$$\Delta\mathbf{w}_{\text{post}}^{\mathrm{H}} = -\mu \left(\mathbf{w}_{\text{post}}^{\mathrm{H}} \cdot \mathbf{U} \cdot \tilde{\boldsymbol{\Xi}} - \boldsymbol{\varphi}_{\mathrm{d}}\right) \cdot \mathbf{R}^{-1} \cdot \tilde{\boldsymbol{\Xi}}^{\mathrm{H}} \cdot \mathbf{U}^{\mathrm{H}}.$$

In the absence of multipath, the rows of $\boldsymbol{\Xi}$ are not linearly independent. Hence, the solution of (4.20) is ambiguous. For example, if no reflected signal is present in Figure 4.16 ($\mathbf{a}^{\mathrm{T}} = [1,1]$, $\mathbf{b}^{\mathrm{T}} = [0,0]$), all vectors $\mathbf{w}_{\text{post}}$ with real elements and a unit length ($|\mathbf{w}_{\text{post}}| = 1$) are possible solutions. However, the optimum solution with regard to the SNR is the MMSE beamformer, i.e. $\mathbf{w}_{\text{post}} = \mathbf{a}^{\mathrm{H}} = [1,1]/\sqrt{2}$. In general, the elements of the beamforming vector $\mathbf{w}_{\text{post}}$ should have similar magnitudes ($|w_1| \approx |w_2| \approx \cdots \approx |w_{N_{\text{ant}}}|$) if signals from different antenna elements have nearly equal magnitudes, i.e. $|a_1| = |a_2| = \cdots = |a_{N_{\text{ant}}}|$, and SNRs. To push the solution of the recursive computation in (4.21) towards a vector $\mathbf{w}_{\text{post}}$ with preferably a well-balanced weighting of the array elements, one can include the following scaling step after computing (4.21):

$$\tilde{w}_i = w_i \cdot \left(1 + \frac{\lambda}{|w_i|}\right) \quad (0 < \lambda < \frac{1}{\sqrt{N_{\text{ant}}}}),$$

where λ is the predefined lower bound for the absolute value of an element w_i of $\mathbf{w}_{\text{post}}$.

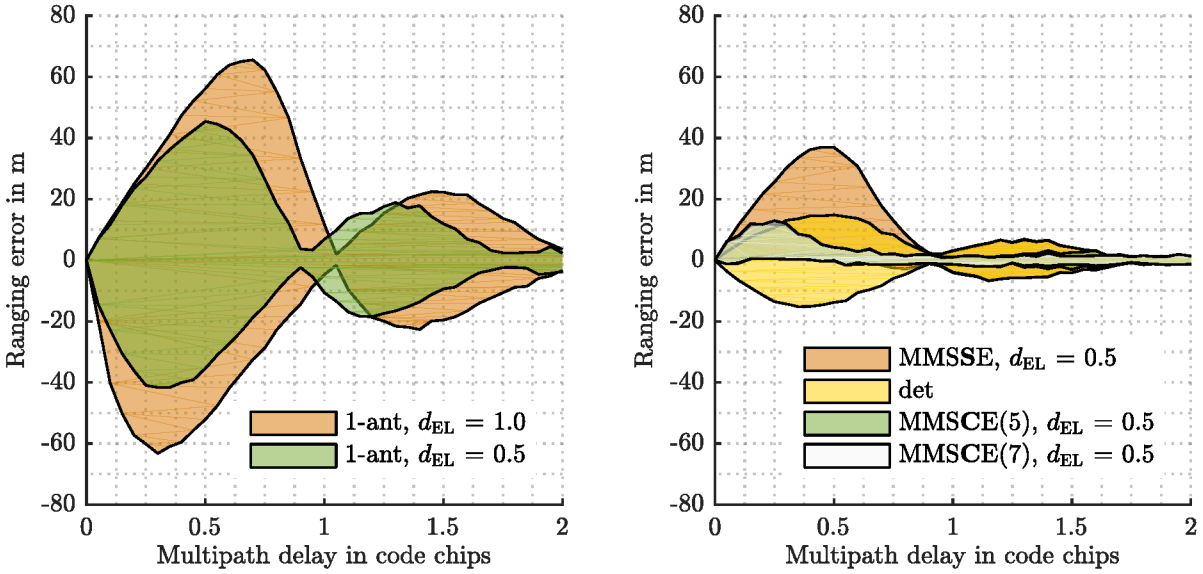
The presented algorithm attempts to minimize the mean square difference between the actual correlation function and the ideal correlation function $\boldsymbol{\varphi}_{\text{d}}$. Hence, it is named the Minimum Mean-Square *Correlation*-Error Beamformer (MMS**C**E) in this thesis. As of now, the MMSE beamformer from Section 4.1.5 will be called the Minimum Mean-Square *Signal*-Error Beamformer (MMS**S**E), to emphasize that it minimizes the mean square difference between the desired temporal signal sequence and the beamformer's output signal.

Simulation Results

Error envelope plots are frequently used to analyze ranging errors caused by multipath and to compare different mitigation techniques. These plots are based on the two-path reception model. In this model, the ranging error is at its highest if the reflected signal's carrier is in phase with the direct signal or if its phase is exactly 180° shifted relative to the direct signal's phase. All other phase relations result in an error between these two extreme cases, which define the error envelopes. The error envelopes in this section were determined by means of simulations, where the reflected signal has a constant carrier frequency that is slightly different from the direct signal's carrier frequency. This way, all possible relative carrier phases occur during the simulation. The error envelopes can then be determined as the maximum positive and minimum negative value of the ranging error for a certain multipath delay.

Figure 4.17a and Figure 4.19a show the error envelopes of a single-antenna receiver using the $\Delta\Delta$-discriminator. Figure 4.17b and Figure 4.19b show the error envelopes of a 2×2-array antenna receiver using different beamformers in combination with the $\Delta\Delta$-discriminator after beamforming. Two variants of the MMSCE beamformer are included, one using $N_{\text{corr}} = 5$ and another one $N_{\text{corr}} = 7$ correlation values. Besides the MMSSE and the MMSCE beamformers, the deterministic beamformer from Section 4.1.1 is also considered. Here, since there is no RFI ($\mathbf{R}_{\mathbf{xx}} \approx \sigma_n^2 \cdot \mathbf{I}$), the deterministic beamformer is equal to MVDR. Figure 4.18 and Figure 4.20 show the RMS ranging error.

In contrast to the MMSSE and the MMSCE, the deterministic beamformer is not a blind beamformer, i.e. it requires calibration of the antenna and knowledge (or estimation) of the satellite signal's direction and antenna orientation. The estimation of the signal directions -especially in case of multipath reception- is a challenge in itself and is not the focus of this thesis. Here, the known steering vector from the simulation was used for the deterministic beamformer.



(a) Single antenna (b) 2x2-array-antenna

Figure 4.17: Ranging error envelope (front-end bandwidth 2 MHz, multipath-to-direct-signal-ratio of -3 dB, Scenario 1)

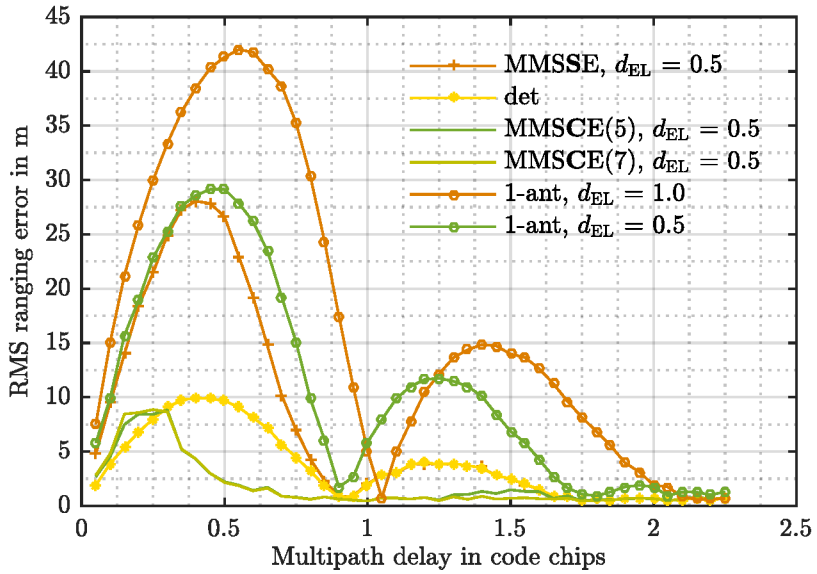


Figure 4.18: RMS ranging error (front-end bandwidth 2 MHz, multipath-to-direct-signal-ratio of -3 dB, Scenario 1)

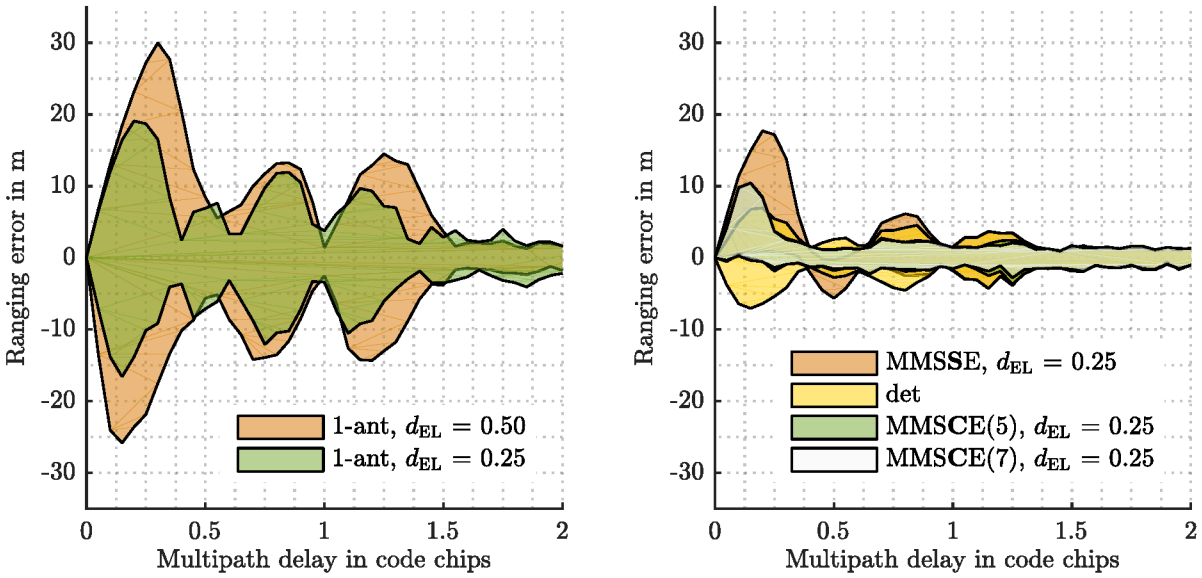
The first observation is that the array-antenna combined with beamforming provides a significant improvement compared to the single antenna reception (compare Figure 4.17a with Figure 4.17b or Figure 4.19a with 4.19b). Increasing the front-end bandwidth from 2 MHz to 4 MHz while shortening the early-late correlator spacing d_{EL} from 0.5 to 0.25 code chips also reduces the ranging errors in general. Reducing the correlator spacing $\delta\tau$ below $\frac{1}{T_{\mathrm{c}} \cdot B}$ (with T_{c} the chip duration and B the signal bandwidth after analog signal conditioning) does not improve the result.

Multipath reception does not affect the ranging performance, if the front-end bandwidth is 2 MHz and the reflected signal's relative delay is greater than 2 code chips (or greater than 1.5 code chips in case of a front-end bandwidth of 4 MHz). In this region, the ranging error is unbiased and exclusively determined by noise. It increases when the correlator spacing is reduced, e.g. from $d_{\mathrm{EL}} = 0.5$ to $d_{\mathrm{EL}} = 0.25$ code chips in Figure 4.20.

The errors of the deterministic beamformer and the MMSSE overlap if the relative delay is longer than 0.8 code chips. Their ranging error may increase up to 4 meters in case of a front-end bandwidth of 2 MHz and up to 2 meters in case of 4 MHz. The MMSCE entirely removes the error induced by multipath, if the relative delay is greater than 0.8 code chips. Only noise-induced errors remain. The difference between the MMSCE using $N_{\mathrm{corr}} = 5$ and using $N_{\mathrm{corr}} = 7$ values is insignificant. For comparison, [80] uses a correlator bank with $N_{\mathrm{corr}} = 2/\delta\tau + 1 \geq 2 \cdot B \cdot T_{\mathrm{c}} + 1$ to compute the input values of the SAGE algorithm.

As shown in Figure 4.18, the MSSCE beamformer achieves the best performance for multipath relative delays less than 0.8 code chips, except for very short relative delays (less than 0.3 code chips). When it comes to very short relative delays, the deterministic beamformer yields lower ranging errors than the MSSCE. If the front-end bandwidth is 4 MHz (Figure 4.19b and in Figure 4.20), the interval where the deterministic beamformer performs better than the MSSCE is even narrower (limited to relative delays less than 0.2 code chips). Very-short-delay multipath is problematic for the MMSCE, as in this case the correlation triangles of the reflected signal and the direct signal cannot be clearly separated from each other. Otherwise, the MSSCE beamformer manages to remove the multipath effects, so that only noise induced errors remain in the range estimation.

Figure 4.21 shows the adaptive gain patterns resulting from the different beamformers. The gain of the MMSSE beamformer in the LOS direction is not as strong as the gains provided by the other two beamformers. Instead of forming a distinct beam in the LOS direction, the MMSSE beamformer is more likely to combine the direct signal and the reflected signal in a constructive way in order to maximize the received



(a) Single antenna (b) 4x4-array-antenna

Figure 4.19: Ranging error envelope (front-end bandwidth 4 MHz, multipath-to-direct-signal-ratio of -3 dB, Scenario 1)

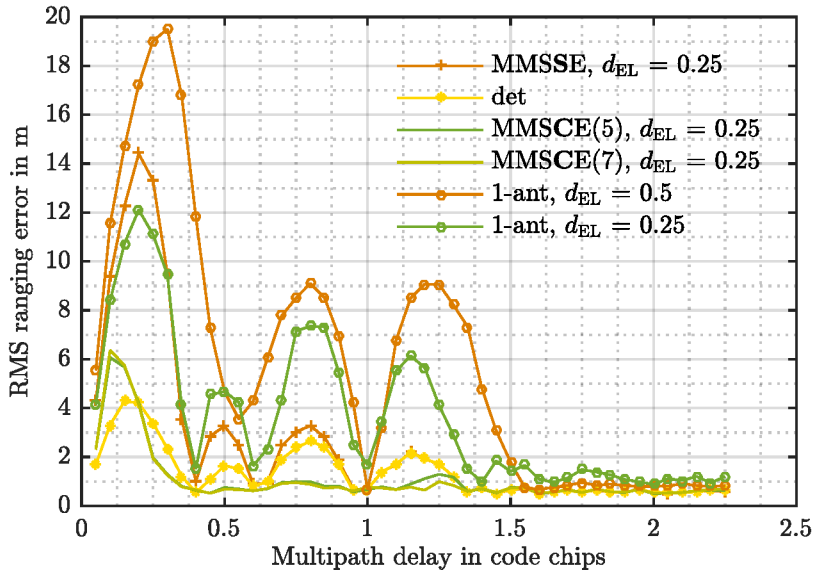
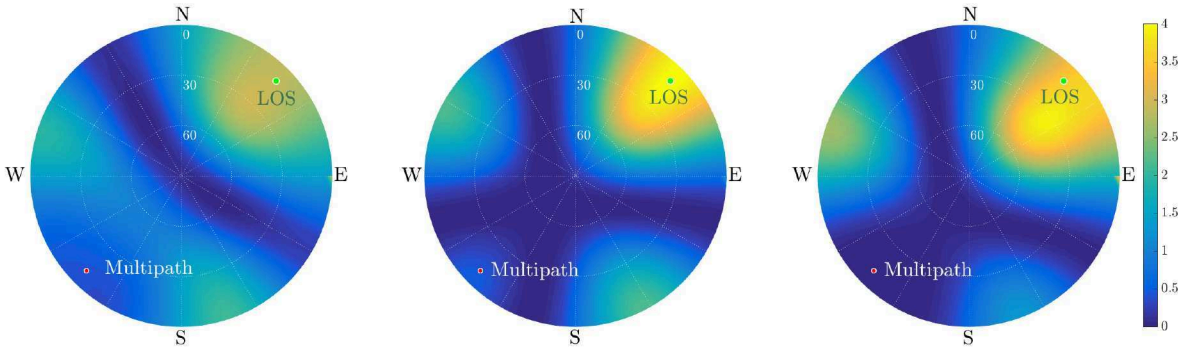


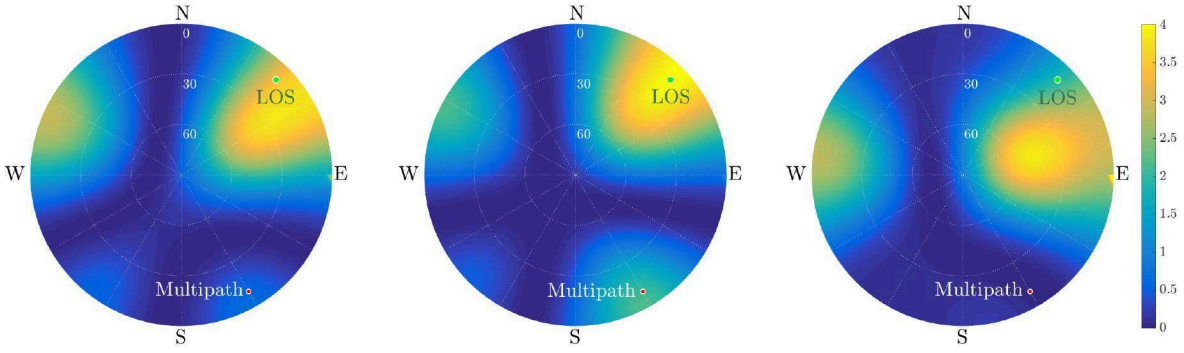
Figure 4.20: RMS ranging error (front-end bandwidth 4 MHz, multipath-to-direct-signal-ratio of -3 dB, Scenario 1)



(a) MMSSE (b) Deterministic (c) MMSCE

Figure 4.21: Adaptive gain pattern (Scenario 1)

signal power. Unlike the MMSSE, the deterministic beamformer focuses a beam effectively in the LOS direction. However, it does not control the side lobes in the gain pattern. In the example in Figure 4.21 (Scenario 1), the reflected signal's direction just luckily does not coincide with a strong side lobe. This will not be the case for the following example. The MMSCE forms a beam in the LOS direction while purposefully suppressing reflected signals.



(a) MMSSE (b) Deterministic (c) MMSCE

Figure 4.22: Adaptive gain pattern (Scenario 2)

Whether the deterministic beamformer performs better than the MSSCE for very short relative multipath delays is actually a question of the multipath directions. To illustrate this point, Figure 4.22 shows the gain patterns that result from a different multipath scenario (Scenario 2). Unlike in Figure 4.21, now the reflected signal's direction coincides with an uncontrolled stronger side lobe. As the deterministic beamformer is determined by the LOS direction only, which is the same as in Scenario 1 from Figure 4.21, the gain pattern remains unchanged. However, the output of the deterministic

beamformer is more affected by multipath compared to the first scenario. The MMSCE beamformer adapts to the new situation by shifting the main lobe slightly away from the LOS direction. This causes a gain loss in the LOS direction but ensures the desired attenuation on the reflected signal's direction. Overall, the RMS ranging error (Figure 4.23) of the MMSCE beamformer is lower than the other two considered beamformers.

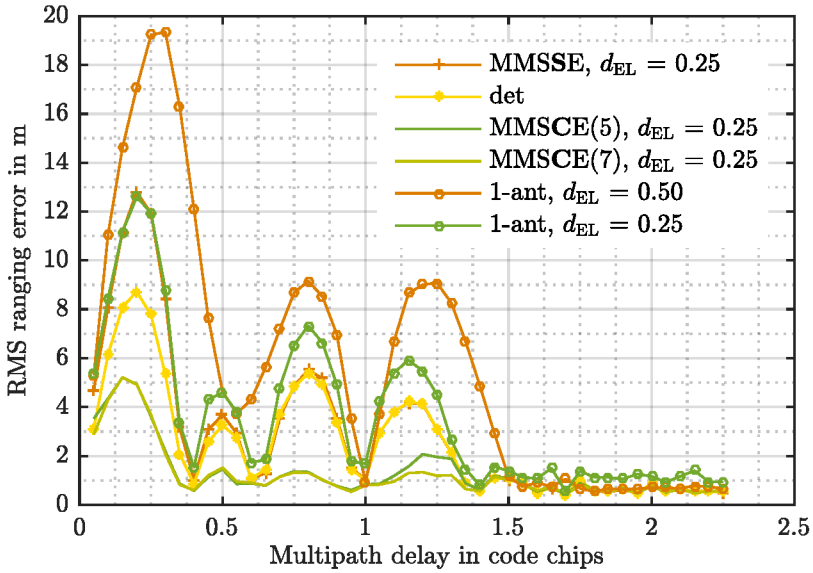


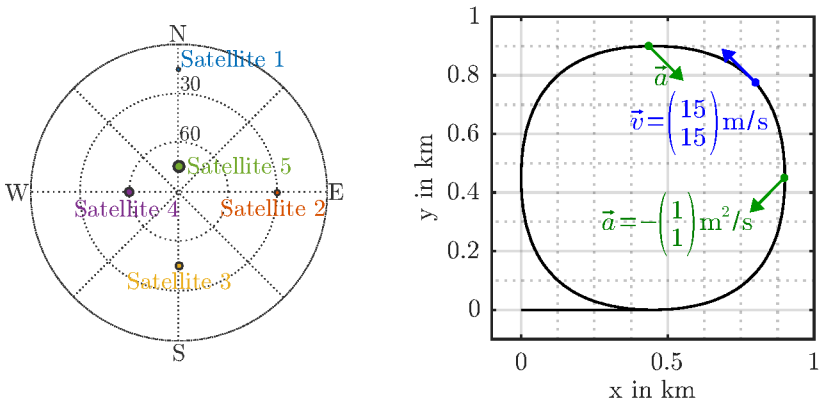
Figure 4.23: RMS ranging error (front-end bandwidth 4 MHz, multipath-to-direct-signal-ratio of -3 dB, Scenario 2)

4.4 Signal Outages and Vector Tracking Loops

If the direction of a strong interferer is close to the direction of a satellite signal, the reception of the satellite signal is practically blocked even if the interference signal is suppressed by means of spatial processing. The receiver may employ vector-tracking-loops (VTL) instead of the conventional tracking loops in harsh situations in order to overcome the gaps in the signal reception caused by temporary interference signals. Such interferences occur, for example, if the receiver goes past jamming devices. While the benefit of the VTL in case of signal shadowing is well-known, the usage of the VTL in the context of interference and beamforming is first presented in this thesis.

Conventionally, the tracking loops, that control the carrier frequency and code delay of the local signal replicas, operate individually for each satellite. In contrast, VTL jointly control all carrier frequencies and all code delays. They combine the discriminators from all channels, the knowledge about the satellite positions and the receiver's position, and their movements in order to compute the control values.

The main advantage of the VTL is that they can continue estimating the parameters of a satellite signal with a weak reception (due to shadowing or jamming) based on other satellites with a clear LOS. Below, this advantage is demonstrated by means of a simulation. The simulated satellite constellation and the receiver's movement are illus-



(a) Sky plot (b) Simulated path

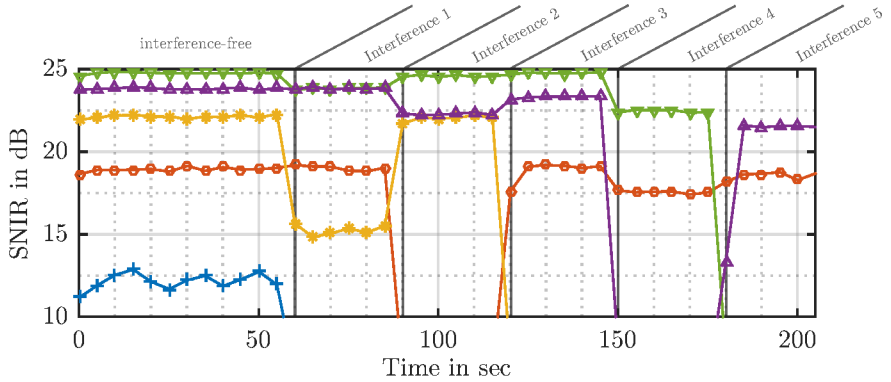
Figure 4.24: Simulation conditions

trated in Figure 4.24. Five satellite signals are received by the array-antenna. Satellite signals coming from low elevations are weaker, which is indicated by the smaller circles used for weaker satellite signals in the sky plot. The receiver moves within an area of ca. 1 km^2, it follows a round route and reaches a maximum velocity of $15\sqrt{2}$ m/s.

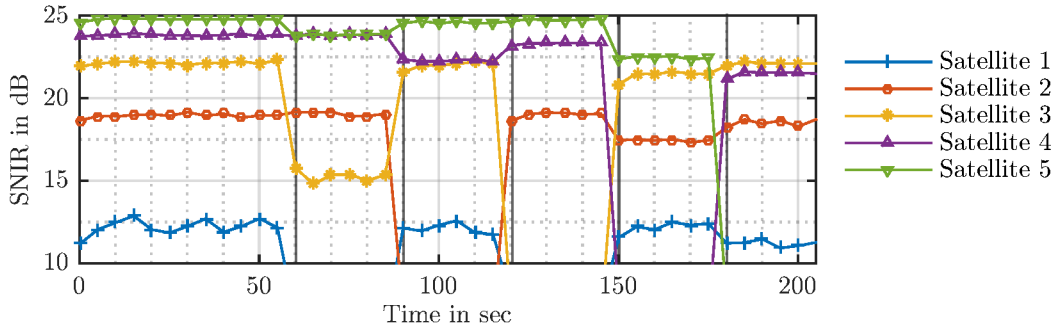
In the simulation, interference signals are turned on one after another each for a limited duration of 30 s. The first interference signal, for instance, is turned on at $t = 60$ s and comes exactly from the direction of Satellite 1. The second interferer appears at $t = 90$ s and comes from the direction of Satellite 2; at the same moment the first interferer disappears, and so on.

Figure 4.25 shows the SNIR after correlation for the conventional tracking loops and the VTL. In the first period (starting at $t = 60$ s) the first satellite's signal is entirely blocked due to the interference signal from the same direction as the satellite signal. The signal attenuation in space is not limited to a sharp region but also affect the reception of the signal from nearby directions. This can be seen in the adaptive gain pattern given in Figure 4.26, where the attenuation in the interference direction affects also channels 3 and 5 in addition to channel 1. The SNIR values of these channels also drop during interference 1.

Figure 4.27 shows the error in the estimated range between the receiver and Satellite 1, and the error in the estimated range rate during the first interference period. The



(a) Conventional tracking loops



(b) Vector tracking loops

Figure 4.25: SNIR after correlation

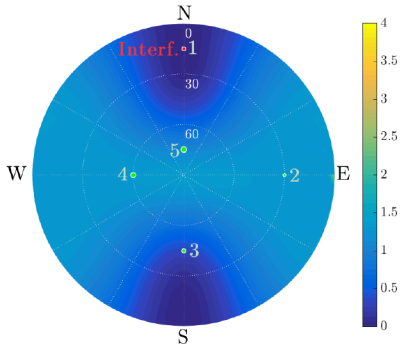
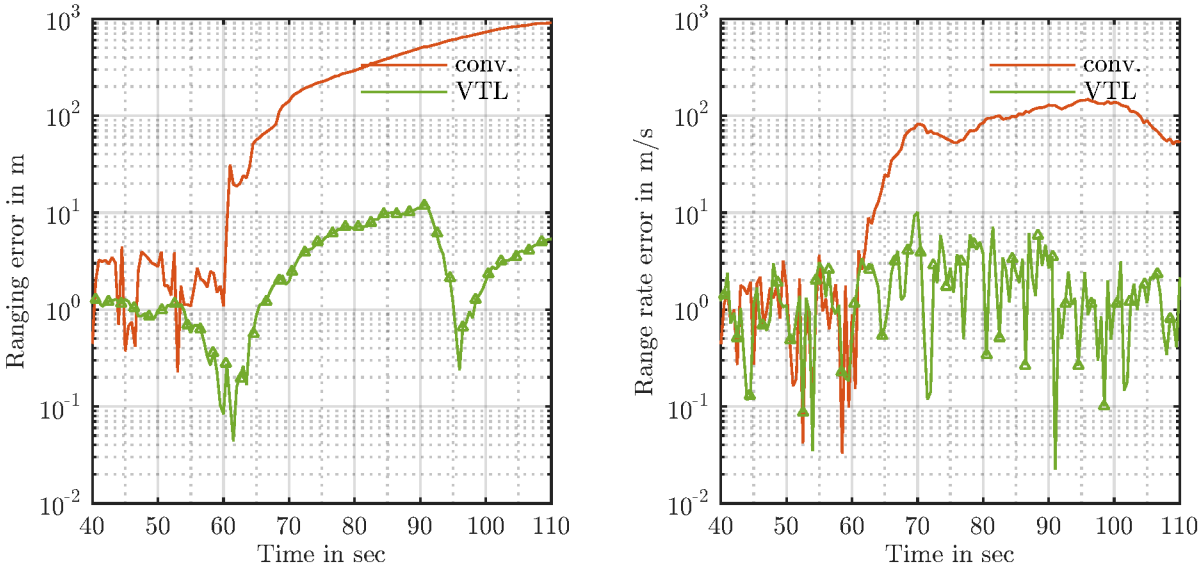


Figure 4.26: Beam pattern after interference mitigation during the first interference period (60 s - 90 s)

conventional tracking loop is not able to track the signal of Satellite 1 during this period. The error growth is significantly faster than the error growth of the VTL. When the interference disappears at $t = 90$ s, the tracking error of the conventional loops is already large enough to make the receiver completely loose track of Satellite 1. Similarly, the receiver looses track of Satellite 3 after the third interference period. The VTL, however, continue to estimate the satellite signal parameters based on other received satellite signals, even during strong interference from the satellite signal's direction. They can start tracking the satellite signal immediately after the interference disappears, i.e. the SNIR jumps back to its earlier value.



(a) Ranging error

(b) Range rate error

Figure 4.27: Ranging error and range rate error of Channel 1 during interference from satellite signal direction (60 s - 90 s)

In case of the conventional loops, re-acquisition is necessary to find the lost satellite signals. Affected satellites are not available for the PVT computation during the time required for re-acquisition and the settling time of the tracking loops. As the VTL can overcome short-term signal outages without loosing track of the satellite signal parameters, they provide a more continuous signal tracking in the presence of appearing and disappearing interferers. (The previously presented simulation was purposed to demonstrate the tendency of the conventional loops to easily loose track of the satellite signals during strong interference. It does not involve the additional time required for re-acquisition.)

Chapter 5

Space-Time Processing

The previous chapter presented the possibility of mitigating interference signals in a multi-antenna receiver using beamforming, i.e. spatial-only processing. Regardless of the waveform of the interference, spatial processing is an effective method against interference, as long as the interference signal has a distinct signal direction.

Broadband noise interference, in particular, does not show any temporal correlations. Hence, it cannot be suppressed in the temporal domain and must inevitably be dealt with in the spatial domain. Narrowband interference, on the contrary, shows spatial as well as temporal correlations. It can be mitigated both in the spatial or in the temporal domain. Nevertheless, the potential of the temporal domain should be exploited before making use of the spatial domain. That is because the spatial degrees of freedom, i.e. the maximum number of interference directions that can be canceled, are already limited by the typically small number of antenna elements. Therefore, they should be saved for mitigating broadband interference. Furthermore, a spatial filter with limited degrees of freedom does not enable a sharp separation of the signal directions. Thus, the mitigation of an interference signal in the spatial domain may potentially blot out an angular sector where a satellite signal lies [81]. If possible, temporal processing is to be preferred over spatial processing also from this point of view. (It can be mentioned at this point, that besides interference mitigation temporal filtering can be employed to alter the temporal characteristics of the input signals in general. In [82], for example, it is used for sub-carrier shaping of BOC signals to remove the side lobes in the auto-correlation function.)

Spatial degrees of freedom can be combined with temporal degrees of freedom to realize a Space-Time Adaptive Processing (STAP) filter, that can efficiently mitigate different types of interference at the same time [83, 84]. Altering the input signal in the temporal domain can thereby cause a distortion of the correlation triangle and may

produce bias errors in the code and carrier phase measurements (Antenna induced biases discussed, e.g., in [85] are neglected in this thesis.). Although pointing out the potential distortions caused by the temporal filtering, [86] does not investigate this phenomenon in detail. Instead, the authors suggest the use of a detection unit, in order to turn off temporal filtering when interference is not present. The STAP filter in [49] employs tapped delay lines with taps distributed over multiple code periods. By exploiting the periodicity of the GNSS signals, [49] choses the filter coefficients under the constraint, that the STAP does not induce any distortions to the GNSS signals. Nevertheless, this method ends up in very long tapped delay lines. [87] proposes the use of an LCMV spatial-temporal filter with a constraint to ensure that at least the correlation peak is not shifted by the filtering. (This does not guarantee that the symmetry of the correlation function is preserved, which is actually crucial for the code tracking loop to function properly.) Both filters from [49] and [87] are not blind, i.e. they require knowledge of the antenna/front-end response, antenna orientation and DOAs of the GNSS signals.

The main disadvantage of STAP relative to space-only processing is the large dimensionality of the space-time correlation matrix relative to the spatial correlation matrix. Large number of taps are required in the STAP to form sharp 'point-nulls' at the angle-frequency coordinates of an interferer and thereby minimize the signal distortions [88]. This translates into increased computational complexity of the filter and slower convergence of gradient-based filter adaptation algorithms [81]. For this purpose, [81, 88] present a space-time preprocessor based on the multistage nested Wiener filter to reduce the dimensionality of the filter.

This thesis presents a STAP with decoupled temporal and spatial components. Decoupled means in this context that the spatial and temporal filter coefficients are computed independently from each other [89]. The filter consists of three stages [90, 91]: a Notch Filter (NF), a spatial filter and an EQualizer Filter (EQ). The NF at the first stage is realized as a bank of Finite Impulse Response (FIR) filters and suppresses temporally correlated (narrowband) interference in the temporal domain. Previously mentioned methods avoid phase biases and signal distortions by applying constraints to the filter coefficients and by increasing the number of taps, i.e. the dimensionality of the filter. In contrast, the NFs here are allowed to distort the signals in the first place. The spatial filter at the second stage suppresses wideband interference, which gets through the first stage. The last filter stage is required to reverse the distortions induced by the NFs. As a result, this filter structure avoids GNSS signal distortions without necessarily increasing the dimensionality of the STAP filter.

This chapter is structured as following: In Sections 5.1 and 5.2, the temporal filter

components are presented. In Section 5.3, these filter components will be combined with the recursive EVD-based spatial filter from the previous chapter to form a spatial-temporal filter. Section 5.4 discusses the implementation aspect. Section 5.5 shows simulation results that reveal the advantages of the STAP over the spatial-only processing. Finally, Section 5.6 provides a brief comparison between the presented decoupled filter and the joint filter approach.

5.1 Notch Filters

In spread spectrum communication systems, the use of NFs for interference cancellation often results in a large improvement, if the interference is narrowband relative to the bandwidth of the desired signal. In particular, an adaptive FIR filter can be used to predict the interference and subtract it from the received signal [92]. The LMS algorithm is commonly used for adjusting the filter coefficients.

Since, in general, FIR filters require longer tapped delay-lines compared to the IIR filters, the use of IIR filters for suppression of narrow-band interference is also proposed [93]. [86] applies this approach to GNSS for mitigating CW interference. In [94, 95], the use of the notch filter is extended to swept frequency interference. The technique used in [86, 94, 95] for filter adaptation minimizes the output power based on the iterative LMS algorithm.

Besides the time-domain filtering, transform domain filtering techniques also exist [93]. These algorithms transform the received signal into spectral domain using techniques like the short-time DFT [96, 97], the Gabor [98] or the wavelet transform [99]. The spectral domain is used to either directly attenuate interference by blanking the corresponding frequency bins or to extract interference parameters for adapting a separate notch filter. For equal computational complexity (equal number of spatial and temporal degrees of freedom) space-time processing slightly outperforms the space-frequency processing [58, 65].

This thesis focuses on the direct form of the FIR filter structure. The primary goal is to demonstrate the potential of using a combined spatial-temporal filter for interference mitigation. Although the implementation aspect is discussed in Section 5.4, this will not be the main focus. Hence, the direct form of the FIR filter over IIR was chosen to simplify the analysis and to avoid stability issues. The structure of the FIR-filter of the order M is given in Figure 5.1.

The PM approach, which was introduced in Section 4.1 in the context of spatial processing, can be applied also here to compute the adaptation of the tap-weight vector

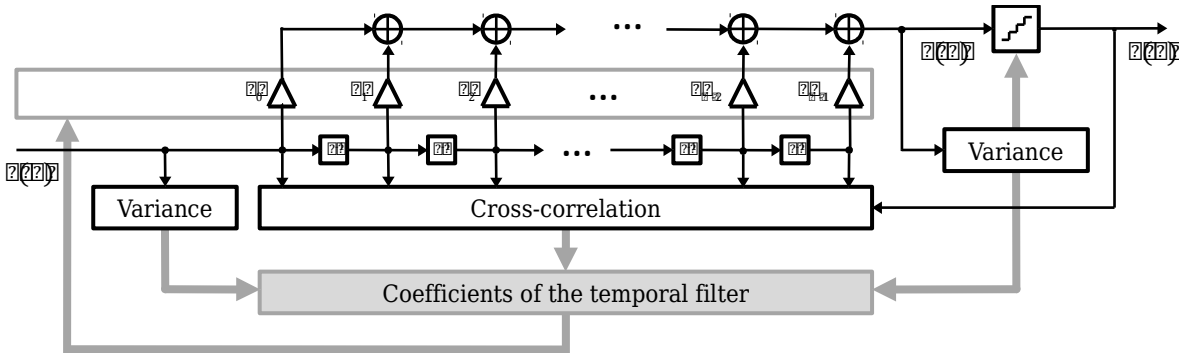


Figure 5.1: Notch filter realized as FIR filter

$\mathbf{b}^{\mathrm{T}} = [b_0, b_2, \cdots, b_M]$ of the NF. Analogous to (4.7), here, the filter output

$$y = \sum_{m=0}^{M-1} b_m \cdot x(k-m)$$

is composed of the delayed samples of the input signal $x(k)$. The filter coefficients can be computed iteratively using an LMS based algorithm. The coefficients are updated after every K samples according to

$$\mathbf{b}(k) = \mathbf{b}(k-K) + \Delta\mathbf{b}(k).$$

The update value $\Delta b_m(k)$, by which the coefficient b_m is changed, is given by

$$\Delta b_m(k) = -\mu(k) \cdot \frac{1}{K} \sum_{k'=k-K}^{k-1} y(k') \cdot x^*(k'-m). \tag{5.1}$$

Note that this is the cross-correlation between the input signal x and the output signal y of the NF. $\mu(k)$ is the step size parameter, that must be chosen as

$$0 < \mu(k) < 2/\text{tap-input-power}$$

with

$$\text{tap-input-power} = \sum_{m=0}^{M-1} \mathrm{E}\{|x(k-m)|^2\} = M \cdot \mathrm{E}\{|x(k)|^2\},$$

in order to guarantee convergence of the algorithm [73].

Like in Section 4.1.7, y can be replaced by its re-quantized value $q = \mathrm{q}\{y\}$, and μ by

$$\tilde{\mu} = \frac{\sigma_y}{\sigma_q} \cdot \mu$$

in (5.1) to reduce the computational complexity of (5.1) in full-adders.

5.2 Equalizer Filter

While suppressing interferers, the NF generates echoes of the original satellite signal as a side effect. As a result, time-shifted copies of the main correlation triangle appear in the correlation function of the filter output with the local satellite signal replica (Figure 5.2a). Similar to the echoes produced by signal reflections (multipath), an overlap of the echo-triangles with the main triangle disrupts the satellite tracking loops.

As a first measure, the use of a tap-spacing greater than $2\times$code-chip-duration helps against filter induced distortions to the correlation triangle (Figure 5.2b). This would avoid an overlap of the main triangle with the echo-triangles, if the received signal's bandwidth was not limited by the front-end. The correlation function of a satellite signal with the local signal replica is, however, not shaped as a triangle with a sharp peak and a limited span. Instead, it is flattened by the BPF in the analog front-end and has side lobes beyond $\tau = T_c$. Hence, a clean separation of the echo "triangles" from the main "triangle" is not possible.

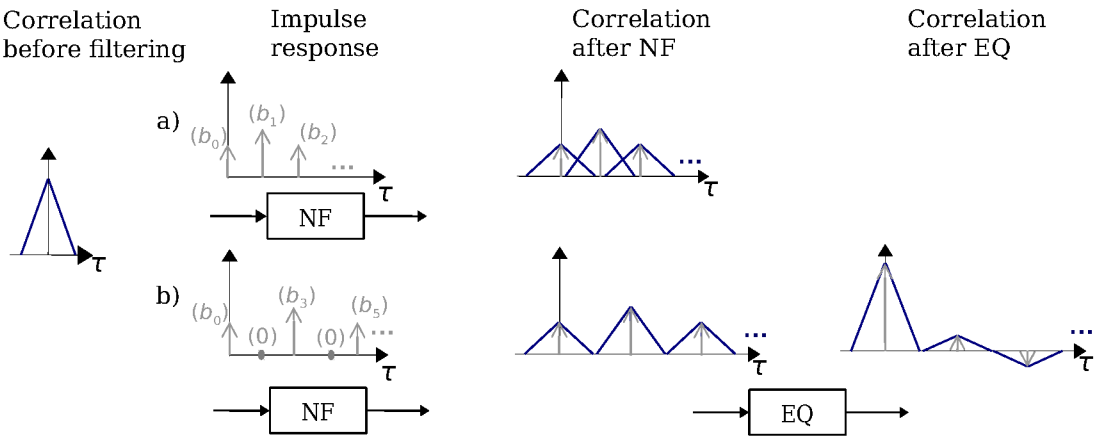


Figure 5.2: Effect of the temporal filter on the correlation function: a) notch filter with narrow tap-spacing b) notch filter with a wide tap-spacing followed by an equalizer filter

In order to suppress the echoes produced by the NF and amplify the main correlation triangle, an equalizer filter (EQ) is applied in the second stage of the temporal filter (Figure 5.2b). The EQ is also realized as an FIR filter with M_{EQ} taps. The tap-weight vector $\mathbf{b}_{\mathrm{EQ}}$ suppressing the echoes is the least-mean-square solution of the equation

$$\mathbf{b}_{\mathrm{EQ}} \cdot \mathbf{B} = \mathbf{d},$$

where

$$\mathbf{B} = \begin{bmatrix} b_0 & b_1 & \cdots & b_{M-1} & & & \mathbf{0} \\ & b_0 & b_1 & \cdots & b_{M-1} & & \\ & & b_0 & b_1 & \cdots & b_{M-1} & \\ \mathbf{0} & & & \ddots & & & \ddots \end{bmatrix}$$

is a band-matrix composed of the shifted copies of $\mathbf{b}$ and

$$\mathbf{d} = \begin{bmatrix} 0 & \dots & 0 & 1 & 0 & \dots & 0 \end{bmatrix}$$

is the desired combined impulse response of the NF and the EQ. $\mathbf{d}$ indicates that all copies of the correlation triangles have to be zeroed but one. A gradient-based algorithm to find the solution iteratively is given by

$$\mathbf{b}_{\mathrm{EQ}}^{i}(k) = \mathbf{b}_{\mathrm{EQ}}^{(i-1)}(k) + \mu_{\mathrm{EQ}} \cdot (\mathbf{d} - \mathbf{b}_{\mathrm{EQ}}^{(i-1)}(k) \cdot \mathbf{B}) \cdot \mathbf{B}^{\mathrm{H}}$$

with the initiation $\mathbf{b}_{\mathrm{EQ}}^{0}(k) = \mathbf{b}_{\mathrm{EQ}}^{I}(k-K)$. Since the tap-weight vector $\mathbf{b}$ of the NF is changed slowly by the gradient-based algorithm given in Section 5.1, few iterations are required after each update of $\mathbf{b}$ to adapt $\mathbf{b}_{\mathrm{EQ}}$ to the updated value $\mathbf{b}(k)$.

5.3 Combined Filtering

Figure 5.3 shows the spatial-temporal filter that combines the recursive spatial filter described in Section 4.3.2 and the temporal filter described in Section 5.1. White blocks represent computations realized as dedicated hardware blocks, while gray blocks are software tasks mapped to the embedded processor.

The first stage of the combined filter is a bank of N_{ant} NFs to suppress temporally correlated interference. The NFs are followed by the decomposition of the temporally filtered signal into its orthogonal spatial components.

Estimation of the spatial and the temporal filter coefficients are decoupled from each other. The spatial coefficients of the filter are derived from the spatial covariance matrix of the quantized output. If the filter coefficients are adapted correctly, narrowband interference is mitigated by the NFs and only wideband interference is detectable in the spatial covariance matrix. In other words, the spatial filter ignores narrowband interferers in the steady state. The coefficients of the NFs are determined based on the cross-correlation between the quantized filter output and the filter input signal. It is a justifiable assumption, that an interferer is received by all antenna elements and the same temporal interference characteristics can be observed for all antennas. Therefore,

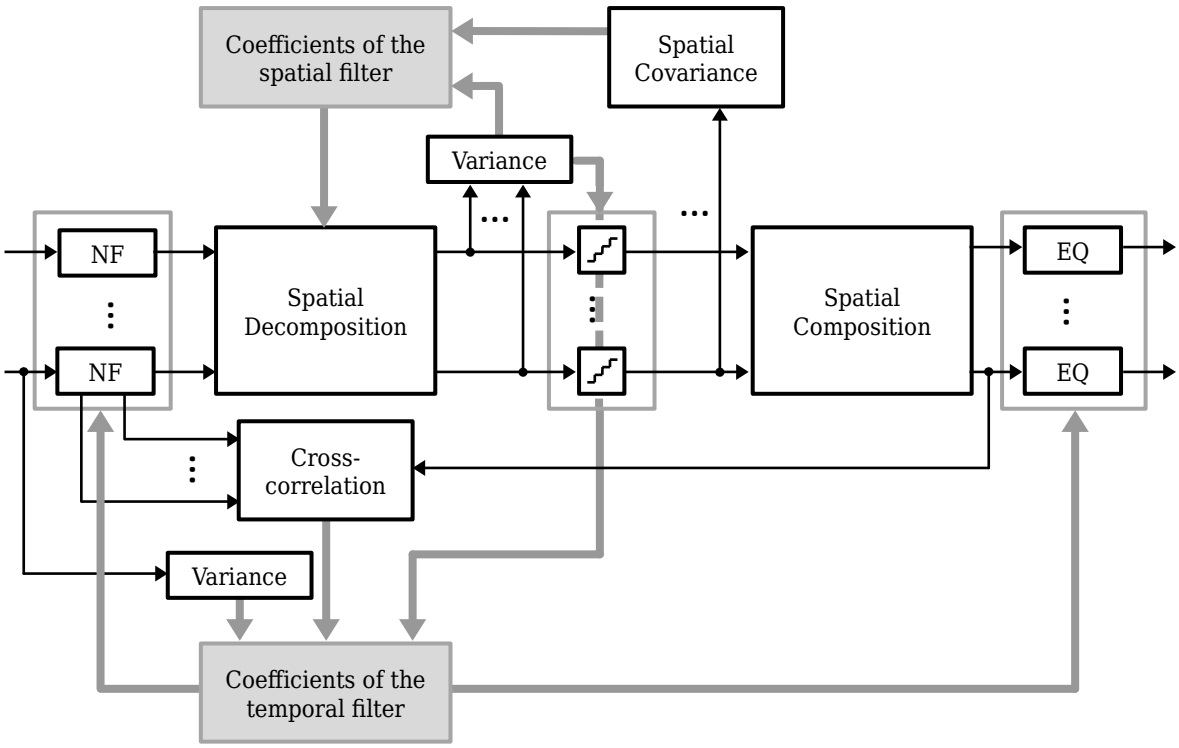


Figure 5.3: Combined Spatial-Temporal Filter [90]

it is sufficient to compute the cross-correlation for one antenna and use one common tap-weight vector for the NFs.

Here, the composition step, which was shifted to the post-correlation stage in [71], is necessarily computed at the pre-correlation stage. Otherwise, the carrier phase ambiguity induced by the decomposition step interferes with the estimation of the temporal filter coefficients. Computation of the variance at the output of the NF (see Figure 5.1) can be omitted, because the mean variance after decomposition is equal to the mean variance before decomposition.

Simulations showed that the interference mitigation performance of the combined filter was improved if the tap-weight vector $\mathbf{b}$ was normalized by its Euclidean norm after each coefficient update. However, if $\mathbf{b}$ is normalized, it does not converge back to the default vector $\mathbf{b}_0 = [1, 0, \cdots, 0]$, after interference signals disappear. Since the EQ realized as an FIR is not capable of perfectly suppressing the echoes for all possible values of $\mathbf{b}$, the "normalized power minimization algorithm" may slightly degrade the SNR in the absence of interference. To avoid an unnecessary generation of echoes, $\mathbf{b}$ needs to be slowly forced towards $\mathbf{b}_0$ if interference is not present. The presence of narrowband interference can be checked by comparing the signal power at the input and at the output of the NFs. If there is no narrowband interference, the input and the output powers are nearly equal.

5.4 Implementation

In [91], the VHDL implementation of the STAP filter in Figure 5.3 using fixed-point arithmetic was presented. Generic parameters of the implementation are

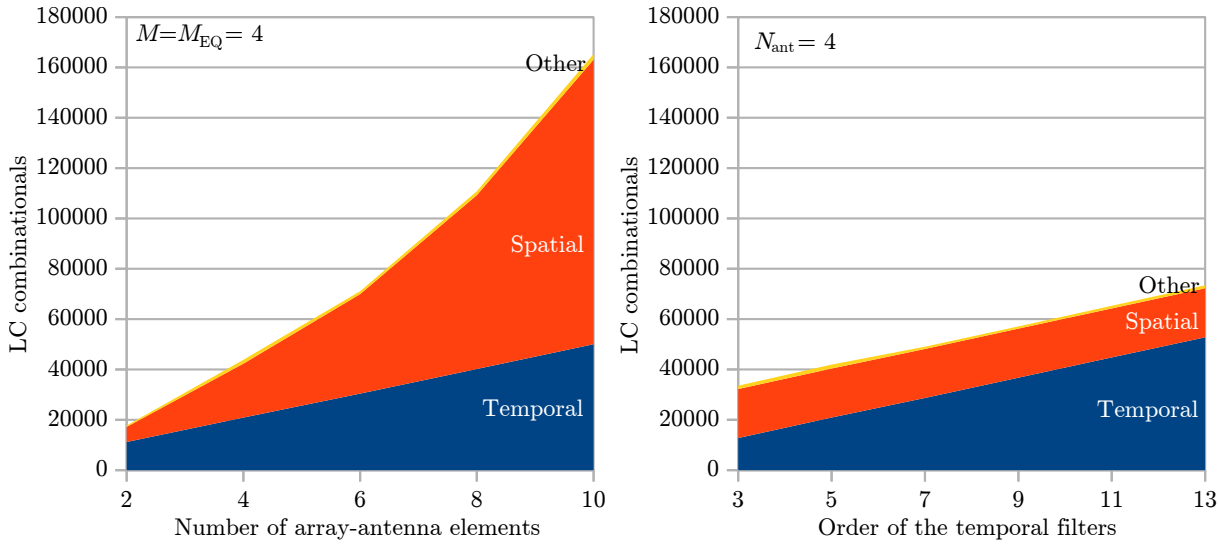
- the number N of the antenna elements,
- the order M of the NFs, M_{EQ} of the EQs,
- the word length n_x of the input signals, n_{SF} of the coefficients of the spatial filter, n_{NF} of coefficients of the NFs, n_{EQ} of the coefficients of the EQs, and
- the observation time K in samples (only powers of two are allowed).

The word length growth due to the arithmetical operations is allowed inside the computational blocks. A final word length of

$$n_x + n_{\text{NF}} + 1 + \lfloor \log_2(M+1) \rfloor$$

is, for example, reached inside the NFs. Provided that the tap-weight vectors and the columns of the decomposition matrix are normalized by their Euclidean norm, the word length at the output of the filter blocks can be reduced to the original data word length w/o causing overflows. Thus, a constant data word length of n_x is preserved between the computational blocks until re-quantization takes place. After re-quantization, signals are represented with 2 bits, one sign and one magnitude bit. The following filter blocks operate with this simplified number representation and have correspondingly lower hardware requirements.

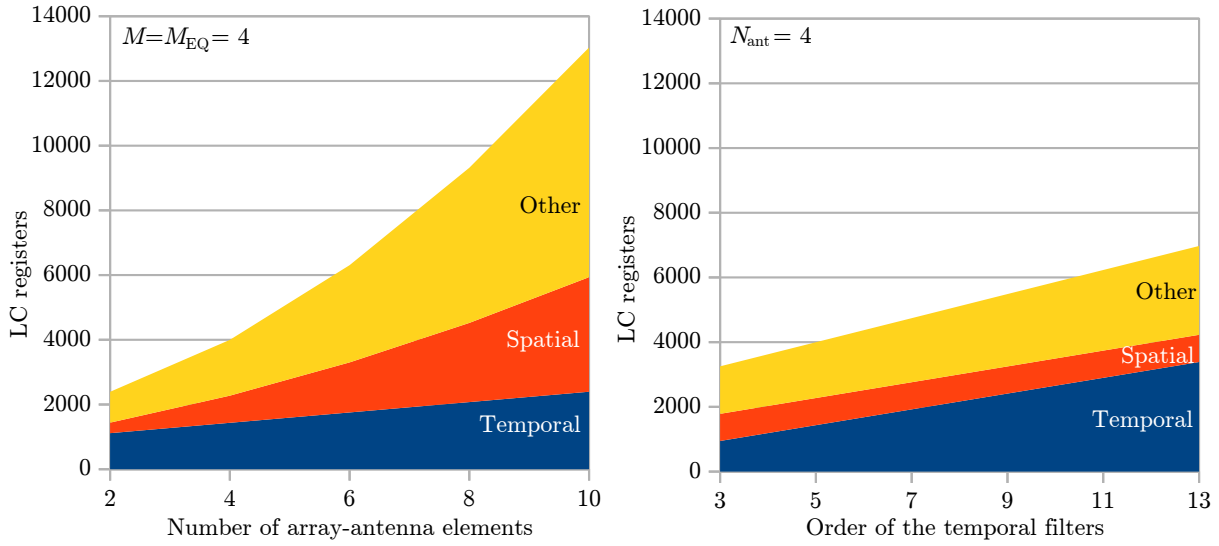
Adopting the input word length $n_x = 14$ bit and the coefficient word lengths $n_{\text{SF}} = n_{\text{NF}} = n_{\text{EQ}} = 16$ bit used in [70], the VHDL model of the filter was synthesized for an Altera Cyclone V FPGA (5CSEMA4U23C6) [43]. In Figure 5.4, the resulting total number of LCs used for combinational logic, and their distribution to the spatial and temporal filter components are plotted. On the left plot, the order of the NFs and the EQs is kept constant ($M = M_{\text{EQ}} = 4$) and the number of antenna elements is varied. While the number of LCs required by the temporal filter components grows linearly with the number of antenna elements, the number of LCs required by the spatial filter components grows quadratically. In case of five antennas, temporal and spatial filter components require approximately the same amount of LCs. This means that using the proposed spatial-temporal filter instead of the spatial-only filter in [71] doubles the hardware cost for interference mitigation. If the number of the antenna elements is higher than five, the hardware cost for spatial filtering dominates the hardware cost



(a) $M = M_{\mathrm{EQ}} = 4$, variable number of antenna-elements

(b) $N_{\mathrm{ant}} = 4$, variable number of taps

Figure 5.4: Number of combinational logic cells



(a) $M = M_{\mathrm{EQ}} = 4$, variable number of antenna-elements

(b) $N_{\mathrm{ant}} = 4$, variable number of taps

Figure 5.5: Number of logic cell registers

for temporal filtering. On the right plot in Figure 5.4, the number of antennas is kept constant ($N\text{ant} = 4$), and the order of the NFs and the EQs is changed concurrently. The number of the LCs required by the temporal filter components grows linearly with the order of the filters. When the filter order is three, the number of LCs required by the temporal filter components is approximately equal to the number of LCs required by the spatial filter components. If the filter order is higher, the hardware cost for temporal filtering dominates the hardware cost for spatial filtering. In Figure 5.5 the number of LCs used as registers is provided similar to Figure 5.4. The different scaling of the different figures is to be noted.

As stated before, the hardware cost of the computational blocks after re-quantization is lower than the ones before re-quantization. The LC requirement of the EQs is nearly one fourth of the NFs for the same filter order. Analogously, the LC requirement of the composition filter is one fourth of the decomposition filter.

5.5 Simulation Results

Functionality of the proposed filter as well as its VHDL implementation was verified using a Matlab/ModelSim based co-simulation. Matlab was used to generate synthetic signals for the simulation, to simulate the floating-point models of the different filters and to compute the filter coefficients. For the simulation of the fixed-point VHDL model, Matlab exports the synthetically generated signals into an external file and starts the ModelSim simulation. ModelSim reads the signals and exports the cross-correlation, the spatial covariance matrix, and the variances after simulating the filter for one observation time. After computing the new filter coefficients, Matlab exports the next portion of data and the new filter coefficients, which are read by ModelSim. ModelSim simulates the filter for the next observation time and so on. Continuity of the simulation is provided by the checkpoint/restore commands of ModelSim to save and restore the simulator state.

The single-antenna receiver (1-ant), the single-antenna receiver with temporal-only filtering (1-ant + tf), the 2x2-array-antenna receiver with spatial-only filtering (2x2-ant + sf), and with combined spatial-temporal filtering (2x2 ant sf + tf) using double-precision floating-point arithmetic were modeled and simulated using Matlab. The VHDL implementation of the spatial-temporal filter using fixed-point arithmetic (2x2 ant sf + tf (vhdl)) was simulated using ModelSim. The element spacing of the array-antenna is $\lambda/2$. Antenna-signals are down-converted to baseband and sampled at a rate of 2.047 MHz prior to interference mitigation. The NFs and the EQs have an

order of $M = M_{\text{EQ}} = 4$ with a tap-spacing of 5 samples. Observation time K is $2^{11} = 2048$ samples. The SNR of the received satellite signal prior to correlation is -16 dB. The weighting vector $\mathbf{w}_{\text{post}}$ from (4.17) is applied at post-correlation stage to form a beam towards the satellite.

The different interference mitigation filters are simulated for a scenario with up to five interferers. Directions of the different signal sources are given in the skyplot in Figure 5.6 (right). Starting only with the satellite signal, an interferer signal is turned on after each 100 ms. All interferers have an interference-to-signal ratio (ISR) of 35 dB. Interferers 1, 3, and 5 radiate CW signals with distinguishable frequencies; interferers 2 and 4 radiate wideband signals. The interferers are turned off at the time 700 ms. In Figure 5.6 (left), the estimated SNIR after correlation and the errors in the code and carrier tracking loops are plotted.

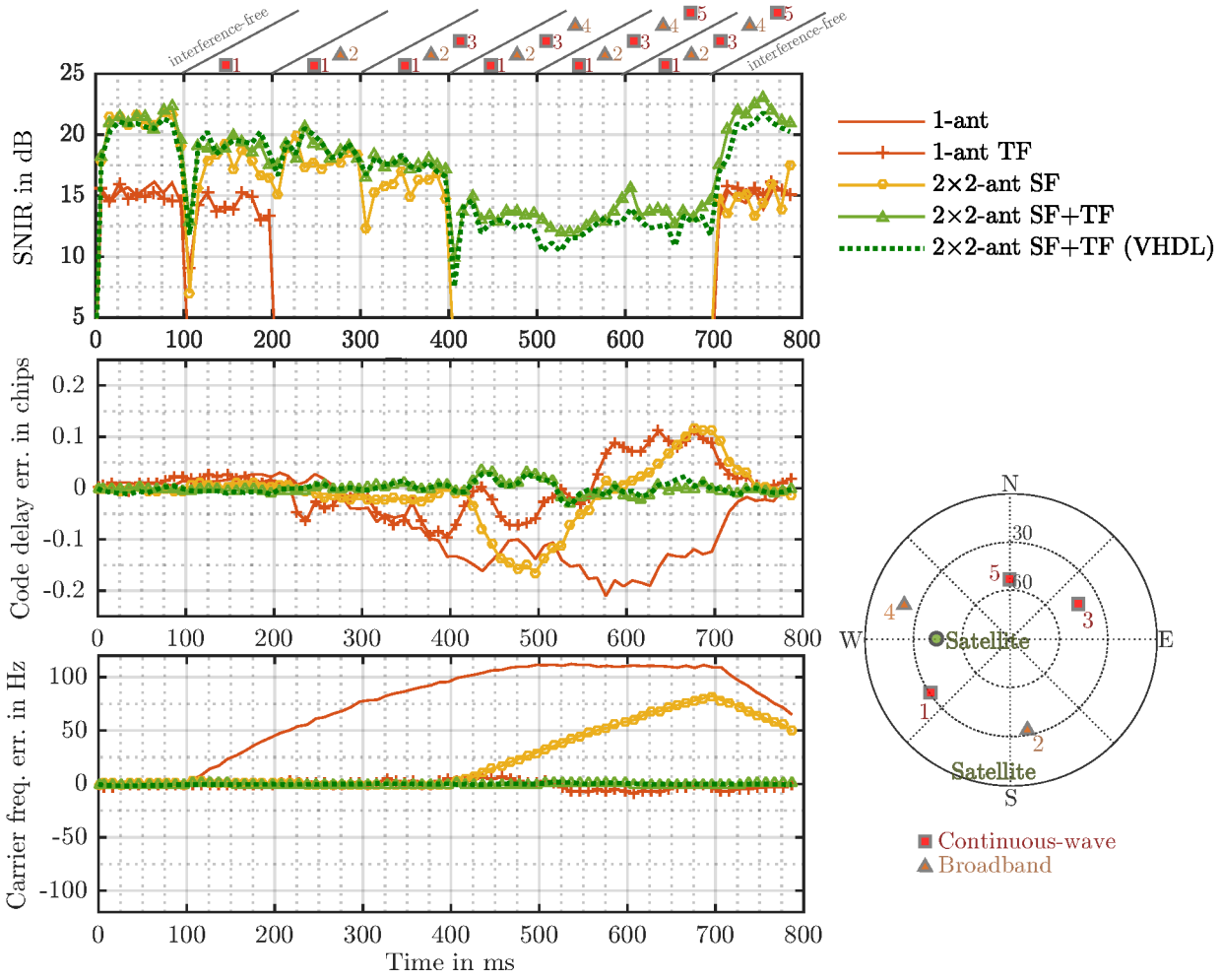
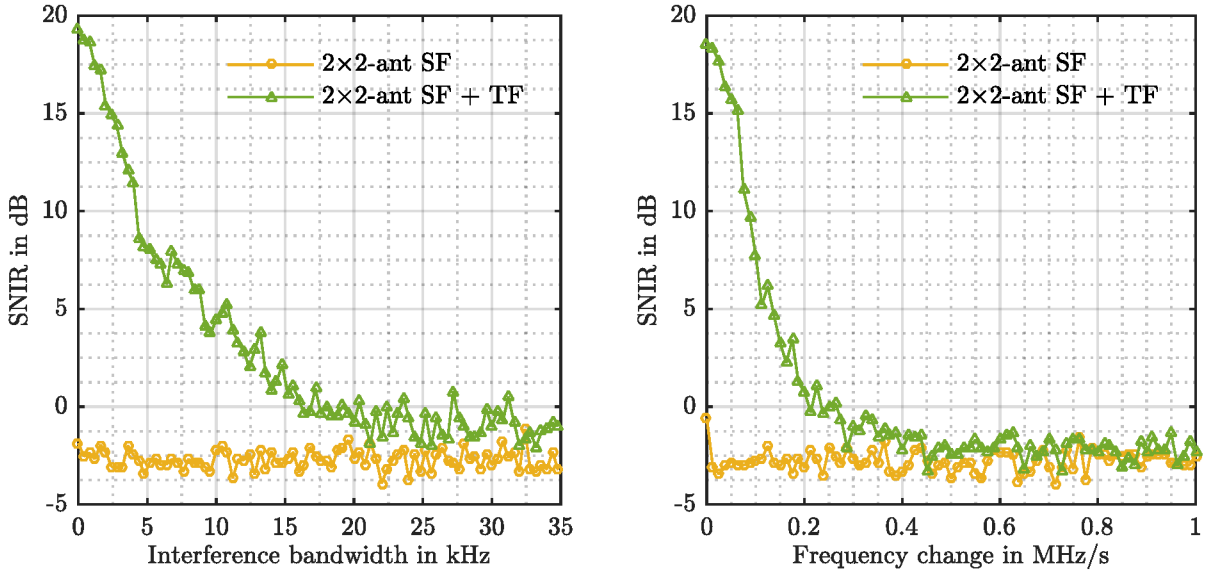


Figure 5.6: Simulation results

In the beginning, the 6 dB difference between the single antenna receivers and antenna-array receivers is caused by the beamforming after correlation. The single-

antenna receiver w/o interference protection looses track of the satellite immediately after the first interferer is turned on. All other receivers are able to mitigate the first interferer signal, which radiates a CW signal. The second interferer is a broadband interferer. The single-antenna receiver with temporal-only filtering fails to track the satellite signal, after this broadband interferer is turned on. The spatial-only filter is capable of mitigating up to three interferers (regardless of their signal character). If a fourth interferer appears, the spatial degrees of freedom are exceeded. Only the receiver with the combined spatial-temporal filter can finish the simulation without losing the satellite signal. The fixed-point VHDL model of the combined filter shows practically the same performance as the double-precision floating-point model simulated in Matlab.



(a) SNIR vs. interference bandwidth

(b) SNIR vs. frequency change rate

Figure 5.7: SNIR for various interferer bandwidths and rates of frequency change

In a further simulation, the corner case that an interferer radiates from the same direction as the satellite is examined. Figure 5.7 shows the resulting SNIR values. The spatial-only filter is incapable of suppressing the interferer signal w/o loosing the satellite signal in this case. The plot on the left side shows the estimate of the post-correlation SNIR over the interferer bandwidth. While a CW-signal is perfectly mitigated by the temporal filter, the filter performance decreases for growing interferer bandwidths. The plot on the right side shows the SNIR for the case that the frequency of the interferer changes over time. Such a signal occurs, for example, if a CW-interferer accelerates relative to the receiver. Similar to the behavior for growing bandwidths, the SNIR is lower for faster frequency changes.

The proposed STAP filter was evaluated based on real data provided by the German

Aerospace Center (DLR). The data was recorded as part of the project SAMURAI [42] at the GATE Testing Area in Berchtesgaden using the GALANT array-antenna demonstrator [100]. Figure 5.8 shows the resulting SNIR averaged over all visible satellites for the different filter concepts. Five interferers are in the vicinity of the receiver. While

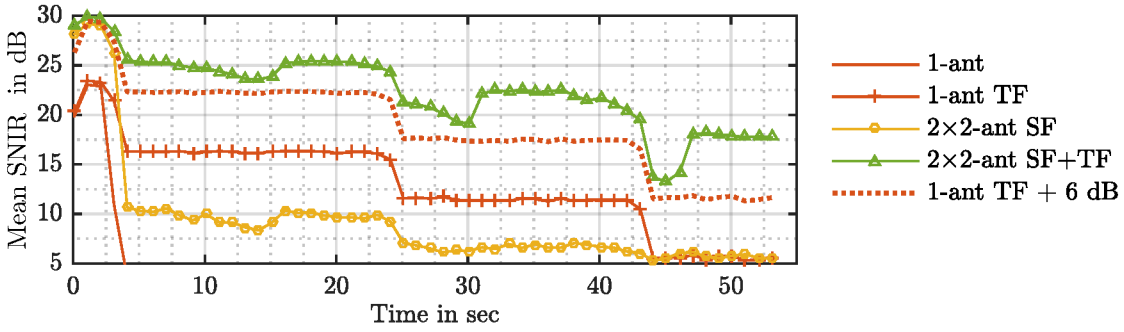


Figure 5.8: Post-processing results

one of these interferers radiates a broadband signal in the L1-band, the remaining are narrowband. The powers of the different interferers are gradually increased at nearly 20 second intervals, all at the same time. The interferers are first turned on at the third second of the record. The INR is 17.7 dB during the next 20 seconds and (21.3 dB and 26.2 dB in the following 20 s intervals).

The single-antenna receiver w/o any filtering immediately looses all satellites, when interferers are turned on. The spatial-only filter (with four degrees of freedom) is also overstrained by the presence of five interferers. The single-antenna receiver with temporal-only filtering can cope with the narrowband interferers. The remaining broadband interference "survives" the temporal processing and causes an SNIR loss. Overall, the combined spatio-temporal filter yields higher SNIR values compared to all other filter variants. The SNIR gain of the combined filter over the single-antenna receiver using temporal-only filtering is greater than 6 dB. (6 dB is the expected SNR gain provided by four antenna-elements in the interference-free case.)

5.6 Comparison to Joint Filter Approach

The decoupled STAP approach (as presented so far) does not exploit the full potential of the signal space spanned by the entire temporal and spatial degrees of freedom. By separating the temporal degrees of freedom from the spatial ones and using the same filter coefficients for all NFs, the decoupled spatial-temporal filter restricts the choice of the filter coefficients to a subset of all possible solutions.

For instance, if the filter suppresses a CW interference, the corresponding frequency is removed by the NFs prior to the spatial filter stage. Entire spatial domain, i.e. all signal directions, are affected by the temporal filter stage. The decoupled approach is not capable of selectively suppressing the interference frequency in the direction of the interference. This requires a joint spatial-temporal processing. This is, however, computationally more complex compared to the decoupled approach. In this section, a brief comparison of the decoupled and the joint approach will be provided by means of a simulation.

The input vector $\check{\mathbf{x}}(k)$ of the joint spatial-temporal filter is defined as

$$\check{\mathbf{x}}(k) = \begin{bmatrix} \mathbf{x}(k) \\ \mathbf{x}(k-1) \\ \vdots \\ \mathbf{x}(k-M+1) \end{bmatrix}$$

and contains all signal taps from all array elements. $\mathbf{x}(k)$ is the array output at time $k \cdot T_\mathrm{s}$ as defined in (3.4). Analogous to the spatial-only filter in Figure 4.8, the spatio-temporal interference mitigation before re-quantization is

$$\check{\mathbf{y}} = \check{\mathbf{P}} \cdot \check{\mathbf{x}},$$

where

$$\mathbf{R}_{\check{\mathbf{x}}\check{\mathbf{x}}} = \mathrm{E}\{\check{\mathbf{x}} \cdot \check{\mathbf{x}}^\mathrm{H}\}$$

is the spatio-temporal covariance matrix of the input vector $\check{\mathbf{x}}$, and $\check{\mathbf{P}}$ is the first N_ant rows of $\mathbf{R}_{\check{\mathbf{x}}\check{\mathbf{x}}}^{-1/2}$. As discussed in Section 5.2, a tap-spacing greater than $2\times$code-chip-duration should be used to avoid a distortion of the correlation function, that results from an overlap of the "echo-triangles" with the main correlation triangle.

The spatio-temporal covariance matrix $\mathbf{R}_{\check{\mathbf{x}}\check{\mathbf{x}}}$ has a relatively larger number of elements compared to the spatial-only covariance matrix $\mathbf{R}_{\mathbf{xx}}$ ($M^2 N_\mathrm{ant}^2$ vs. N_ant^2). Thus, the complexity of computing the coefficients of the joint filter (e.g. based on the EVD of $\mathbf{R}_{\check{\mathbf{x}}\check{\mathbf{x}}}$) is significantly higher than computing the spatial and temporal filter coefficients in a decoupled sense (based on the two separate covariance matrices with smaller dimensions). Furthermore, application of the joint filter in hardware is also an expensive task compared to the decoupled application of the NFs and the spatial decomposition in Figure 5.3. The first requires $M N_\mathrm{ant}^2$ complex multiplications, whereas the second requires $M N_\mathrm{ant}$ complex multiplications for the NFs and N_ant^2 for the decomposition filter. If, for example, $N_\mathrm{ant} = 4$ array elements and $M = 5$ taps are employed, using the joint filter in place of the decoupled filter doubles the number of the multiplications.

The following performance comparison is based on a Monte Carlo simulation. The satellite signal in the simulation has a C/N_0 of 42.7 dB/Hz. The interference signals have a random INR between 10 dB and 40 dB. The signal directions are random (elevation > 15°). Starting with the interference-free reception, an additional interferer is turned on after each 100 ms. First, third, and fifth interferers are CW signals with a frequency between $f_{\mathrm{L1}} - 1$ MHz and $f_{\mathrm{L1}} + 1$ MHz. Second and fourth interferers are wide-band signals. At time 0.6 s, all interferers are turned off again. The powers and the directions of the signals vary between different experiments. Thousand experiments were simulated. The average SNIR for different filter approaches are presented in Figure 5.9.

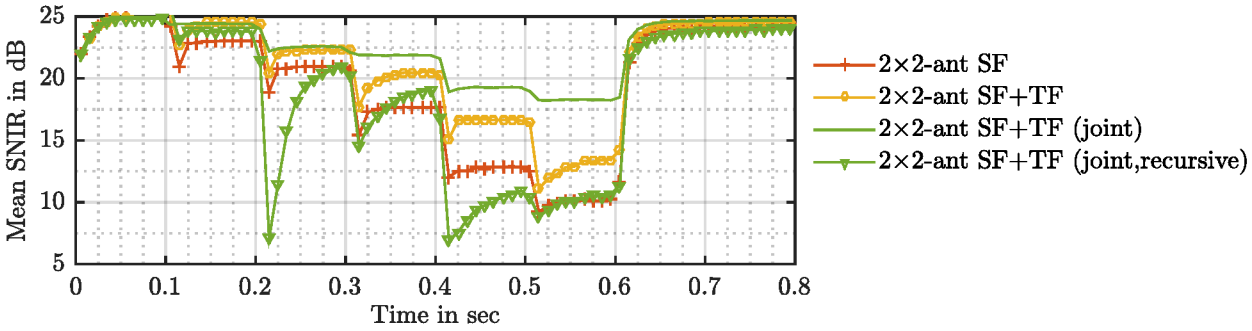


Figure 5.9: Simulation results comparing decoupled and joint spatial-temporal filters

A recursive implementation of the joint filter approach was also considered in the simulations. The recursive implementation is based on the Multidimensional Power Minimization (MPM) method, the use of which was presented in Section 4.3.2. Here, N_{ant} single-output PM filters are employed again for interference mitigation before correlation, each of which takes a different array element's latest output $x_i(k)$ as its reference signal. By combining all other taps $x_i(k-m)$, the PM filter attempts to generate a copy of the reference signal and subtracts the copy signal from the reference. The restriction (4.9) for the step-size parameter should be met to guarantee the convergence of the algorithm. Here, the filter coefficients are updated with a rate of 1 kHz.

The decoupled and the joint approaches yield similar SNIR values during the first two interference intervals. After a third interferer appears, their SNIR values are different. The difference is most obvious in the case of five interferers (0.5 s-0.6 s), i.e. the SNIR of the decoupled filter is 5 dB lower relative to the joint filter. In general, spatial-temporal filtering is more effective against interference compared to the spatial-only filtering apart from the recursive implementation of the joint filter. The recursive implementation has a relatively slow convergence speed due to the increased dimension of the signal space. Furthermore, it may converge to sub-optimum solutions and be

even less effective than spatial-only filter, as it is the case in the presence of four interferers in Figure 5.9 (0.4 s - 0.5 s).

To conclude, the joint filter requires a significantly higher computing power compared to the decoupled approach. Its recursive implementation is also problematic because of the slow convergence speed, which is caused by the increased dimension of the signal space. Although the joint filter yields better SNIR values in steady state, the decoupled filter provides a reasonable trade-off between the computational complexity and the interference suppression capability.

Chapter 6

Conclusion

The main aim of this thesis was to find an easy-to-implement, low-complexity, and efficient solution for interference and multipath mitigation in an array-antenna receiver. For this purpose, the Minimum Mean-Square Error Beamformer (MMSE) was chosen to be the starting point for further optimizations and algorithmic improvements. The argument for this choice was the blind character of the MMSE. "Blind" means in this context that this beamformer does not require any knowledge about the antenna geometry, the signal directions, or any kind of calibration, which makes it relatively simple compared e.g. to the Minimum Variance Distortionless Beamformer (MVDR) or parametric methods.

In the first place, the thesis asked the question where in the signal processing chain to execute beamforming. Since beamforming and correlation are linear operations, their execution order does not make a difference, if the computations could be realized with an infinite precision. However, in case of a digital implementation, the order and the chosen word lengths are directly linked with the implementation cost of the baseband signal processing. Thus, the thesis thoroughly studied the effect of quantization on the resulting SNIR. The outcome of this analysis was two formulas that can serve as a general rule-of-thumb for the choice of the word lengths in a beamformer. The next step was the estimation of the computational cost and the memory requirements of the digital beamforming by taking quantization into account. We assumed a word length of 14 bit for the input signal, a coefficient word length of 16 bit and a word length of 2 bit for the interference-free signal. The comparison proved an MMSE-based 2-step approach to be the most resource efficient option.

First step of the proposed 2-step beamformer is the pre-correlation interference mitigation filter. This is an adaptive pre-whitening filter, whose coefficients are computed based on the EVD of the covariance matrix of the input signal. While computation

of the covariance matrix and the filtering of the signal is realized in dedicated digital hardware, the EVD is computed in software by means of the Jacobi-Algorithm. In particular, the thesis presented a recursive form of this pre-whitening filter. For a minor loss in the dynamic performance, the recursive form of the filter offers significant resource savings both in hardware and in software in comparison to the non-recursive implementation. Besides reducing the hardware cost by 18%, the main benefit is the drastically reduced number of Givens-rotations, that are required by the Jacobi-Algorithm to compute the EVD. Furthermore, the recursive filter shows an improved mitigation performance in case of pulsed jamming.

Second step of the proposed 2-step beamformer is the post-correlation multipath mitigation filter. The thesis presented a revised version of the MMSE to achieve an improved multipath rejection at this stage. This beamformer (the MMSCE) can be seen as the counter part of an equalizer in the spatial domain. Overall, it achieves the best multipath mitigation performance in comparison to the deterministic beamformer, MVDR, and the conventional MMSE. While the deterministic and the MVDR (which are equivalent in the interference-free case) form a beam towards the satellite signal ignoring multipath, the conventional MMSE tends to constructively combine multipath and direct signal in order to maximize the signal power. In contrast, the MMSCE forms a beam towards the satellite while purposefully suppressing multipath signals. The thesis also showed the potential of using the VTL in combination with beamforming in order to overcome signal outages caused by interference mitigation.

In the final chapter, the 2-step beamformer from the previous chapter was combined with a bank of Notch Filters (NFs) to form a spatial-temporal filter. A bank of equalizers are employed at the output of the filter to compensate the signal distortions caused by the NFs. The presented filter belongs to the category of decoupled Space-Time Adaptive Processing (STAP), i.e. the temporal and spatial filter coefficients of the filter are computed separately. The thesis demonstrated the performance improvement of STAP relative to the spatial-only filtering by means of simulations using synthetic as well as real data. The benefit of STAP became clear especially in scenarios with a high number of interferers, if the interference signals are partly narrow-band and can, thus, be suppressed in the temporal domain. On the other hand, the disadvantage of STAP is its relatively higher resource requirement. In case of a 4-element antenna, for example, the temporal filter components dominate the hardware cost already for filter orders greater than 3. The question, whether this is a justified cost, can only be answered by extensive monitoring of the GNSS bands, assessment of the present interference situation and definition of realistic scenarios.

To sum up, the thesis provides an overview of a wide range of spatial processing

techniques for array-antenna receivers and differentiates from previous work by carefully considering the implementation aspects. The thesis proposes a novel adaptive spatial processing approach for array-antenna receivers. All things considered, it is safe to say, that the presented approach is a very powerful and cost-efficient method against interference and multipath, which can be implemented on currently available digital hardware platforms.

Appendix A

Tracking

In a GNSS receiver, the PVT is computed based on the travel times of the satellite signals from the satellites to the receiver and the Doppler frequencies of the different satellite signals. The travel time and the Doppler frequency can directly be derived from the code phase and carrier frequency of the received satellite signal. In order to determine these signal parameters, the receiver generates local replicas of the satellite signals, correlates them with the received signal in the baseband and tries to synchronize the local replicas with the received satellite signals. This process of synchronization is called signal *tracking*. While correlation is typically computed in dedicated hardware as described in Section 3.3, control of the correlation channels, i.e. tracking, is carried out in software.

Conventionally, tracking is realized by scalar control loops, that adjust the signal parameters separately for each satellite channel. Although there is also a direct link between the signal parameters and the satellite's and the receiver's positions and velocities, this relation is not used in the scalar tracking loops. As an alternative to the scalar loops, the VTL combine the two tasks of tracking and PVT computation into one overall algorithm. They compute the control values for the correlation channels based on a universal signal reception model, that describes the relationship between the signal parameters of all satellites and the positions and velocities of the satellites and the receiver.

The following two sections give a brief summary of the conventional tracking loops and the VTL.

A.1 Conventional Tracking Loops

Conventionally, the code delay and the carrier frequency of the satellite signal are tracked in separate scalar loops, the Delay-Locked Loop (DLL) and the Frequency-Locked Loop (FLL). Coherent code tracking requires the use of a Phase-Locked Loop (PLL) in addition. For the sake of simplicity, however, this and the following sections present incoherent code tracking.

The general structure of a scalar tracking loop is shown in Figure A.1 .

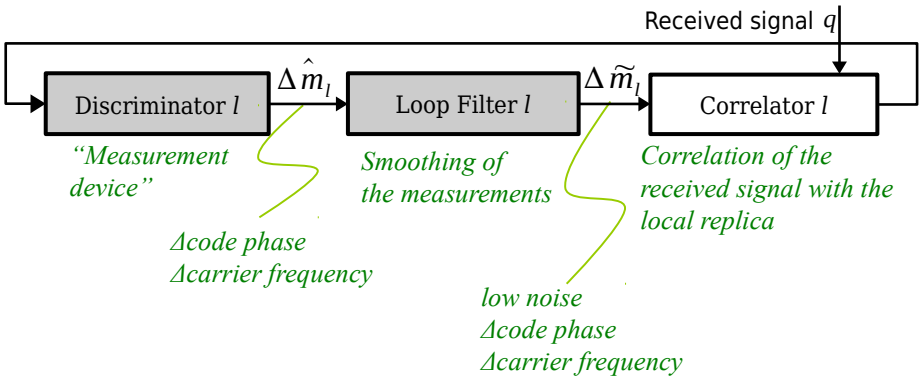


Figure A.1: Conventional tracking loop

The discriminators estimate the variance of the local signal replica's code delay $\hat{\tau}$ from the received satellite signal's code delay τ, as well as the variance of the locally generated carrier frequency $\hat{f}$ from the carrier frequency f of the received signal ($\Delta\tau = \tau - \hat{\tau}$, $\Delta f = f - \hat{f}$). The discriminators are based on discrete values of the correlation function:

$$\begin{aligned} \text{“very early”} \quad & \mathcal{E}_v \quad = \varphi_{\hat{s}q}(-2 \cdot \delta\tau) \\ \text{“early”} \quad & \mathcal{E} \quad = \varphi_{\hat{s}q}(-\delta\tau) \\ \text{“prompt”} \quad & \mathcal{P} \quad = \varphi_{\hat{s}q}(0) \\ \text{“late”} \quad & \mathcal{L} \quad = \varphi_{\hat{s}q}(+\delta\tau) \\ \text{“very late”} \quad & \mathcal{L}_v \quad = \varphi_{\hat{s}q}(+2 \cdot \delta\tau) \end{aligned}$$

The *Early-minus-Late* discriminator (here in its incoherent form)

$$\Delta\hat{\tau}_{\mathrm{EL}} = (1 - \frac{\delta\tau}{T_{\mathrm{c}}}) \cdot \frac{|\mathcal{E}| - |\mathcal{L}|}{|\mathcal{E}| + |\mathcal{L}|} \cdot T_{\mathrm{c}},$$

where T_{c} is the the code duration, is the most commonly used estimator in the DLL to estimate $\Delta\tau$. The variance at the output of this estimator is (if the so-called “squaring loss” is neglected)

$$\sigma^2_{\tau,\mathrm{EL}} = \mathrm{E}\{|\Delta\hat{\tau}_{\mathrm{EL}}|^2\} \approx \frac{\delta\tau \cdot T_{\mathrm{c}}}{\mathrm{SNR}}, \tag{A.1}$$

where

$$\text{SNR} = \frac{\mathrm{E}\{\mathcal{P}\}}{\mathrm{E}\{|\mathcal{P} - \mathrm{E}\{\mathcal{P}\}|^2\}} = \frac{1}{T \cdot C/N_0}$$

is the signal-to-noise ratio after correlation. C/N_0 is the signal-to-noise-density ratio of the satellite signal.

The double-delta-correlator ($\Delta\Delta$-correlator) computes five correlation values in order to estimate $\Delta\tau$

$$\Delta\hat{\tau}_{\Delta\Delta} = \frac{\mathcal{E} - \mathcal{L} - (\mathcal{E}_v - \mathcal{L}_v)/2}{\mathcal{P}}$$

based on these five correlation values. The $\Delta\Delta$-correlator is immune against reflected signals with relative code delays greater than $2 \cdot \delta\tau$. This is true only if the satellite signal is received with an unlimited front-end bandwidth, so that the correlation function is an ideal correlation triangle. Reducing the front-end bandwidth flattens the correlation triangle and there is no use in reducing the correlator spacing to less than the spreading code rate divided by the front-end bandwidth [3, 101]. Decreasing the correlator spacing below this limit will only decrease the linear range of the discriminator [102].The variance at the output of the $\Delta\Delta$-correlator is

$$\sigma^2_{\tau,\Delta\Delta} = \mathrm{E}\{|\Delta\hat{\tau}_{\Delta\Delta}|^2\} \approx 2 \cdot \frac{\delta\tau \cdot T_\mathrm{c}}{\text{SNR}}. \tag{A.2}$$

In the FLL, e.g. the *Cross*-discriminator

$$\Delta\hat{f} = \frac{1}{2\pi T} \cdot \frac{\mathfrak{Re}\{\mathcal{P}_{-1}\} \cdot \mathfrak{Im}\{\mathcal{P}\} - \mathfrak{Re}\{\mathcal{P}\} \cdot \mathfrak{Im}\{\mathcal{P}_{-1}\}}{|\mathcal{P}_{-1}| \cdot |\mathcal{P}|}$$

can be used to estimate Δf, where $\mathcal{P}_{-1}$ is the output of the "prompt"-correlator from the previous observation period. The variance of this discriminator can approximated as [2]

$$\sigma^2_f = \mathrm{E}\left\{\left|\Delta\hat{f}\right|^2\right\} \approx \frac{1}{\text{SNR}} \cdot \left(1 + \frac{1}{2 \cdot \text{SNR}}\right) \cdot \frac{1}{(2\pi T)^2}. \tag{A.3}$$

The loop filter in Figure A.1 is used to reduce the measurement noise. In the simplest case, a filter of the first order is applied, which multiplies the measured value $\Delta m = \Delta\hat{\tau}$ of the discriminator with a factor $0 < \omega_0 T < 1$

$$\Delta\tilde{m} = \omega_0 T \Delta m, \tag{A.4}$$

where T is the observation time from (3.5). The equivalent noise bandwidth of this loop filter is $B_n = \omega_0/4$. The bandwidth B_n is a design parameter, that must be chosen as

small as possible to suppress the measurement noise. At the same time, the bandwidth of the filter must be broad enough to cope with the dynamics of the signal parameters (that result from the satellite and user movements and the drift of the user clock).

In practice, the code phase of the local signal replica is not directly controlled by the tracking loops but indirectly via the chip rate f_c.That means that instead of directly changing the code phase by $\Delta\tilde{\tau}$, the chip rate is increased by $\Delta\tilde{f}_c = \Delta\tilde{\tau}/T$ for the next integration period. This way, the local code generator is accelerated (or slowed down) during the next integration period T , in order to catch up the detected delay in the code phase of the local signal relative to the received satellite signal.

Carrier Aiding There is a proportional relation $f_{c,D}/f_{c,0} = f_D/f_0$ between the Doppler shift $f_{c,D}$ of the chip rate and f_D of the carrier frequency, where $f_{c,0}$ and f_0 are the chip rate and the carrier frequency transmitted by the receiver. Because the carrier frequency tracking is by orders of magnitude less noisy than the code tracking, it makes sense to derive the Doppler shift of the code signal from the estimated carrier frequency $\hat{f}$ and consider this value in the code tracking loop [3]. For the estimation of the chip rate, this means

$$\hat{f}_c = f_{c,0} \cdot \left(1 + \frac{\hat{f} - f_{IF}}{f_0}\right) + \Delta\tilde{f}_c, \tag{A.5}$$

where f_{IF} is the intermediate frequency.

A.2 Vektor Tracking Loops

In contrast to the conventionally used scalar loops, the VTL combine the signal parameters from all satellites, the satellite positions, the user positions, and their velocities into a universal reception model. They jointly process all discriminator outputs and jointly control all signal parameters of all visible satellites. The principle is illustrated in Figure A.2.

The VTL have i.a. the following advantages (+) and disadvantages (−) [103]:

+ The VTL are able to track a satellite signal even in case of a total signal outage, as they are able to estimate the signal parameters based on the visible satellites. This way they overcome not only shadowing effects but also a short-term spatial nulling towards a satellite due to interference mitigation (see Section 4.4).

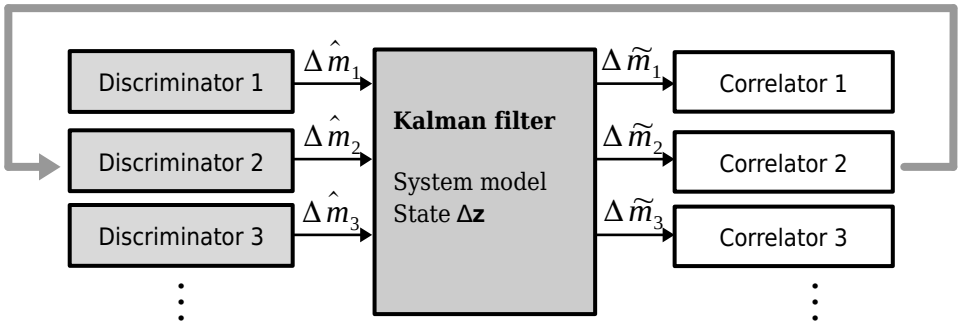


Figure A.2: Vector tracking loops (VTL)

+ The VTL can in general track satellites with lower signal to noise density ratios C/N_0.

+ The VTL can be designed to cope with the same dynamics as the scalar loops but produce less noise at the filter output. This again leads to less noisy PVT estimates.

– The VTL require significantly higher computing power than the scalar loops.

– Errors in a satellite channel may affect all channels, that are controlled by the VTL. An undetected larger error may cause instability in the filter, which may lead the VTL to loose track of all satellite signals.

The loop filter used in the VTL is an extended Kalman filter, that jointly processes all measurements $\Delta\tau^{(l)}$ and $\Delta f^{(l)}$. The measurements are merged to a measurement vector

$$\Delta\mathbf{m} = \left[\Delta\hat{\tau}^{(l)} \quad \dots \quad \Delta\hat{\tau}^{(l)} \quad \Delta\hat{f}^{(l)} \quad \dots \quad \Delta\hat{f}^{(l)}\right]^{\mathrm{T}}.$$

Internally, the filter estimates the change of the user position $\mathbf{x}$ of the user velocity $\mathbf{v}$, the clock bias δt ($b = c_0 \cdot \delta t$), and the clock drift $\delta\dot{t}$ ($\dot{b} = c_0 \cdot \delta\dot{t}$) (where c_0 is the speed of light). These estimates form the *state vector*

$$\Delta\mathbf{z} = \begin{bmatrix} \Delta\mathbf{x} \\ \Delta\mathbf{v} \\ \Delta b \\ \Delta\dot{b} \end{bmatrix}.$$

The non-linear observation equation $\Delta\mathbf{m} = h(\Delta\mathbf{z}) + \mathbf{n}$ defines the relationship between the state vector $\Delta\mathbf{z}$ and the measurement vector $\Delta\mathbf{m}$, where $\mathbf{n}$ is the measurement noise.

Below, the update procedure of the Kalman filter is described [104]:

1. Prediction of the state vector $\Delta\hat{\mathbf{z}}$ for the current time k based on the previous estimate $\Delta\hat{\mathbf{z}}_{k-1}^{+}$ of the state vector (*time update*):

$$\Delta\hat{\mathbf{z}}_{k}^{-} = \mathbf{\Phi} \cdot \Delta\hat{\mathbf{z}}_{k-1}^{+}. \tag{A.6}$$

The upper index $(-)$ indicates, that the current measurement $\Delta\mathbf{m}_k$ in (A.6) is not taken into account yet. The transition matrix $\mathbf{\Phi}$ defines the expected change in the state vector $\Delta\mathbf{z}$ after one update period T:

$$\mathbf{\Phi} = \begin{bmatrix} \mathbf{I}_{3\times3} & T\cdot\mathbf{I}_{3\times3} & \mathbf{0}_{3\times1} & \mathbf{0}_{3\times1} \\ \mathbf{0}_{3\times3} & \mathbf{I}_{3\times3} & \mathbf{0}_{3\times1} & \mathbf{0}_{3\times1} \\ \mathbf{0}_{1\times3} & \mathbf{0}_{1\times3} & 1 & T \\ \mathbf{0}_{1\times3} & \mathbf{0}_{1\times3} & 0 & 1 \end{bmatrix},$$

where $\mathbf{I}_{M\times M}$ is the unit matrix of size $M \times M$ and $\mathbf{0}_{M\times N}$ is the zero matrix of size $M \times N$.

With other words $\mathbf{\Phi}$, models the linear relationship between the user position and the user velocity

$$\Delta\mathbf{x}_k = \Delta\mathbf{x}_{k-1} + T \cdot \Delta\mathbf{v}_{k-1},$$

as well as the linear relationship between the clock offset and the clock drift

$$\Delta b_k = \Delta b_{k-1} + T \cdot \Delta\dot{b}_{k-1}.$$

2. Prediction of the *error covariance matrix*

$$\mathbf{P} = E\{(\mathbf{z} - \hat{\mathbf{z}}) \cdot (\mathbf{z} - \hat{\mathbf{z}})^{\mathrm{T}}\}$$

for the current time k based on the previous estimate $\mathbf{P}_{k-1}^{+}$ (*time update*):

$$\mathbf{P}_{k}^{-} = \mathbf{\Phi} \cdot \mathbf{P}_{k-1}^{+} \cdot \mathbf{\Phi}^{\mathrm{T}} + \mathbf{Q}$$

$\mathbf{Q}$ is the *system covariance matrix* and stands for the system noise. It models the errors in the estimated states and their growth over time due to the noise sources in the system. The noise sources in the system are e.g. unmodeled dynamics as well as errors of the measurement devices. Generally, $\mathbf{Q}$ is diagonal and constant.

3. Computation of the covariance matrix

$$\mathbf{R} = \mathrm{E}\{\mathbf{n} \cdot \mathbf{n}^{\mathrm{T}}\}$$

of the measurement noise. $\mathbf{R}$ is also a diagonal matrix and consists of the variances of the different discriminators. These variances can be derived from the SNR by the equations (A.1) and (A.3).

4. Computation of the *observation matrix* $\mathbf{H}$. The observation matrix results from the linearization of the observation equation:

$$h(\Delta\mathbf{z}) \approx \mathbf{H}_k \cdot \Delta\mathbf{z}$$

with

$$\mathbf{H} = \begin{bmatrix} \mathbf{h}_\tau^{(1)} \\ \vdots \\ \mathbf{h}_\tau^{(L)} \\ \mathbf{h}_f^{(1)} \\ \vdots \\ \mathbf{h}_f^{(L)} \end{bmatrix}.$$

Here,

$$\mathbf{h}_\tau^{(l)} = \frac{1}{T_c c_0} \begin{bmatrix} \mathbf{e}^{(l)\mathrm{T}} & \mathbf{0}_{1\times 3} & -1 & 0 \end{bmatrix}$$

is a row of $\mathbf{H}$, that translates a change in the state vector $\Delta\mathbf{z}$ to a change in the code phase $\Delta\tau^{(l)}$ of the l-th satellite. Analogously,

$$\mathbf{h}_f^{(l)} = \frac{f_0}{c_0} \begin{bmatrix} \mathbf{0}_{1\times 3} & \mathbf{e}^{(l)\mathrm{T}} & 0 & -1 \end{bmatrix}$$

is a row of $\mathbf{H}$, that translates a change in the state vector $\Delta\mathbf{z}$ to a change in the carrier frequency $\Delta f^{(l)}$ of the l-th satellite. $\mathbf{e}^{(l)}$ is the direction vector of unit length, that points from the user position to the l-th satellite.

5. Computation of the *Kalman matrix* $\mathbf{K}$:

$$\mathbf{K}_k = \mathbf{P}_k^- \cdot \mathbf{H}_k^{\mathrm{T}} \cdot (\mathbf{H}_k \cdot \mathbf{P}_k^- \cdot \mathbf{H}_k^{\mathrm{T}} + \mathbf{R}_k)^{-1}. \tag{A.7}$$

6. Correction of the state vector considering the latest measurements $\Delta\mathbf{m}_k$ (*measurement update*)

$$\Delta\hat{\mathbf{z}}_k^+ = \Delta\hat{\mathbf{z}}_k^- + \mathbf{K}_k \cdot \Delta\mathbf{m}_k,$$

where $\Delta\hat{\mathbf{z}}_k^-$ is computed by (A.6);
computation of the correction values for the signal parameters

$$\Delta\tilde{\mathbf{m}}_k = \mathbf{H}_k \cdot \mathbf{K}_k \cdot \Delta\mathbf{m}_k, \tag{A.8}$$

that are applied to the local replica generation in the next observation period. The Kalman matrix K is responsible for the proper weighting of the measurements depending on their "'quality"' (SNR).

7. Correction of the error covariance matrix considering the latest measurements (*measurement update*):

$$\hat{\mathbf{P}}_k^+ = \mathbf{P}_k^- - \mathbf{K}_k \cdot \mathbf{H}_k \cdot \mathbf{P}_k^-.$$

A real-time capable implementation of the Kalman filter based VTL on an embedded platform is presented in [105].

Appendix B

Position, Velocity, Time Computation

This appendix presents a conventional algorithm, that is used for computing the PVT of the receiver based on the measured travel times and the Doppler-frequencies of the received satellite signals. An efficient implementation of this algorithm in software using block floating point arithmetic is presented in [106]. In addition, [107] presents, how to apply interpolation to reduce the processing power required for the computation of the satellite positions and the atmospheric corrections.

The measured pseudorange $\rho^{(l)}$ of the l-th satellite is computed as the difference between the (uncorrected) transmission time $t - \tau^{(l)}$ and the reception time t:

$$\rho^{(l)} = c_0 \cdot (\text{reception time} - \text{transmission}) = c_0 \cdot \tau^{(l)},$$

where $\tau^{(l)}$ is the signal travel time and c_0 is the speed of light.

The expected pseudorange $\hat{\rho}^{(l)}$ for a known user position $\mathbf{x}$ and the user clock bias δt is given by

$$\hat{\rho}^{(l)}(\mathbf{x}, b) = \|\mathbf{x}^{(l)} - \mathbf{x}\| + b - c_0 \cdot \delta t^{(l)} + c_0 \cdot (\delta\tau_{\text{iono}}^{(l)} + \delta\tau_{\text{trop}}^{(l)}).$$

Here, $\mathbf{x}^{(l)} = \mathbf{x}^{(l)}(t - \tau^{(l)})$ is the position of the k-th satellite and $\delta t^{(l)} = \delta t^{(l)}(t - \tau^{(l)})$ is the offset of the satellite's clock at transmission time $t - \tau^{(l)}$. $\mathbf{x} = \mathbf{x}(t)$ is the user position and $b = c_0 \cdot \delta t$ with $\delta t = \delta t(t)$ is the offset of the user's clock at reception time t.

The objective of the PVT algorithm is to find an estimate $(\mathbf{x}, b)$ of the user position and time, which minimizes the mean square difference $\|\Delta\boldsymbol{\rho}(\mathbf{x}, b)\|^2$

$$\Delta\boldsymbol{\rho}(\mathbf{x}, b) = \begin{bmatrix} \Delta\rho^{(1)}(\mathbf{x}, b) \\ \vdots \\ \Delta\rho^{(K)}(\mathbf{x}, b) \end{bmatrix} = \begin{bmatrix} \hat{\rho}^{(1)}(\mathbf{x}, \delta t) - \rho^{(1)} \\ \vdots \\ \hat{\rho}^{(K)}(\mathbf{x}, \delta t) - \rho^{(K)} \end{bmatrix} \tag{B.1}$$

between expected and measured pseudoranges.

The solution can be found iteratively by means of the Newton's method

$$\begin{bmatrix} \mathbf{x}_{i+1} \\ b_{i+1} \end{bmatrix} = \begin{bmatrix} \mathbf{x}_i \\ b_i \end{bmatrix} + (\mathbf{G}^{\mathrm{T}} \cdot \mathbf{W} \cdot \mathbf{G})^{-1} \cdot \mathbf{G}^{\mathrm{T}} \cdot \mathbf{W} \cdot \Delta\boldsymbol{\rho}(\mathbf{x}_i, b_i).$$

$\mathbf{W}$ is, here, a diagonal weighting matrix, e.g. with the diagonal elements

$$w_{l,l} = \sin^2(\text{elevation of the } l\text{-th satellite}),$$

for taking the reduced quality of the satellite signals coming from lower elevations.

The matrix

$$\mathbf{G} = \begin{bmatrix} \mathbf{e}^{(1)^{\mathrm{T}}} & -1 \\ \vdots & \\ \mathbf{e}^{(K)^{\mathrm{T}}} & -1 \end{bmatrix}$$

is referred as the geometry matrix and contains the direction vectors

$$\mathbf{e}^{(l)} = \frac{\mathbf{x}^{(l)} - \mathbf{x}}{\|\mathbf{x}^{(l)} - \mathbf{x}\|},$$

pointing from the user position to the satellite positions.

The velocity $\mathbf{v}$ and clock drift $\delta\dot{t}$ of the receiver can be computed similarly.

The measured range rate

$$\dot{\rho}^{(l)} = c_0 \cdot \frac{-f_{\mathrm{D}}^{(l)}}{f_0} \tag{B.2}$$

is be computed from the Doppler shift $f_{\mathrm{D}}^{(l)}$ of the the carrier frequency.

Analogous to the position computation, the objective is to minimize the difference

$$\Delta\dot{\boldsymbol{\rho}}(\mathbf{v}, \dot{b}) = \begin{bmatrix} \Delta\dot{\rho}^{(1)}(\mathbf{x}, b) \\ \vdots \\ \Delta\dot{\rho}^{(K)}(\mathbf{x}, b) \end{bmatrix} = \begin{bmatrix} \hat{\dot{\rho}}^{(1)}(\mathbf{v}, \dot{b}) - \dot{\rho}^{(1)} \\ \vdots \\ \hat{\dot{\rho}}^{(K)}(\mathbf{v}, \dot{b}) - \dot{\rho}^{(K)} \end{bmatrix} \tag{B.3}$$

between the expected range-rates

$$\hat{\dot{\rho}}^{(l)}(\mathbf{v}, \dot{b}) = \mathbf{e}^{(l)^{\mathrm{T}}} \cdot \left(\mathbf{v}^{(l)} - \mathbf{v}\right) + \dot{b} \quad \text{mit } \dot{b} = c_0 \cdot \delta\dot{t}$$

and the measured range-rates from (B.2) [2].

The solution can be computed iteratively:

$$\begin{bmatrix} \mathbf{v}_{i+1} \\ \dot{b}_{i+1} \end{bmatrix} = \begin{bmatrix} \mathbf{v}_i \\ \dot{b}_i \end{bmatrix} + (\mathbf{G}^{\mathrm{T}} \cdot \mathbf{W} \cdot \mathbf{G})^{-1} \cdot \mathbf{G}^{\mathrm{T}} \cdot \mathbf{W} \cdot \Delta\dot{\boldsymbol{\rho}}(\mathbf{v}_i, \dot{b}_i).$$

Bibliography

[1] M. S. Braasch and V. Dierendonck, "Gps receiver architectures and measurements," in *Proceedings of the IEEE*, vol. 87, 1999.

[2] P. Misra and P. Enge, *Global Positioning System: Signals, Measurements, and Performance*. Ganga-Jamuna Press, 2006.

[3] E. Kaplan, J. Leva, and M. Pavloff, *Understanding GPS: Principles And Applications*. Artech House, Inc., 1996.

[4] K. Borre, D. M. Akos, N. Bertelsen, P. Rinder, and S. H. Jensen, *A Software-Defined GPS and GALILEO receiver*. Birkhäuser Boston, 2007.

[5] *Interface Control Document: Navstar GPS Space Segment/Navigation User Interfaces (ICD-GPS-200, IRN-200C-004)*, 2000.

[6] X. Luo, M. Mayer, B. Heck, and J. L. Awange, "A realistic and easy-to-implement weighting model for gps phase observations," *IEEE Transactions on Geoscience and Remote Sensing*, vol. 52, no. 10, Jan 2014.

[7] S. Pullen and G. X. Gao, "Gnss jamming in the name of privacy: Potential threat to gps aviation," *Inside GNSS*, Mar/Apr 2012.

[8] J. R. Clynch, A. A. Parker, R. W. Adler, W. R. Vincent, P. McGill, and G. Badger, "The hunt for rfi: Unjamming a coast harbor," *GPS World*, vol. 14, no. 1, Jan 2013.

[9] W. Dunkel, O. Weber, and F. Butsch, "Gnss interference detection with gimos," in *11th International GBAS Working Group Meeting (I-GWG-11)*, 2011.

[10] R. Bauernfeind, T. Kraus, D. Doetterboeck, B. Eissfeller, E. Loehnert, and E. Wittmann, "Car jammers: Interference analysis," *GPS World*, Oct 2011.

[11] R. H. Mitch, R. C. Dougherty, M. L. Psiaki, S. P. Powell, B. W. O'Hanlon, J. A. Bhatti, and T. E. Humphreys, "Know your enemy: Signal characteristics of civil gps jammers," *GPS World*, vol. 23, no. 1, 2012.

[12] R. Bauernfeind, I. Kraemer, H. Beckmann, B. Eissfeller, and V. Vierroth, "In-car jammer interference detection in automotive gnss receivers and localization by means of vehicular communication," in *IEEE Forum on Integrated and Sustainable Transportation Systems*, Jun/Jul 2011.

[13] J. Warburton and C. Tedeschi, "Gps privacy jammers and rfi at newark," in *12th International GBAS Working Group Meeting (I-GWG-12)*, 2012.

[14] J. Grabowski, "Field observations of personal privacy devices," in *Proceedings of ION ITM*, 2012.

[15] C.-C. Sun and S.-S. Jan, "Interference characteristics for the civil airport environment using time-frequency analysis," in *Position Location and Navigation Symposium (PLANS)*, 2012.

[16] Z. Shengkang, W. Hongbo, Y. Jun, and H. Leiming, "Gps short-delay multipath estimation and mitigation based on least square method," *Journal of Systems Engineering and Electronics*, vol. 20, no. 5, 2009 2009.

[17] B. R. Rao, J. H. Williams, E. N. Rosario, and R. J. Davis, "Gps microstrip antenna array on a resistivity tapered ground plane for multipath mitigation," The MITRE Corporation, Tech. Rep., 2000.

[18] M. Brenner, R. Reuter, and B. Schipper, "Gps landing system multipath evaluation techniques and results," in *Proceedings of the 11th International Technical Meeting of the Satellite Division of The Institute of Navigation (ION GPS)*, Sep 1998.

[19] A. Jahn, H. Bischl, and G. Heiss, "Channel characterisation for spread spectrum satellite communications," in *IEEE 4th International Symposium on Spread Spectrum Techniques and Applications*, Sep 1996.

[20] J. L. Vicario, F. Antreich, M. Barcelo, N. Basta, J. Cebrian, M. Cuntz, O. Gago, L. Gonzales, V. Heckler, C. Lavin, M. M. nosas, J. Picanyol, G. Seco-Granados, M. Sgammini, and F. Amarillo, "Adibeam: Adaptive digital beamforming for galileo reference ground stations," in *Proceedings of the 23rd International Technical Meeting of The Satellite Division of the Institute of Navigation (ION GNSS)*, Sep 2010.

[21] M. C. Bailey, "A broad-beam circularly-polarized antenna," in *Antennas and Propagation Society International Symposium*, vol. 15, Jun 1977.

[22] J. H. Williams, R. J. Davis, and E. N. Rosario, "Multipath mitigation performance of planar gps adaptive antenna arrays for precision landing ground stations," in

Proceedings of the 13th International Technical Meeting of the Satellite Division of The Institute of Navigation (ION GPS), Sep 2000.

[23] J. M. Tranquilla, J. P. Carr, and H. M. Al-Rizzo, "Analysis of a choke ring groundplane for multipath control in global positioning system (gps) applications," *IEEE Transactions on Antennas and Propagation*, vol. 42, no. 7, Jul 1994.

[24] C. C. Counselman, "Multipath-rejecting gps antennas," *Proceedings of the IEEE*, vol. 87, no. 1, Jan 1999.

[25] M. V. T. Heckler, W. Elmarissi, L. A. Greda, M. Cuntz, and A. Dreher, "Narrowband microstrip antenna array for a robust receiver for navigation applications," in *3rd European Conference on Antennas and Propagation*, Mar 2009.

[26] A. Konovaltsev, M. Cuntz, L. A. Greda, M. V. T. Heckler, and M. Meurer, "Antenna and rf front end calibration in a gnss array receiver," in *IEEE International Microwave Workshop Series on RF Front-ends for Software Defined and Cognitive Radio Solutions (IMWS)*, Feb 2010.

[27] O. C. Dabak, F. Erdem, T. Sonmez, L. Alatan, and S. S. Koc, "Interference suppression in a gps receiver with 4 element array design and implementation of beamforming algorithms," in *IEEE/ION Position, Location and Navigation Symposium (PLANS)*, Apr 2016.

[28] N. Basta, A. Dreher, S. Caizzone, M. Sgammini, F. Antreich, G. Kappen, S. Irteza, R. Stephan, M. A. Hein, E. Schäfer, A. Richter, M. A. Khan, L. Kurz, and T. G. Noll, "System concept of a compact multi-antenna gnss receiver," in *The 7th German Microwave Conference*, 2012.

[29] L. Guo, P.-K. Tan, and T.-H. Chio, "A compact 8-element antenna array for gps digital beamforming," in *International Symposium on Antennas and Propagation (ISAP)*, Nov 2012.

[30] J. Wang and M. G. Amin, "Gps interference cancellation performance in single and multiple mvdr beamforming methods," in *Fortieth Asilomar Conference on Signals, Systems and Computers (ACSSC)*, Oct 2006.

[31] S. Backén, D. M. Akos, and M. L. Nordenvaad, "Post-processing dynamic gnss antenna array calibration and deterministic beamforming," in *Proceedings of the 21st International Technical Meeting of the Satellite Division of The Institute of Navigation (ION GNSS)*, 2008.

[32] A. K. Brown and B. Mathews, "Gps multipath mitigation using a three dimensional phased array," in *Proceedings of the 18th International Technical Meeting of the Satellite Division of The Institute of Navigation (ION GNSS)*, Sep 2005.

[33] J. Max, "Quantizing for minimum distortion," in *IRE Transactions on Information Theory*, vol. 6, no. 1, 1960.

[34] A. Schmid, A. Neubauer, H. Ehm, and R. Weigel, "Galileo/gps receiver fixed-point implementation using conventional and differential correlation," in *Proceedings of the 18th International Technical Meeting of the Satellite Division of The Institute of Navigation (ION GNSS)*, 2005.

[35] A. Mezghani, F. Antreich, and J. A. Nossek, "Multiple parameter estimation with quantized channel output," in *International ITG Workshop on Smart Antennas (WSA)*, 2010.

[36] A. T. Balaei, "Quantization degradation of gnss signal quality in the presence of cw rfi," in *IEEE 10th International Symposium on Spread Spectrum Techniques and Applications*, 2008.

[37] J. Curran, D. Borio, and C. C. Murphy, "Front-end filtering and quantisation effects on gnss signal processing," in *1st International Conference on Wireless Communication, Vehicular Technology, Information Theory and Aerospace and Electronic Systems Technology (Wireless VITAE)*, 2009.

[38] J. Curran, D. Borio, G. Lachapelle, and C. C. Murphy, "Reducing front-end bandwidth may improve digital gnss receiver performance," in *IEEE Transactions on Signal Processing*, vol. 58, no. 4, 2009.

[39] C.-C. Sun and S.-S. Jan, "Interference characteristics for the civil airport environment using time-frequency analysis," in *Position Location and Navigation Symposium (PLANS)*, 2012.

[40] R. L. Fante and J. J. Vaccaro, "Evaluation and reduction of multipath-induced bias on gps time-of-arrival," *IEEE Transactions on Aerospace and Electronic Systems*, vol. 39, no. 3, Jul 2003.

[41] D. M. Akos and M. Pini, "Effect of sampling frequency on gnss receiver performance," in *Journal of The Institute of Navigation*, vol. 53, no. 2, 2006.

[42] T. Noll, "Sensor array processing for multipath and radio interference identification and suppression - samurai : Abschlussbericht," Lehrstuhl für Allgemeine Elektrotechnik und Datenverarbeitungssysteme (EECS) der Rheinisch-

Westfälischen Technischen Hochschule Aachen, Tech. Rep., 2014. [Online]. Available: http://edok01.tib.uni-hannover.de/edoks/e01fb16/847440400.pdf

[43] *Cyclone V Device Datasheet CV-51002*, Altera Corporation, 6 2012. [Online]. Available: https://www.altera.com/en_US/pdfs/literature/hb/cyclone-v/cv_51002.pdf

[44] K. Gold and A. Brown, "An array of digital antenna elements for mitigation of multipath for carrier landings," in *Proceedings of the 2005 National Technical Meeting of The Institute of Navigation*, Jan 2005.

[45] A. Konovaltsev, F. Antreich, and A. Hornbostel, "Performance assessment of antenna array algorithms for multipath and interferers mitigation," in *2nd Workshop on GNSS Signals and Signal Processing (GNSS SIGNALS)*, Apr 2007.

[46] M. Sahmoudi and M. G. Amin, "Optimal robust beamforming for interference and multipath mitigation in gnss arrays," in *IEEE International Conference on Acoustics, Speech and Signal Processing (ICASSP)*, Apr 2007.

[47] A. Paulraj, R. Roy, and T. Kailath, "Estimation of signal parameters via rotational invariance techniques- esprit," in *Nineteeth Asilomar Conference on Circuits, Systems and Computers*, Nov 1985.

[48] R. Schmidt, "Multiple emitter location and signal parameter estimation," *IEEE Transactions on Antennas and Propagation*, vol. 34, no. 3, Mar 1986.

[49] S. Daneshmand, "Gnss interference mitigation using antenna array processing," Ph.D. dissertation, University of Calgary, 2013.

[50] S. Daneshmand, A. Broumandan, and G. Lachapelle, "Gnss interference and multipath suppression using array antenna," in *Proceedings of the 24th International Technical Meeting of The Satellite Division of the Institute of Navigation (ION GNSS)*, 2011.

[51] J. L. Vicario, M. Barcelo, M. M. nosas, G. Seco-Granados, F. Antreich, J. M. Cebrian, J. Picanyol, and F. Amarillo, "A novel look into digital beamforming techniques for multipath and interference mitigation in galileo ground stations," in *5th Advanced Satellite Multimedia Systems Conference and the 11th Signal Processing for Space Communications Workshop*, Sep 2010.

[52] L. Du, T. Yardibi, J. Li, and P. Stoica, "Review of user parameter-free robust adaptive beamforming algorithms," in *42nd Asilomar Conference on Signals, Systems and Computers*, Oct 2008.

[53] G. Seco-Granados, J. Fernandez-Rubio, and C. Fernandez-Prades, "Ml estimator and hybrid beamformer for multipath and interference mitigation in gnss receivers," *IEEE Transactions on Signal Processing*, vol. 53, no. 3, Mar 2005.

[54] M. D. Zoltowski and A. S. Gecan, "Advanced adaptive null steering concepts for gps," in *Military Communications Conference (MILCOM '95), Conference Record, IEEE*, 1995.

[55] H. Krim and M. Viberg, "Two decades of array signal processing research," in *IEEE Signal Processing Magazine*, vol. 13, 1996.

[56] B. H. Fleury, M. Tschudin, R. Heddergott, D. Dahlhaus, and K. I. Pedersen, "Channel parameter estimation in mobile radio environments using the sage algorithm," in *IEEE Journal on Selected Areas in Communications*, vol. 17, no. 3, Mar 1999.

[57] S. Rougerie, A. Konovaltsev, M. Cuntz, G. Carrie, L. Ries, F. Vincent, and R. Pascaud, "Comparison of sage and classical multi-antenna algorithms for multipath mitigation in real-world environment," in *5th ESA Workshop on Satellite Navigation Technologies and European Workshop on GNSS Signals and Signal Processing (NAVITEC)*, Dec 2010.

[58] D. S. De Lorenzo, "Navigation accuracy and interference rejection on gps adaptive antenna arrays," Ph.D. dissertation, Stanford University, 2007.

[59] M. S. Bartlett, "Smoothing periodograms from time-series with continuous spectra," *Nature*, vol. 161, no. 4096, May 1948.

[60] J. Capon, "High-resolution frequency-wavenumber spectrum analysis," in *Proceedings of the IEEE*, vol. 57, no. 8, 1969.

[61] H. L. V. Trees, *Optimum Array Processing: Part IV of Detection, Estimation, and Modulation Theory*. John Wiley and Sons, Inc., 2002.

[62] D. S. De Lorenzo, J. Gautier, J. Rife, P. Enge, and D. Akos, "Adaptive array processing for gps interference rejection," in *Proceedings of the 18th International Technical Meeting of the Satellite Division of The Institute of Navigation (ION GNSS)*, 2005.

[63] J. Arribas, C. Fernandez-Prades, and P. Closas, "Multi-antenna techniques for interference mitigation in gnss signal acquisition," *EURASIP Journal on Advances in Signal Processing*, 2013.

[64] D. S. De Lorenzo, F. Antreich, H. Denks, A. Hornbostel, C. Weber, and P. Enge, "Testing of adaptive beamsteering for interference rejection in gnss receivers," in *European Navigation Conference (ENC)*, 2007.

[65] R. L. Fante and J. J. Vaccaro, "Wideband cancellation of interference in a gps receive array," in *IEEE Transactions on Aerospace and Electronic Systems*, vol. 36, no. 2, 2000.

[66] L.-J. Wang, H.-C. Zhao, G. Xiong, and J.-B. Liu, "Adaptive beamforming with coherent interference for gps receivers," in *Proceedings of the 4th International Conference on Microwave and Millimeter Wave Technology (ICMMT)*, Aug 2004.

[67] H. Zhao, B. Lian, and J. Feng, "Interference suppression in gnss receiver using space-time adaptive processing," in *International Conference on Medical Physics and Biomedical Engineering*, 2012.

[68] ——, "Interference suppression in gnss receiver using space-time adaptive processing," in *IEEE 3rd International Conference on Communication Software and Networks (ICCSN)*, 2011.

[69] G. Kappen, C. Haettich, and M. Meurer, "A robust multi-antenna mass-market gnss receiver," *GPS World*, vol. 23, no. 9, 2012.

[70] L. Kurz, E. Tasdemir, D. Bornkessel, T. G. Noll, G. Kappen, F. Antreich, M. Sgammini, and M. Meurer, "An architecture for an embedded antenna-array digital gnss receiver using subspace-based methods for spatial filtering," in *6th ESA Workshop on Satellite Navigation Technologies and European Workshop on GNSS Signals and Signal Processing (NAVITEC)*, 2012.

[71] E. Tasdemir, L. Kurz, and T. Noll, "Optimization of a blind adaptive spatial filter for interference mitigation in gnss receivers," in *Proceedings of the 26th International Technical Meeting of The Satellite Division of the Institute of Navigation (ION GNSS+)*, 2013.

[72] A. Gecan and M. Zoltowski, "Power minimization techniques for gps null steering antenna," in *Proceedings of the 8th International Technical Meeting of the Satellite Division of The Institute of Navigation*, Sep 1995.

[73] S. O. Haykin, *Adaptive Filter Theory*, 3rd ed. Prentice Hall, 1995.

[74] W. H. Press, S. A. Teukolsky, W. T. Vetterling, and B. P. Flannery, *Numerical Recipes in C: The Art of Scientific Computing*, 3rd ed. Cambridge University Press, 1997.

[75] A. Kessy, A. Lewin, and K. Strimmer, "Optimal whitening and decorrelation," *arXiv*, 2015. [Online]. Available: https://arxiv.org/abs/1512.00809v1

[76] A. J. Bell and T. J. Sejnowski, "The "independent components" of natural scenes are edge filters," *Vision Res.*, vol. 37, no. 23, 1997.

[77] M. I. adn B. Eissfeller, "Comparison of multipath mitigation techniques with consideration of future signal structures," in *Proceedings of the 16th International Technical Meeting of the Satellite Division of The Institute of Navigation (ION GPS/GNSS)*, Sep 2003.

[78] J. V. Dierendonck, P. Fenton, and T. Ford, "Theory and performance of narrow correlator spacing in a gps receiver," *Journal of the Institute of Navigation*, vol. 39, no. 3, 1992.

[79] G. A. M. adn Michael S. Braasch, "Gnss multipath mitigation using gated and high resolution correlator concepts," in *Proceedings of the 1999 National Technical Meeting of The Institute of Navigation*, Jan 1999.

[80] S. Rougerie, G. Carrié, F. Vincent, L. Ries, and M. Monnerat, "A new multipath mitigation method for gnss receivers based on an antenna array," *International Journal of Navigation and Observation*, vol. 2012, 2012.

[81] W. Myrick, M. Zoltowski, and J. Goldstein, "Anti-jam space-time preprocessor for gps based on multistage nested wiener filter," in *IEEE Military Communications Conference Proceedings (MILCOM)*, 1999.

[82] P. B. Anantharamu, D. Borio, and G. Lachapelle, "Space-time equalization techniques for new gnss signals," in *Proceedings of the 24th International Technical Meeting of The Satellite Division of the Institute of Navigation (ION GNSS)*, 2011.

[83] S. Rounds, "Jamming protection of gps receivers," *GPS World*, vol. 15, no. 2, Feb 2004.

[84] C. H. Kang, S. Y. Kim, and C. G. Park, "A gnss interference identification using an adaptive cascading iir notch filter," *GPS Solutions*, vol. 18, no. 4, Oct 2014.

[85] D. S. De Lorenzo, J. Rife, P. Enge, and D. Akos, "Navigation accuracy and interference rejection for an adaptive gps antenna array," in *Proceedings of the 19th International Technical Meeting of the Satellite Division of The Institute of Navigation (ION GNSS)*, 2006.

[86] D. Borio, L. Camoriano, and L. L. Presti, "Two-pole and multi-pole notch filters: a computationally effective solution for interference detection and mitigation," in *7th International Conference on ITS Telecommunications*, Jun 2007.

[87] A. J. O'Brien and I. J. Gupta, "Optimum adaptive filtering for gnss antenna arrays," in *Proceedings of the 21st International Technical Meeting of the Satellite Division of The Institute of Navigation (ION GNSS)*, Sep 2008.

[88] W. Myrick, M. Zoltowski, and J. Goldstein, "Gps jammer suppression with low-sample support using reduced-rank power minimization," in *Proceedings of the Tenth IEEE Workshop on Statistical Signal and Array Processing*, Aug 2000.

[89] A. Paulraj and E. Lindskog, "Taxonomy of space-time processing for wireless networks," *IEE Proceedings - Radar, Sonar and Navigation*, vol. 145, no. 1, Feb 1998.

[90] E. Tasdemir, L. Kurz, and T. Noll, "Combined spatial-temporal filtering for interference mitigation in gnss receivers," in *European Navigation Conference (ENC)*, 2014.

[91] ——, "A spatial-temporal filter for interference mitigation in gnss receivers," in *Proceedings of the 27th International Technical Meeting of The Satellite Division of the Institute of Navigation (ION GNSS+)*, 2014.

[92] L. B. Milstein, "Interference rejection techniques in spread spectrum communications," *Proceedings of the IEEE*, vol. 76, no. 6, Jun 1988.

[93] J. W. Choi and N. I. Cho, "Suppression of narrow-band interference in ds-spread spectrum systems using adaptive iir notch filter," *Signal Processing*, vol. 82, no. 12, Dec 2002.

[94] D. Borio, C. O'Driscoll, and J. Fortuny, "Gnss jammers: Effects and countermeasures," in *6th ESA Workshop on Satellite Navigation Technologies and European Workshop on GNSS Signals and Signal Processing (NAVITEC)*, Dec 2012.

[95] D. Borio, "A multi-state notch filter for gnss jamming mitigation," in *International Conference on Localization and GNSS (ICL-GNSS)*, Jun 2014.

[96] D. Borio, L. Camoriano, S. Savasta, and L. L. Presti, "Time-frequency excision for gnss applications," *IEEE Systems Journal*, vol. 2, no. 1, Feb 2008.

[97] A. D. Fonzo, M. Leonardi, G. Galati, P. Madonna, and L. Sfarzo, "Software-defined-radio techniques against jammers for in car gnss navigation," in *Metrology for Aerospace (MetroAeroSpace), IEEE*, May 2014.

[98] S. Savasta, L. L. Presti, and M. Rao, "Interference mitigation in gnss receivers by a time-frequency approach," *IEEE Transactions on Aerospace and Electronic Systems*, vol. 49, no. 1, Jan 2013.

[99] Y.-R. Chien and P.-Y. Chen, "Wavelet-packet-transform-based adaptive predictor to mitigate gnss jammers," in *International Conference on Wavelet Analysis and Pattern Recognition (ICWAPR)*, Jul 2015.

[100] M. Cuntz, A. Konovaltsev, A. Hornbostel, E. S. Neves, and A. Dreher, "Galant - galileo antenna and receiver demonstrator for safety-critical applications," in *European Conference on Wireless Technologies*, Oct 2007.

[101] R. D. J. V. Nee, "Spread-spectrum code and carrier synchronization errors caused by multipath and interference," *IEEE Transactions on Aerospace and Electronic Systems*, vol. 29, no. 4, Oct 2002.

[102] H. Hurskainen, E. S. Lohan, X. Hu, J. Raasakka, and J. Nurmi1, "Multiple gate delay tracking structures for gnss signals and their evaluation with simulink, systemc, and vhdl," *International Journal of Navigation and Observation*, vol. 2008, 2008.

[103] M. Lashley and D. M. Bevly, "Gnss solutions: What are vector tracking loops, and what are their benefits and drawbacks?" *Inside GNSS*, 2009.

[104] P. D. Groves, *Principles of GNSS, Inertial, and Multisensor Integrated Navigation Systems*. Artech House, 2008.

[105] "Galileo online: Go!" http://go-galileo-online.de/.

[106] E. Tasdemir, G. Kappen, and T. Noll, "Potential of using block floating point arithmetic in asip-based gnss-receivers," in *21st IEEE International Conference on Application-specific Systems Architectures and Processors (ASAP)*, 2010.

[107] E. Tasdemir, L. Kurz, and T. G. Noll, "Efficient computation of the position, velocity and time estimation algorithm on a gnss processor using interpolation," in *6th ESA Workshop on Satellite Navigation Technologies and European Workshop on GNSS Signals and Signal Processing, (NAVITEC)*, 2012.

List of Publications

i. Tasdemir, E.; Kurz, L.; Noll, T. G.; *"Combined Spatial-Temporal Filtering for Interference Mitigation in GNSS Receivers"*, Proceedings of the European Navigation Conference (ENC) 2014, Rotterdam, The Netherlands, 14.04-17.04.2014, 2014

   also in

   - Coordinates vol. 10, no. 12, 2014
   - European Journal of Navigation vol. 12, no. 2, p. 4-10, 2014

ii. Tasdemir, E.; Kurz, L.; Noll, T. G.; *"A Spatial-Temporal Filter for Interference Mitigation in GNSS Receivers"*, Proceedings of the 27th International Technical Meeting of the Satellite Division of the Institute of Navigation: (ION GNSS+), Tampa, Florida, USA, 08.-12.09.2014 p. 3502-3509, 2014

   Award: Best Student Paper Award

iii. Tasdemir, E.; Kurz, L.; Noll, T. G.; *"Optimization of a Blind Adaptive Spatial Filter for Interference Mitigation in GNSS Receivers"*, Proceedings of the 26th International Technical Meeting of the Satellite Division of The Institute of Navigation, ION GNSS+ 2013, Sept. 16 - 20, 2013, Nashville Convention Center, Nashville, Tennessee, p. 3424-3432, 2013

iv. Tasdemir, E.; Kurz, L.; Noll, T. G.; *"Efficient Computation of the Position, Velocity and Time Estimation Algorithm on a GNSS Processor Using Interpolation"*, Proceedings of the 6th ESA Workshop on Satellite Navigation Technologies (Navitec 2012) & European Workshop on GNSS Signals and Signal Processing, Noordwijk, 5 - 7 December 2012, 2012

v. Tasdemir, E.; Kappen, G. C.; Noll, T. G.; *"Block Floating Point Arithmetic for Low-Energy GNSS-Receiver PVT-Estimation"*, Proceedings of the 23rd International Technical Meeting of the Satellite Division of the Institute of Navigation (ION GNSS) 2010, Portland, Oregon, USA, 21.09.-24.09.2010, p. 2933-2940, 2010

vi. Tasdemir, E.; Kappen, G. C.; Noll, T. G.; *"Potential of using Block Floating Point Arithmetic in ASIP-Based GNSS-Receivers"*, Proceedings of the 21st IEEE International Conference on Application Specific Systems, Architectures and Processors (ASAP) 2010, July 7-9, 2010, Rennes, France, p. 293-296, 2010

vii. Kurz, L.; Tasdemir, E.; Noll, T. G.; *"JamCam: a Camera-Integrated GNSS Receiver for Spatial Detection of Radio Frequency Interference Sources"*, Proceedings of the 7th ESA Workshop on Satellite Technologies, NAVITEC, Nordwijk, Netherlands, 3 Dec 2014 - 5 Dec 2014, 2014

viii. Castaneda, M. H.; Stein, M.; Antreich, F.; Tasdemir, E.; Kurz, L.; Noll, T. G.; Nossek, J. A.; *"Joint Space-Time Interference Mitigation for Embedded Multi-Antenna GNSS Receivers"*, Proceedings of the 26th International Technical Meeting of the Satellite Division of the Institute of Navigation, ION GNSS+ 2013, Sept. 16 - 20, 2013, Nashville Convention Center, Nashville, Tennessee, p. 3399-3408, 2013

ix. Kurz, L.; Tasdemir, E.; Bornkessel, D.; Noll, T. G.; Kappen, G. C.; Antreich, F.; Sgammini, M.; Meurer, M.; *"An Architecture for an Embedded Antenna-Array Digital GNSS Receiver Using Subspace-Based Methods for Spatial Filtering"*, Proceedings of the 6th ESA Workshop on Satellite Navigation Technologies (Navitec 2012) & European Workshop on GNSS Signals and Signal Processing, Noordwijk, 5 - 7 December 2012, 2012

Lebenslauf

Persönliche Daten

Name	Tasdemir
Vorname	Emrah
Geburtsdatum	16. Oktober 1984
Geburtsort	Istanbul, Türkei
Eltern	Fatma Taşdemir (geb. Timurlenk, Chemikerin) Murtaza Taşdemir (inhabender Geschäftsführer)
Geschwister	Ezgi Taşdemir Ergün (geb. Taşdemir, Wirtschaftsingenieurin)

Beruflicher Werdegang

seit 04.2017	Entwicklungsingenieur bei Rohde & Schwarz GmbH & Co KG
12.2009 - 08.2016	Wissenschaftlicher Mitarbeiter am Lehrstuhl für Allgemeine Elektrotechnik und Datenverarbeitungssysteme (EECS) der Rheinisch-Westfälischen Technischen Hochschule (RWTH) Aachen
04.2008 - 10.2008	Fachpraktikum bei Philips Research Aachen
04.2007 - 10.2009	Studentische Hilfskraft am EECS

Studium

seit 12.2009	Promotion Elektrotechnik und Informationstechnik (ET/IT) an der RWTH Aachen
10.2003 - 10.2009	Studium der ET/IT an der RWTH Aachen (Vertiefung in Informations- und Kommunikationstechnik) Diplomarbeit am EECS: *"Untersuchung optimierter Fließkomma-Datenformate für Positionsberechnungsalgorithmen"*

Schulausbildung

09.1995 - 06.2003	Istanbul Lisesi (Istanbul, Gymnasium)
09.1990 - 06.1995	Dr. Refik Saydam Ilköğretim Okulu (Istanbul, Grundschule)